University of Colorado, Boulder
CU Scholar

Aerospace Engineering Sciences Graduate Theses & Dissertations

Aerospace Engineering Sciences

Spring 1-1-2013

The Effects of Composition on Thermosphere Mass Density Response to Geomagnetic Activity

Xianjing Liu
University of Colorado Boulder, xjliu.pku@gmail.com

Follow this and additional works at: https://scholar.colorado.edu/asen_gradetds

Part of the Aerospace Engineering Commons, and the Atmospheric Sciences Commons

Recommended Citation
Liu, Xianjing, "The Effects of Composition on Thermosphere Mass Density Response to Geomagnetic Activity" (2013). *Aerospace Engineering Sciences Graduate Theses & Dissertations*. 74.
https://scholar.colorado.edu/asen_gradetds/74

This Dissertation is brought to you for free and open access by Aerospace Engineering Sciences at CU Scholar. It has been accepted for inclusion in Aerospace Engineering Sciences Graduate Theses & Dissertations by an authorized administrator of CU Scholar. For more information, please contact cuscholaradmin@colorado.edu.

www.manaraa.com

The Effects of Composition on Thermosphere Mass Density Response to Geomagnetic Activity

Xianjing Liu

M.S., Aerospace Engineering Sciences, University of Colorado at Boulder, 2009

A thesis submitted to the
Faculty of the Graduate School of the
University of Colorado in partial fulfillment
of the requirements for the degree of
Doctor of Philosophy
Department of Aerospace Engineering Sciences
2013

www.manaraa.com

This thesis entitled:

To Investigate Composition Affects on Thermosphere Mass Density

written by Xianjing Liu

has been approved for the Department of Aerospace Engineering Sciences

_____

Prof. Jeffrey P. Thayer (Chair)

_____

Prof. Delores J. Knipp

Date _____

The final copy of this thesis has been examined by the signatories, and we find that both the content and the form meet acceptable presentation standards of scholarly work in the above mentioned discipline.

www.manaraa.com

Xianjing, Liu (Ph.D., Aerospace Engineering Sciences)

The Effects of Composition on Thermosphere Mass Density Response to Geomagnetic Activity

Thesis advised by Professor Jeffrey P. Thayer

The ability to determine the thermosphere mass density response to geomagnetic disturbances is of critical importance in understanding how energy deposited in the thermosphere affects satellite drag. The response is dependent on the state of the thermosphere prior to geomagnetic activity. The recent extreme solar minimum of 2008 results in the preconditioned thermosphere to be a cold and contracted multiconstituent gas. The associated reduced constituent scale heights led to more concentrated transitions of heavy species to light species with altitude. This dissertation focuses on investigating the effects of composition on the thermosphere mass density change during geomagnetic activity, with particular emphasis on conditions of the recent extreme solar minimum.

A study of the mass density response to geomagnetic activity demonstrated complex behavior in the region near the oxygen to helium transition near 450 km. This study was expanded to explore the altitude variation of mass density response throughout the thermosphere and identified the helium / oxygen transition to have the greatest impact. Further analysis related the mass density peturbation with changes in the density scale height. It was found that the

www.manaraa.com

molecular weight scale height perturbation near the helium / oxygen transition region contributed significantly to the mass density response.

The significant role of helium on mass density response warranted the extraction of helium number densities from the CHAMP and GRACE satellite measurements. A comparison between the derived helium concentration from satellite and the NRL-MSISE00 estimate indicated more helium was present in the winter polar regions than represented by MSIS.

Physical models of the thermosphere in general do not include helium. A helium module was implemented into the Thermosphere Ionosphere Electrodynamics General Circulation Model (TIEGCM). A comparison between TIEGCM modeling with helium and without helium illustrated the need to include helium in order to reproduce the observations. The mechanism for the winter helium bulge formation was also revisited in this work. It was found that vertical advection of helium dominates its formation while hemispheric horizontal transport, once considered the primary process, is of secondary importance.

www.manaraa.com

Dedication

To my parents, Wangrong Liu and Yunfeng Yu, my husband Bo Tan, who gave me continuous encouragement and support.

www.manaraa.com

Acknowledgements

I would like to thank my advisor, Prof. Jeffrey P. Thayer. I have worked with Prof. Jeffrey Thayer for five years since the fall of 2008. I greatly appreciate the tremendous time Prof. Jeffrey Thayer spent discussing with me and providing guidance to me about my PhD research. I have worked with Dr. Alan Burns and Dr. Wenbin Wang for two years since May 2011. I'm really grateful for their ideas and guidance on my PhD research and the time they spent discussing with me.

I would like to thank my committee members Prof. Jeffrey Forbes, Dr. Arthur Richmond, Prof. Delores J. Knipp, and Prof. Fran Bagenal for their time spent on my comprehensive exam and thesis defense.

I would like to thank my colleagues and friends in Thayer's Research Group for your support during my graduate study.

Finally I would like to acknowledge the Air Force Office of Scientific Research and NASA for providing financial support during my PhD study. I would like to acknowledge the National Center for Atmospheric Research (NCAR)/High Altitude Observatory (HAO) for providing the computing resources used in my research.

www.manaraa.com

Contents

Chapter 1 Introduction 1

1.1 Research Motivation and Impact 1

1.2 Thesis Overview 3

1.3 Thermosphere Preconditioned State 4

1.3.1 Thermospheric preconditioned state related to Solar Cycle variations 4

1.3.2 Thermosphere Temperature and Composition Structure 6

1.3.3 Governing Equation for Thermosphere Composition 8

1.3.4 Thermosphere Dynamics 16

1.3.5 Escape of the Atmosphere 17

1.3.6 Thermosphere Measurements 18

1.4 Thermosphere Disturbed State 19

1.4.1 Categories of the geomagnetic storms 20

1.4.2 Geomagnetic indices 21

1.4.3 Dependence of geomagnetic disturbance on precondition state 22

1.4.4 Thermosphere composition response to geomagnetic forcing 25

1.4.5 Thermosphere mass density change at fixed altitude and fixed pressure level 27

1.5 Data and Models 30

1.5.1 CHAMP 30

1.5.2 GRACE 31

www.manaraa.com

1.5.3 NRL-MSISE00 32

1.5.4 NCAR TIEGCM Model 32

Chapter 2 Observations of Thermosphere Mass Density Response and Inferred Composition Effect 34

2.1 Solar Minimum of Cycle 23/24 34

2.2 CHAMP to GRACE Mass Density Ratio 38

2.3 Satellite observed C/G mass density ratio in 2007 and 2008 40

2.4 MSISE00 Simulations of C/G ratio and Scale Heights in 2007 and 2008 46

2.5 Oxygen / Helium Transition Altitudes 59

2.6 Conclusions 62

Chapter 3 Altitude Variations of the Thermosphere Mass Density Response 67

3.1 Background Introduction 67

3.2 Mass Density Observation from CHAMP and GRACE 70

3.3 Helium Estimation from CHAMP and GRACE Measurement 72

3.4 Mass Density and Scale Height Perturbations 81

3.4.1 Storm time mass density perturbation in MSIS 81

3.4.2 Parameters that affect the mass density perturbations 83

3.4.3 Parameters that affect mass density scale height perturbations 86

3.5 Conclusion 96

Chapter 4 TIEGCM with Helium module 99

4.1 Introduction 99

www.manaraa.com

4.2 Numerical experiments 100

4.3 Analysis and Results 102

4.3.1 Change in Thermosphere parameters of TIEGCM at fixed altitudes 102

4.3.2 Changes in altitude profiles of thermosphere parameters in TIEGCM 107

4.3.3 Changes in thermosphere parameters of TIEGCM at fixed pressure level 109

4.4 Test of helium in TIEGCM 114

4.5 Discussion and Conclusions 118

Chapter 5 A Revisit of the Winter Helium Bulge Formation 120

5.1 Introduction 121

5.2 TIEGCM Helium Minor vs. Helium Major 123

5.3 TIEGCM Helium Minor Numerical experiments 125

5.4 Mechanism For Winter Helium Bulge 127

5.5 Discussion and Conclusions 132

Chapter 6 Conclusions and Outlooks 140

6.1 Conclusions 140

6.2 Recommendation for Future Study 144

References 146

Appendix A Drag Coefficient Calculations 156

Appendix B Helium concentration estimation at the GRACE altitude 160

www.manaraa.com

List of Figures

Figure 1.1. Energy transfer from the Sun to the Earth upper atmosphere [*Prölss,* 2011] 5

Figure 1.2. Time series of (a) Global mean thermosphere mass density at 400 km, over four solar cycles, (b) F10.7 solar proxy index. Blue dots, daily mean values; red lines, 81 day centered running means; solid black lines, annual means [*Solomon et al.,* 2011]. 6

Figure 1.3. Altitude profile of the daily zonal mean temperature [K] at the latitude 57 degree north (black) and 57 degree south (red) in Dec 1, 2008. 7

Figure 1.4. Altitude profile of the daily zonal mean number density [m^{-3}] of the thermospheric individual constituents at 30 degree north on Dec 1, 2008. 8

Figure 1.5. The absolute and relative change in mass density at 400 km for the same energy deposition by a geomagnetic storm during solar minimum vs. solar maximum. 23

Figure 1.6. The response of the molecular nitrogen density to geomagnetic activities in difference seasons and solar activities. The N_2 data is measured by ESRO-4 satellite and normalized to 270 km. [*Prölss,* 2011] 24

Figure 1.7. The latitudinal variation of the composition and density perturbation during the geomagnetic storm in October 29, 1973 at 09 solar local time. The top panel shows the relative changes in argon (Ar), molecular nitrogen (N_2), atomic oxygen (O) and helium (He) densities referred to the prestorm conditions and normalized to 280 km [*Prölss,* 2011]. 26

Figure 2.1. a) Latitude-time plot of the natural logarithm of the GRACE and CHAMP mass density ratio normalized by the satellite altitude difference for a 29 day period at 10 SLT

www.manaraa.com

starting from February 1, 2007, b) K_p and $F_{10.7}$ indices and c) time series of the data in (a) at the specific latitudes of 58°S and 59°N. 42

Figure 2.2. a) Latitude-time plot of the natural logarithm of the GRACE and CHAMP mass density ratio normalized by the satellite altitude difference for a 30 day period at 9 SLT starting from December 1, 2008, b) K_p and $F_{10.7}$ indices and c) time series of the data in (a) at the specific latitudes of 58°S and 59°N. 44

Figure 2.3. Latitude-time plot of the natural logarithm of the MSIS mass density ratio normalized by the altitude difference for CHAMP and GRACE satellites over a 29 day period at 10 SLT starting from February 1, 2007. 47

Figure 2.4. a) Time series of the MSIS February 2007 estimates from Figure 2.3, b) Time series of the MSIS reciprocal pressure scale height, and c) Time series of the MSIS reciprocal molecular weight scale height at the specific latitudes of 58°S and 59°N. 48

Figure 2.5. Latitude-time plot of the natural logarithm of the MSIS mass density ratio normalized by the altitude difference for CHAMP and GRACE satellites over a 30 day period at 9 SLT starting from December 1, 2008. 51

Figure 2.6. a) Time series of the MSIS December 2008 estimates from Figure 2.5, b) Time series of the MSIS reciprocal pressure scale height, and c) Time series of the MSIS reciprocal molecular weight scale height at the specific latitudes of 58°S and 59°N. 52

Figure 2.7. CHAMP and GRACE mass density estimates (red line) versus geographic latitude averaged over December 9-10, 2008. Adjusted MSIS mass density estimates after reducing $F_{10.7}$ index by 14 sfu and increasing ap by 2 (black line), further adjustment by increasing

www.manaraa.com

helium by 30% above 50° N (black dashed line), and excluding helium in the estimate of MSIS mass density after $F_{10.7}$ and ap adjustment (black dash-dot line). Error bars on GRACE density represent the statistical error of the mean after two-day averaging. 55

Figure 2.8. a) Time series of the adjusted MSIS December 2008 estimates from Figure 6, b) Time series of the adjusted MSIS reciprocal pressure scale height, and c) Time series of the adjusted MSIS reciprocal molecular weight scale height at the specific latitudes of 58°S and 59°N. 57

Figure 2.9. The adjusted MSIS oxygen-helium transition altitude for the month of December, 2008. 60

Figure 3.1. Latitudinal and UT variation of the thermosphere mass density near 09 LT from (a) CHAMP measurements normalized to 350 km and (b) GRACE measurements normalized to 500 km; (c) UT variations of the K_p index and $F_{10.7}$ index. 71

Figure 3.2. Latitudinal and UT variation of (a) helium and (b) oxygen number density at GRACE altitude estimated from CHAMP and GRACE satellite measurements; (c) The helium and (d) oxygen number density from adjusted MSIS estimation at GRACE altitude at 9 SLT. 73

Figure 3.3 (a) Latitudinal and UT variation of the logarithm of the helium to oxygen number density ratio at GRACE altitude, (b) The latitudinal profile of the mass density perturbation in percent change (%) during the geomagnetic active period Dec 05-06, 2008 at CHAMP and GRACE altitudes. 78

www.manaraa.com

Figure 3.4. Altitudinal and latitudinal variations of the mass density perturbation in percent change (%) during the Dec 05-06, 2008 geomagnetic storm from the adjusted NRL-MSISE00 estimation. The black dash lines indicate the CHAMP and GRACE altitudes. 82

Figure 3.5. (a) Altitudinal variation of mean molecular weight averaged over the geomagnetic quiet and active period at 75 S, (b) Altitude variation of the temperature percent change, mean molecular weight percent change, pressure percent change and density percent change during the geomagnetic storm at 75 S; (c) and (d) are similar to (a) and (b) but at 75 N. All the results in Figure 5 are from NRL-MSISE00 estimation. The quiet period is Dec 09-10 and the active period is Dec 05-06, 2008. 85

Figure 3.6. Altitudinal and latitudinal variations of the mass density scale height perturbation in percent change (%) during the Dec 05-06, 2008 geomagnetic storm from the adjusted MSIS estimation. The black dash lines indicate the CHAMP and GRACE altitudes. The purple dash line, originally displayed in Figure 3.4, indicating the altitude where the maximum density perturbation occurs..... 87

Figure 3.7. Altitudinal and latitudinal variation of the (a) temperature percent change (b) mean molecular weight percent change (c) pressure scale height percent change during geomagnetic active period Dec 05-06, 2008 by the adjusted MSIS estimation. The reference quiet time period is Dec 09-10, 2008..... 90

Figure 3.8. Altitudinal variation of the (a) helium to oxygen number density ratio (b) oxygen to molecular nitrogen number density ratio (c) mean molecular weight (d) mean molecular

www.manaraa.com

weight scale height during geomagnetic quiet and active period; All the results in Figure 8 are from adjusted MSIS estimation. The quiet period is Dec 09-10 and the active period is Dec 05-06, 2008..... 92

Figure 3.9 Altitudinal and latitudinal variation of (a) the mean molecular weight scale height perturbations (b) storm-time weighting factor a index (c) weighted mean molecular weight scale height perturbation (d) weighted pressure scale height perturbation during geomagnetic active period Dec 05-06, 2008 by the adjusted MSIS estimation. The reference quiet time period is Dec 09-10, 2008..... 93

Figure 4.1. Top panels from left to right are the latitudinal and UT variations of the TIEGCM w/o helium results of thermosphere mass density (kg/m^3), neutral temperature (K), mass mixing ratio of atomic oxygen and thermosphere mean molecular weight at 200 km, fixed 09 SLT. The bottom panels are similar to the top but are the results of TIEGCM w/ helium module. 103

Figure 4.2. The latitudinal and UT variations of the percent difference of TIEGCM after implementing the helium module in thermosphere mass density (Den), temperature (Tn), atomic oxygen mass mixing ratio (o1) and mean molecular weight (mbar) at 200 km, fixed 09 SLT. 105

Figure 4.3. Similar to the Figure 4.1, but at 400km 106

Figure 4.4. Similar to the Figure 4.2, but at 400 km. 107

Figure 4.5. Altitude variations of dairy mean mass density (unit: kg/m^3), temperature (unit: K)

www.manaraa.com

and atomic oxygen mass mixing ratio from left to right panel. The tops are the absolute values from the modeling without helium in blue and modeling with helium in red. The bottoms are the relative values calculated by (without/with-1)*100. The simulation is for day 336th of 2008 at fixed 09 SLT. 108

Figure 4.6. Top panels from left to right are the latitudinal and UT variations of the TIEGCM w/o helium modeling results of thermosphere mass density (kg/m^3), neutral temperature (K), mass mixing ratio of atomic oxygen and thermosphere mean molecular weight at fixed pressure level 15, 09 local time. The bottom panels are similar to the top panels but are the results of TIEGCM w/ helium module. 110

Figure 4.7. Similar to Figure 4.6, but at fixed pressure level 26. 111

Figure 4.8. The latitudinal and UT variations of the percent difference [%] of TIEGCM after implementing the helium module in thermosphere mass density (top left), temperature (top right), atomic oxygen mass mixing ratio (bottom left) and mean molecular weight (bottom right) at fixed pressure level 15, fixed 09 SLT. 113

Figure 4.9. Similar to the Figure 4.8, but at fixed pressure level 26. 114

Figure 4.10. Latitudinal and UT variation of (a) helium and (b) oxygen number density at 450 km estimated from CHAMP and GRACE satellite measurements; (c) The helium and (d) oxygen number density from TIEGCM w/ helium at 450 km. (e) The helium and (f) oxygen number density from adjusted MSIS estimation at 450 km at fixed 09 SLT. The unit for the number density is [m^{-3}]. 116

Figure 4.11. (a) Altitudinal and latitudinal variations of the mass density perturbation in percent

www.manaraa.com

change (%) during the day 340-341 (Dec 05-06) of 2008 geomagnetic storm from TIEGCM w/ helium, (b) Same as (a), but the result from TIEGCM w/o helium. 117

Figure 5.1. The latitudinal and longitudinal variations of the helium number density [m^{-3}] by TIEGCM w/ helium as minor species (Top) and w/helium as major species (Bottom) in day 326 of year 2008. The left are the results at 150 km and the right are the results at 400 km. Fixed $F_{10.7}$=70 sfu, K_p=2, UT=4. The upper boundary flux for the helium module is zero flux. 124

Figure 5.2. Similar to Figure 5.1, but the plots of the vertical wind. 125

Figure 5.3. (a) Latitudinal variation of the relative helium number density to the latitudinal mean at 97 (blue), 150 (red), 200 (green), 300 (black) and 400 km (purple) by TIEGCM model in day 10. Fixed $F_{10.7}$=70 sfu, K_p=2, UT=4, Lon=100 degree. The upper boundary flux for the helium module is $2x10^8$ $cm^{-2}s^{-1}$. (b) Same as Figure 5.3a, but the upper boundary flux for the helium module is $-w(z)*n_{he}(z)$. where n_{he} is the helium number density and w is the vertical wind. (c) Same as Figure 5.3a, but from NRL-MSISE00 simulation with same solar condition. 128

Figure 5.4. Latitudinal variation of relative helium number density to the latitudinal mean from day 1 to day 10 by TIEGCM, Fixed $F_{10.7}$=70 sfu, K_p=2, UT=4, Lon=100 degree. The upper boundary flux for the helium module is $-w(z)*n_{he}(z)$. The solid line represents the result of Run 1, the simulation includes both horizontal advection and vertical wind effects; the azure dash line shows the result of Run 2, the simulation with the horizontal advection off;

www.manaraa.com

the black dot line shows the result of Run 3, the simulation with the vertical wind effect off. 129

Figure 5.5. From top to bottom are the latitudinal and longitudinal variations of the vertical wind by TIEGCM, helium number density by TIEGCM and helium number density by NRL-MSISE00 in day 10. The left are the results at 150 km and the right are the results at 400 km. Fixed $F_{10.7}$=70 sfu, K_p=2, *UT*=4. The upper boundary flux for the helium module is $-w(z)*n_{he}(z)$. 131

Figure 5.6. (a) The altitude profile of the zonal mean vertical wind at 57 degree N (winter hemisphere) and 57 degree S (summer hemisphere) in day 10; (b) The altitude profile of the zonal mean He number density from TIEGCM Run 1 in solid line and TIEGCM Run 3 in dash line at 57 degree N (winter hemisphere) and 57 degree S (summer hemisphere) in day 10. Fixed $F_{10.7}$=70 sfu, K_p=2, *UT*=4, *Lon*=100 degree. The upper boundary flux for the helium module is $-w(z)*n_{he}(z)$. 133

Figure 5.7. Altitude variation of the mass density scale heights: the black dotted line is the actual density scale height for species *i* ; the blue dotted line is the density scale height of species *i* assuming in diffusive equilibrium and the red dotted line is the total mass density height assuming in diffusive equilibrium. (a) is for He, (b) is for O and (c) is for N_2. (d) are the actual density scale heights for N_2 in green, O in purple and He in blue. The density is the zonal mean density from TIEGCM Run 1 at 57 degree S (summer hemisphere) in day 10. Fixed $F_{10.7}$=70 sfu, K_p=2, *UT*=4, *Lon*=100 degree. The upper boundary flux for the helium module is $-w(z)*n_{he}(z)$. 137

www.manaraa.com

Figure 5. 8. (a) Exactly the same as Figure 5.3b; (b) Similar to (a), but from TIEGCM with helium as major species model with same solar condition. 138

Figure A.1. GRACE panel model C_DxA as a function of He/O ratio at two values of atmospheric temperature and angle of attack. 158

Figure A.2. MSIS outputs for December 9th 2008, sampled along the GRACE orbit. 159

Figure B.1. An example of the $F_{10.7}$ adjustment to best fit the NRL-MSISE00 total mass density output (black) with the total mass density by CHAMP measurement (red) in 09 December 2008; The adjustments of $F_{10.7}$ were from -15 to -9 with a step of 1, (b) Latitudinal variation of the MSIS adjusted exosphere temperature for 01-09 December 2008. 161

Figure B.2. (a) Latitudinal variation of the NRL-MSISE00 estimated exosphere temperature in 09 December, 2008 with the $F_{10.7}$ adjustments from -15 to -9; the step of the $F_{10.7}$ adjustment is 1, (b) Latitudinal variation of the relative uncertainty in calculated oxygen density at GRACE altitude from 01-09 December 2008. The result includes the error propagation of the uncertainty of oxygen density at CHAMP altitude and the uncertainty of the MSIS adjusted exosphere temperature at fixed 09 SLT. 165

www.manaraa.com

Chapter 1 Introduction

1.1 Research Motivation and Impact

Motivation: The thermosphere of the earth is a region of the atmosphere that ranges from 90 km up to about 1000 km and is populated by low-earth orbiting satellites and debris. The mass density of the thermosphere is one of the fundamental properties that describe the state of the thermosphere and is intimately connected to drag forces on low-earth orbiting objects. Uncertainties in thermosphere mass density variations is the major limiting factor for precise low-earth orbit determination/prediction at altitudes below about 700 km [*Marcos et al.,* 2010]. This uncertainty adversely impacts the accurate cataloging of all low-earth orbiting objects, their operational tracking, collision avoidance warning, and re-entry predictions. Furthermore, the error in thermosphere mass density estimation affects satellite design in estimating lifetime, on-board fuel, and attitude control. These aspects are motivating factors for developing improved estimates of mass density in the thermosphere. Geomagnetic storms produce the largest perturbations in thermosphere mass density and have a variability of their own due to complex pathways for energy deposition into the thermosphere.

Research Impact: This thesis focuses on the effects of neutral composition on thermosphere mass density response to geomagnetic activity. Here, it is established that the initial state of the thermosphere composition and the dynamic behavior of thermosphere consituents during geomagnetic activity impacts how the mass density will change during geomagnetic activity.

www.manaraa.com

Through analysis of high-resolution accelerometer measurements by the low-earth orbiting CHAMP (CHAllenging Minisatellite Payload) and GRACE (Gravity Recovery and Climate Experiment) satellites, application of the NRL-MSISE00 (Naval Research Laboratory's Mass Spectrometer and Incoherent Extended 2000) model, and numerical simulation, modification, and evaluation of the NCAR TIEGCM (Thermosphere – Ionosphere – Electrodynamics Global Circulation) Model, the following findings of this research are summarized.

- Illustrated that the preconditioned state of a cold and contracted thermosphere during this solar minimum resulted in a predominance of helium in the winter hemisphere.
- Demonstrated that the dynamic action of the oxygen to helium transition region in both latitude and altitude leads to complex behaviors in the mass density response throughout the extended solar minimum from 2007 to 2010.
- Compared the mass density response to a geomagnetic storm at two different altitudes using CHAMP and GRACE measurement and displayed the abnormal behavior in mass density response during solar minimum.
- Revealed the altitude distribution of storm-time density perturbation, with maximum perturbation to occur near the He/O transition region and a much weaker maximum near the O/N_2 transition region.
- Demonstrated the relation between density scale height, pressure scale height, mean molecular weight scale height and temperature scale height.

www.manaraa.com

- Disclosed the significant contribution of the molecular weight scale height to the mass density scale height and its influence on the altitude structure of density scale height perturbation.
- Extracted helium number densities near 500 km from the satellite measurements and clearly show the presence of a winter hemisphere helium bulge.
- Implemented a helium module into the Thermosphere Ionosphere Electrodynamics General Circulation Model (TIEGCM) by National Center for Atmospheric Research (NCAR) as a minor speices.
- Provided a comparison of modeling results between TIEGCM without helium and TIEGCM with helium.
- Reproduced the altitude variation of mass density in TIEGCM with helium model.
- Revisited the mechanism for the winter helium bulge formation using TIEGCM with helium as a minor species.
- Demonstrated that the vertical wind is the main source for the winter helium bulge formation. Hemispheric horizontal transport, once considered the primary process, is of secondary importance.

1.2 Thesis Overview

This dissertation is divided into six chapters. Following the introduction, Chapter 2 displays the composition preconditioned state impact from helium on the mass density response using CHAMP and GRACE coplanar orbits period in 2007 and 2008. Chapter 3 studies the altitude

www.manaraa.com

variation of thermosphere mass density response to geomagnetic forcing. Chapter 4 discusses the modeling of helium in TIEGCM and provides a comparison between the modeling of TIEGCM without helium module and the modeling of TIEGCM with helium module. Chapter 5 Compares the modeling result from the TIEGCM with helium as a major species to the TIEGCM with helium as a minor species, and uses the helium minor module to revisit the mechanisms for winter helium bulge formation. Chapter 6 summarizes the results of the dissertation and provides recommendations for future study.

1.3 Thermosphere Preconditioned State

The level of perturbation in the thermosphere mass density during geomagnetic activity is strongly dependent on the state of the thermosphere prior to the storm, which is referred to as the thermospheric preconditioned state in this study.

1.3.1 Thermospheric preconditioned state related to Solar Cycle variations

There are two ways that the energy from the sun is transferred to the thermosphere. One is by solar radiation in the extreme ultraviolet (EUV) that can be directly absorbed by the thermosphere and the other is by extracting energy from the solar wind stream that is dissipated in the upper atmosphere by Joule heating and particle precipitation. With regard to the first way, large changes in solar radiation are slow and relative to solar cycle variations, thus is more or less predictable [*Prölss,* 2011].

Hence the upper atmosphere state relative to solar radiation is treated as one of the thermospheric preconditions in this thesis. The thermosphere perturbations associated with the

www.manaraa.com

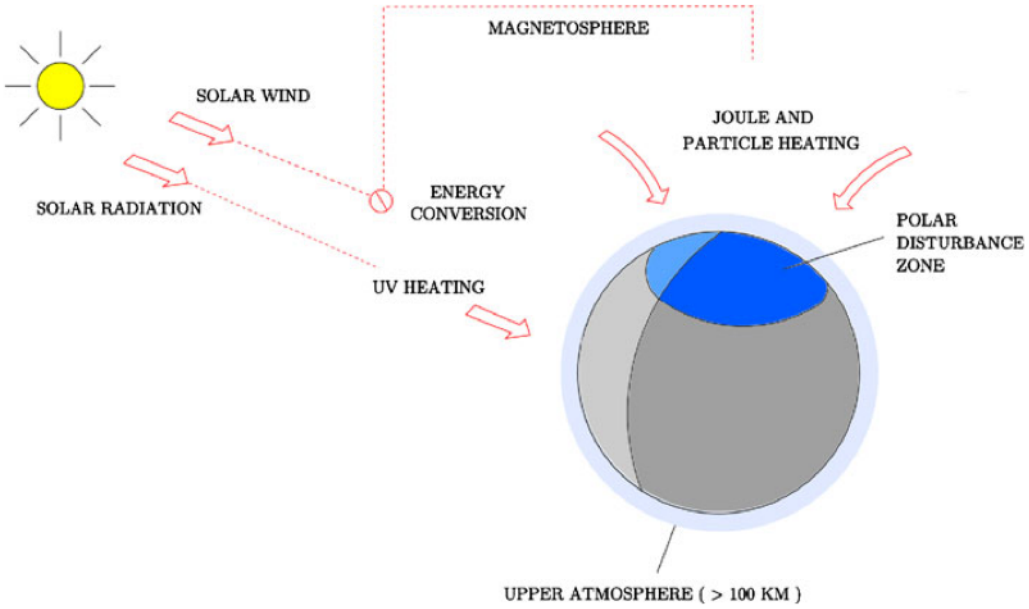

Figure 1.1. Energy transfer from the Sun to the Earth upper atmosphere [*Prölss,* 2011]

effect from the solar wind are usually referred to as 'geomagnetic storm effects', or 'geomagnetic disturbances', which are largely irregular and hard to predict. The change of the thermosphere properties during a geomagnetic storm will be discussed in the next section as the thermosphere disturbed state.

As the primary energy source to the upper atmosphere, the solar EUV irradiance variation is a critical precondition state that affects the amount of change in thermosphere density to geomagnetic activity. The $F_{10.7}$ index, a solar radio emission at 2800 MHz (10.7cm), is used to indicate the strength of UV and EUV radiation. The solar irradiance is correlated with the sunspot number, which follows a periodic variation of 11-year, that is, the 11-year solar cycle. Figure 1.2 shows the time variation of $F_{10.7}$ solar proxy index and the global mean thermosphere mass density obtained from the satellite orbital parameter at 400 km for four solar cycles

www.manaraa.com

[*Solomon et al.,* 2011]. Both the thermosphere mass density and the $F_{10.7}$ variations strongly follow the 11-year solar cycle, hence the $F_{10.7}$ index is adequate to illustrate the mass density level and the $F_{10.7}$ index is generally used as the input in models to represent the solar radiation conditions. Besides the 11-year variation, there are also annual or semi-annual variations in the thermosphere mass density due to seasonal changes. Variations in mass density related to the 27-day solar rotation are also illustrated in the blue line of Figure 1.2 as short-time variations compared to the 11-year variation. Note that the recent solar minimum in 2007-2010 is the lowest minimum since 1970, which results in an extremely low and contracted thermosphere. This solar minimum will be studied extensively in this thesis.

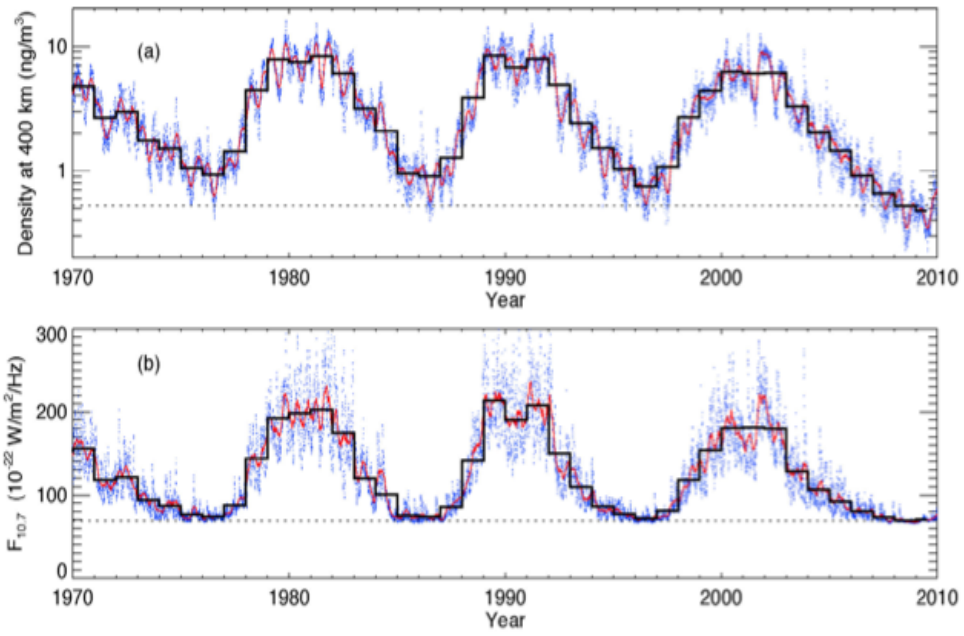

Figure 1.2. Time series of (a) Global mean thermosphere mass density at 400 km, over four solar cycles, (b) F10.7 solar proxy index. Blue dots, daily mean values; red lines, 81 day centered running means; solid black lines, annual means [*Solomon et al.,* 2011].

1.3.2 Thermosphere Temperature and Composition Structure

The solar EUV radiation is absorbed by the Earth's upper atmosphere and redistributed by

www.manaraa.com

emission, heat conduction, and winds. The altitude profile of the neutral temperature from TIEGCM modeling is illustrated in Figure 1.3. Note that in the thermosphere above 250 km, the temperature is almost uniform with altitude.

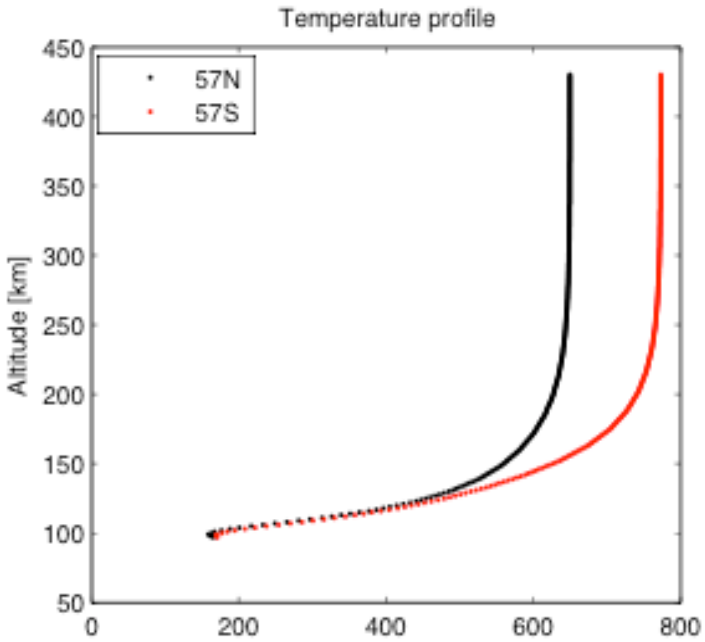

Figure 1.3. Altitude profile of the daily zonal mean temperature [K] at the latitude 57 degree north (black) and 57 degree south (red) in Dec 1, 2008.

With regard to the composition structure, Figure 1.4 demonstrates the altitude distribution of individual species from the NRL-MSISE00 model for solar minimum conditions in December 01, 2008. The thermosphere is a well-mixed multiconstituent gas, i.e. constant mixing ratio, below the altitude of the turbopause. The definition of the turbopause is where the molecular diffusion coefficient is equal to the eddy diffusion coefficient and, due to each species having a different diffusion coefficient; each species will have slightly different turbopause altitude. Above the turbopause, the altitude distribution of the individual species in the quiet-time thermosphere is basically described by diffusive equilibrium with species separating out with altitude by their

www.manaraa.com

respective molecular weights. Consequently, the neutral atmosphere from 150 km to 800 km progresses from 1) a molecular-nitrogen dominant region, 2) molecular nitrogen to oxygen transition region, 3) oxygen-dominant region, 4) oxygen to helium transition region and 5) a helium-dominant region as illustrated in Figure 1.4. The altitude where these transitions occur is temperature dependent through their individual scale heights and therefore varies with latitude, longitude and universal time.

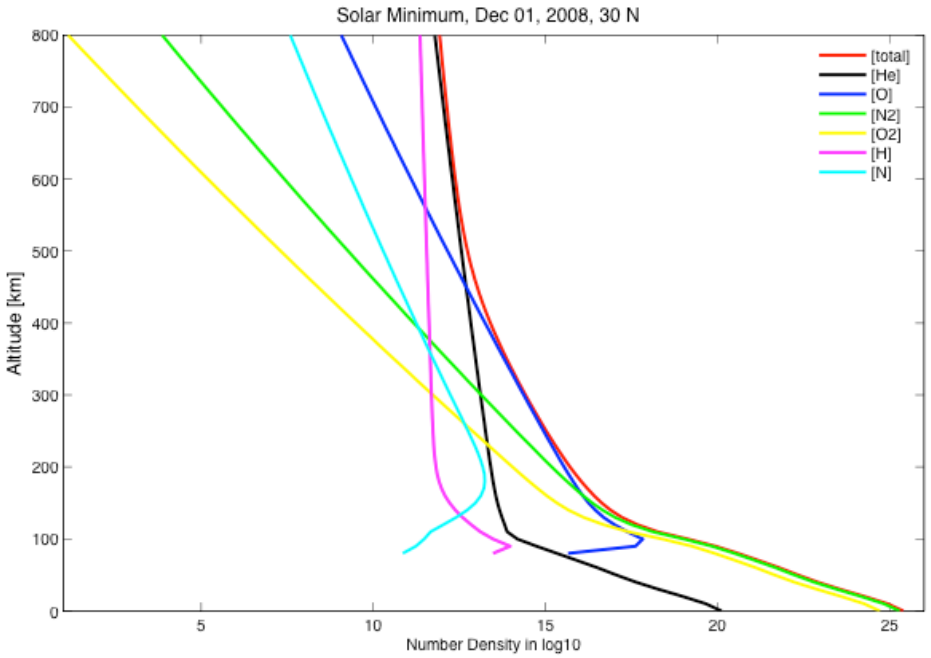

Figure 1.4. Altitude profile of the daily zonal mean number density [m^{-3}] of the thermospheric individual constituents at 30 degree north on Dec 1, 2008.

1.3.3 Governing Equation for Thermosphere Composition

The governing equation for the thermosphere composition distribution shown in Figure 1.4 is discussed in this section. First, let's define different types of velocities:

www.manaraa.com

$\vec{U}$: *Mass – density – weighted average velocity of all the species*

$\vec{U_i}$: *Velocity of the individual species*

$\vec{C_i}$: *The diffusion velocity of individual species*

The relation between these three velocities is,

$$\vec{C_i} = \vec{U_i} - \vec{U} \qquad Eq(1.1)$$

Mass Continuity Equation

The mass continuity equation of the individual species in the gas is,

$$\frac{\partial \rho_i}{\partial t} + \nabla \bullet (\rho_i \vec{U_i}) = P_i - L_i \qquad Eq(1.2)$$

where the first term is the change of density with time, the second term is the divergence of the density flux. The third and fourth terms are the product and loss term of the species.

Subtracting the term $\nabla \bullet (\rho_i \vec{U})$ from both sides of Equation 1.2, the continuity equation results in,

$$\frac{\partial \rho_i}{\partial t} + \nabla \bullet [\rho_i (\vec{U_i} - \vec{U})] = P_i - L_i - \nabla \bullet (\rho_i \vec{U}) \qquad Eq(1.3)$$

Note that the last term in Equation 1.3 can be expanded as,

$$\nabla \bullet (\rho_i \vec{U}) = \nabla \bullet (\frac{\rho_i}{\rho} \rho \vec{U}) = \rho \vec{U} \bullet \nabla (\frac{\rho_i}{\rho}) + \frac{\rho_i}{\rho} \nabla \bullet (\rho \vec{U}) \qquad Eq(1.4)$$

And according to the continuity equation for the total gas,

$$\frac{\partial \rho}{\partial t} + \nabla \bullet (\rho \vec{U}) = 0 \qquad Eq(1.5)$$

If $Eq(1.3) - \frac{\rho_i}{\rho} * Eq(1.5)$, the combined continuity equation can be written as,

$$\frac{\partial \rho_i}{\partial t} - \rho \frac{\partial \rho}{\partial t} + \nabla \bullet [\rho_i (\vec{U_i} - \vec{U})] = P_i - L_i - [\rho \vec{U} \bullet \nabla (\frac{\rho_i}{\rho}) + \frac{\rho_i}{\rho} \nabla \bullet (\rho \vec{U})] + \frac{\rho_i}{\rho} \nabla \bullet (\rho \vec{U})$$

The above equation can be written as,

www.manaraa.com

$$\rho \frac{\partial}{\partial t}(\frac{\rho_i}{\rho}) = -\nabla \bullet (\rho_i \vec{C}_i) + P_i - L_i - \rho \vec{U} \bullet \nabla(\frac{\rho_i}{\rho}) \qquad Eq(1.6)$$

On the right hand size of Equation 1.6, the first term is the divergence of the diffusive flux of the species through the background gas, where $\rho_i \vec{C}_i$ is the diffusive mass flux, which is composed of a molecular diffusion component $\vec{\Gamma}_{Di}$ and an eddy diffusion component $\vec{\Gamma}_{Ei}$. Suppose this is the equation for the minor species, this term can be approximately treated as the divergence of the flux of minor gas diffusing through the major gas. The second and third terms are the chemical production and loss terms of the species. The last term is the advection term that can act as a source or sink of the species depending on the sign of the gradient in mass mixing ratio $(\frac{\rho_i}{\rho})$.

Molecular Diffusive Flux and Momentum Equation

In the following analysis, we will solve for the molecular diffusive flux $\vec{\Gamma}_{Di}$ in the continuity equation (Eq. 1.6) using the momentum equation of the species, defining the diffusion velocity of species *t* as C_t,

$$\nabla P_i - n_i m_i \vec{G} = -n_i m_i \sum_{t \neq i} \upsilon_{it} (\vec{C}_i - \vec{C}_t) \qquad Eq(1.7)$$

The inertial, viscous stress, Coriolis and centrifugal forces are neglected in the momentum equation.

According to Equation 1.7, the diffusive mass flux in the continuity equation can be expressed as,

www.manaraa.com

$$\vec{\Gamma}_{Di} = \rho_i \vec{C}_i = -\frac{1}{\sum_{t\neq i} \upsilon_{it}} (\nabla P_i - \rho_i \vec{G} + \rho_i \sum_{t\neq i} \upsilon_{it} \vec{C}_t) \qquad Eq(1.8)$$

The vertical component of the diffusive mass flux in Equation 1.8 is,

$$\Gamma_D^z = -\frac{D_i m_i}{kT} (\frac{\partial P_i}{\partial z} + \rho_i g + \rho_i \sum_{t\neq i} \upsilon_{it} C_t^z) \qquad Eq(1.9)$$

where D_i is the diffusive coefficient $D_i = \frac{kT}{\sum_{t\neq i} m_i \upsilon_{it}}$. From the ideal gas law, $P_i = kn_i T$, Equation 1.9 can be written as,

$$\Gamma_{Di}^z = -\frac{D_i m_i}{kT} [\frac{\partial}{\partial z} (\frac{\rho_i}{m_i} kT) + \rho_i g + \rho_i \sum_{t\neq i} \upsilon_{it} C_t^z] \qquad Eq(1.10)$$

Expanding the first term of Equation 1.10, and defining the pressure scale height of the species $H_{Pi} = \frac{kT}{m_i g}$. The Equation 1.10 can be further written as,

$$\Gamma_D^z = -D_i [\frac{\partial \rho_i}{\partial z} + \frac{\rho_i}{T} \frac{\partial T}{\partial z} - \frac{\rho_i}{m_i} \frac{\partial m_i}{\partial z} + \frac{\rho_i}{H_{Pi}} + \frac{\rho_i m_i}{kT} \sum_{t\neq i} \upsilon_{it} C_t^z] \qquad Eq(1.11)$$

Because m_i is constant, $\frac{\rho_i}{m_i} \frac{\partial m_i}{\partial z} = 0$.

From Equation 1.11, the vertical molecular diffusion velocity of the species is,

$$C_i^z = -D_i [\frac{1}{\rho_i} \frac{\partial \rho_i}{\partial z} + \frac{1}{T} \frac{\partial T}{\partial z} - \frac{1}{m_i} \frac{\partial m_i}{\partial z} + \frac{1}{H_{Pi}} + \frac{m_i}{kT} \sum_{t\neq i} \upsilon_{it} C_t^z] \qquad Eq(1.12)$$

Diffusive equilibrium holds if the collisional terms in Equation 1.7 are negligible, so that $\frac{\partial P_i}{\partial z} + \rho_i g = 0$, which gives,

$$\frac{\partial \rho_i}{\partial z} + \frac{\rho_i}{T} \frac{\partial T}{\partial z} - \frac{\rho_i}{m_i} \frac{\partial m_i}{\partial z} + \frac{\rho_i}{H_{Pi}} = 0$$

Eddy diffusive flux

www.manaraa.com

Note that the mass continuity equation in the above analysis includes only the diffusive flux term. To account for the eddy diffusion due to turbulent mixing, we need to derive the flux of eddy diffusion in the following analysis. Again looking at the vertical component, suppose k_z is the vertical eddy diffusivity coefficient and the eddy diffusion velocity is,

$$C_{Ei}^z = -k_z \frac{1}{\rho_i / \rho} \frac{\partial(\rho_i / \rho)}{\partial z}$$

The above equation is modified from Schunk and Nagy, Equation 10.57, to satisfy the requirement that $\sum_i \rho_i C_{Ei}^z = 0$, meaning that eddy diffusion produces no net mass transport. Expanding the term on the right hand side,

$$C_{Ei}^z = -k_z [\frac{1}{\rho_i} \frac{\partial \rho_i}{\partial z} - \frac{1}{\rho} \frac{\partial \rho}{\partial z}] \qquad Eq(1.13)$$

According to the hydrostatic equation,

$$\frac{dP}{dz} = -nmg = -\rho g$$

And replacing the pressure P in the hydrostatic equation with $P=nkT$, and $\rho = nm$

$$\frac{\partial(\frac{\rho}{m} kT)}{\partial z} = \frac{kT}{m} \frac{\partial \rho}{\partial z} + \frac{\rho k}{m} \frac{\partial T}{\partial z} - \frac{\rho kT}{m^2} \frac{\partial m}{\partial z} = -\rho g \qquad Eq(1.14)$$

Rearranging the terms in Equation 1.14,

$$\frac{\partial \rho}{\partial z} = -\frac{\rho}{T} \frac{\partial T}{\partial z} + \frac{\rho}{m} \frac{\partial m}{\partial z} - \frac{\rho mg}{kT} \qquad Eq(1.15)$$

Replacing the last term of Equation 1.13 with Equation 1.15, and assuming $H_P = \frac{kT}{mg}$

$$C_{Ei}^z = -k_z [\frac{1}{\rho_i} \frac{\partial \rho_i}{\partial z} + \frac{1}{T} \frac{\partial T}{\partial z} - \frac{1}{m} \frac{\partial m}{\partial z} + \frac{1}{H_P}] \qquad Eq(1.16)$$

Thus, the mass flux due to eddy diffusion in the vertical direction is calculated by,

www.manaraa.com

$$\Gamma_{Ei}^{z} = \rho_i C_{Ei}^{z} = -k_z[\frac{\partial \rho_i}{\partial z} + \frac{\rho_i}{T}\frac{\partial T}{\partial z} - \frac{\rho_i}{m}\frac{\partial m}{\partial z} + \frac{\rho_i}{H_P}] \qquad Eq(1.17)$$

Expanded Mass Continuity Equation

The fluxes in the expanded mass continuity equation now include those due to both molecular diffusion and eddy diffusion. From Equation 1.11 and 1.17, the total flux can be expressed as,

$$\Gamma_i^z = \Gamma_{Di}^z + \Gamma_{Ei}^z = -D_i^z[\frac{\partial \rho_i}{\partial z} + \frac{\rho_i}{T}\frac{\partial T}{\partial z} - \frac{\rho_i}{m_i}\frac{\partial m_i}{\partial z} + \frac{\rho_i}{H_{Pi}} + \frac{\rho_i m_i}{kT}\sum_{t\neq i}\upsilon_{it}C_t^z]$$
$$-k_z[\frac{\partial \rho_i}{\partial z} + \frac{\rho_i}{T}\frac{\partial T}{\partial z} - \frac{\rho_i}{m}\frac{\partial m}{\partial z} + \frac{\rho_i}{H_P}] \qquad Eq(1.18)$$

Then using the total flux in Equation 1.18 and replacing the diffusive flux in Equation 1.8, the mass continuity equation in Equation 1.6, in the vertical direction, can be written in terms of the mass mixing ratio as,

$$\rho\frac{\partial}{\partial t}(\frac{\rho_i}{\rho}) = -\frac{\partial}{\partial z}(\Gamma_i^z) + P_i - L_i - \rho U(z)\frac{\partial}{\partial z}(\frac{\rho_i}{\rho}) \qquad Eq(1.19)$$

Part of the last term of Equation 1.19 can be expanded using Equation 1.15 as,

$$\rho\frac{\partial}{\partial z}(\frac{\rho_i}{\rho}) = \frac{\partial \rho_i}{\partial z} - \frac{\rho_i}{\rho}\frac{\partial \rho}{\partial z} = \rho_i[\frac{1}{\rho_i}\frac{\partial \rho_i}{\partial z} + \frac{1}{T}\frac{\partial T}{\partial z} - \frac{1}{m}\frac{\partial m}{\partial z} + \frac{1}{H_P}] \qquad Eq(1.20)$$

So an expanded mass continuity equation in the vertical direction is

$$\rho\frac{\partial}{\partial t}(\frac{\rho_i}{\rho}) = -\frac{\partial}{\partial z}\{-D_i[\frac{\partial \rho_i}{\partial z} + \frac{\rho_i}{T}\frac{\partial T}{\partial z} - \frac{\rho_i}{m_i}\frac{\partial m_i}{\partial z} + \frac{\rho_i}{H_{Pi}} + \frac{\rho_i m_i}{kT}\sum_{t\neq i}\upsilon_{it}C_t^z] - k_z[\frac{\partial \rho_i}{\partial z} + \frac{\rho_i}{T}\frac{\partial T}{\partial z} - \frac{\rho_i}{m}\frac{\partial m}{\partial z} + \frac{\rho_i}{H_P}]\}$$
$$-U(z)[\frac{\partial \rho_i}{\partial z} + \frac{\rho_i}{T}\frac{\partial T}{\partial z} - \frac{\rho_i}{m}\frac{\partial m}{\partial z} + \frac{\rho_i}{H_P}] + P_i - L_i \qquad Eq(1.21)$$

Example of Use of Expanded Mass Continuity Equation

www.manaraa.com

Using the following definitions:

$$\frac{1}{H^*_{\rho i}} = -\frac{1}{\rho_i}\frac{\partial \rho_i}{\partial z}, \qquad \frac{1}{H_T} = \frac{1}{T}\frac{\partial T}{\partial z}, \qquad \frac{1}{H_m} = -\frac{1}{m}\frac{\partial m}{\partial z}, \qquad H_{Pi} = \frac{kT}{m_i g}$$

Thus $H^*_{\rho i}$ is the actual density scale height that was determined by the density profile of species *i* in vertical direction, in this case, the species *i* could be either in hydrostatic equilibrium, $\frac{dP_i}{dz} = -n_i m_i g$, or not in hydrostatic equilibrium. Similar to Equation 1.15, the density scale height of species *i*, assuming species *i* is in hydrostatic equilibrium, is $\frac{1}{H_{\rho i}} = \frac{1}{H_{Pi}} + \frac{1}{H_{mi}} + \frac{1}{H_{Ti}}$ or $\frac{1}{H_{\rho i}} = \frac{1}{H_{Pi}} + \frac{1}{H_{Ti}}$ because $\frac{1}{H_{mi}} = 0$. The density scale height for the total gas is $\frac{1}{H_\rho} = \frac{1}{H_P} + \frac{1}{H_m} + \frac{1}{H_T}$, where $\frac{1}{H_m} \neq 0$.

Ignoring the chemical production and loss terms, the expanded mass continuity Equation 1.21 can be written as

$$\rho \frac{\partial}{\partial t}\left(\frac{\rho_i}{\rho}\right) = -\frac{\partial}{\partial z}\{-D(z)\rho_i(z)[\frac{1}{H_{\rho i}} - \frac{1}{H^*_{\rho i}} + \frac{m_i}{kT}\sum_{t\neq i}\upsilon_{it}C_t^z] - k(z)\rho_i(z)[\frac{1}{H_\rho} - \frac{1}{H^*_{\rho i}}]\} - U(z)\rho_i(z)[\frac{1}{H_\rho} - \frac{1}{H^*_{\rho i}}] \qquad Eq(1.22)$$

Note that there are three terms that affect the change in the mass mixing ratio of the species: molecular diffusion, eddy mixing and vertical winds on the right hand side of Equation 1.22. Several insights can be gained from Equation 1.22:

(1) The molecular diffusive coefficient, *D(z)*, and vertical wind, *U(z)*, tend to increase with altitude while the eddy diffusive coefficient, *k(z)*, decreases with altitude in the thermosphere. In the lower altitudes, the eddy diffusion term is the dominant term. Around the altitude of the

www.manaraa.com

homopause, the molecular diffusion and eddy diffusion terms are comparable. As altitude increases, the molecular diffusion and vertical wind effect become the dominant terms.

(2) If the eddy diffusion term and vertical wind effect are both close to zero, then the species reaches diffusive equilibrium when the molecular diffusion term is zero. In the upper atmosphere where the eddy diffusion term is negligible, the vertical wind can cause the departure from diffusive equilibrium for minor species.

(3) If the species in discussion is the dominant species, the three density scale heights $H_{\rho i}$, $H^{*}_{\rho i}$ and H_{ρ} in Equation 1.22 are approximately equal. In this case, the dominant species can reach a diffusive equilibrium state.

(4) If the species in discussion is a minor species, the eddy diffusion and vertical wind tendency is to force the minor species density profile with altitude to follow the density scale height of the major species. However, molecular diffusion tries to adjust the density profile of minor species to follow its own density scale height. In order to reach the steady state, the molecular diffusion, eddy diffusion and vertical wind effect have to balance each other.

(5) At the altitudes where the vertical wind effect on the species is significant (this is species dependent but as we will show for helium it is below about 200~250 km), the mean molecular weight gradient in the vertical direction is very small, thus the last term in Equation 1.22 can be written as,

$$-U(z)\rho_i(z)[\frac{1}{H_\rho}-\frac{1}{H^{*}_{\rho i}}]\approx -U(z)\rho_i(z)[\frac{1}{H_P}+\frac{1}{H_T}-\frac{1}{H_{Pi}}-\frac{1}{H_{Ti}}]\approx -\frac{U(z)\rho_i(z)}{H_P}[1-\frac{m_i}{m}] \qquad Eq(1.23)$$

www.manaraa.com

If $m_i < m$, an upward vertical wind (positive) would act as a sink for the lighter minor species like hydrogen (H) and helium (He). The major species are less sensitive to the vertical wind because $m_i \approx m$ for the major species

(6) Similar to the vertical wind effect, the eddy diffusion term can be written as,

$$k(z)n_i(z)[\frac{1}{H} - \frac{1}{H_i^*}] = \frac{k(z)\rho_i(z)}{H_P}[1 - \frac{m_i}{m}]$$

Where the eddy diffusion is important, a gas like helium (He) would be forced downward by eddy diffusion to make the gas mixing ratio fixed with height, because the eddy diffusion velocity $C_{Ei}^z = \frac{k_z}{H_P}(\frac{m_i}{m} - 1) < 0$. The change in the major gas N_2 altitude distribution is less affected by these processes near the homopause of the atmosphere as its individual molecular weight is close to the mean molecular weight of the total gas.

1.3.4 Thermosphere Dynamics

The most important parameters that control the thermosphere composition are: the thermosphere temperature profile, the altitude of the turbopause, dynamics (air motions) and photochemistry [*Reber,* 1976]. However, which parameter is more dominant is dependent on the species and the altitude. Heavier species such as N_2 are more sensitive to temperature change because a certain change in temperature results in a larger concentration change in the heavier species (such as N_2) than that in the lighter species (such as He). The lighter species are more sensitive to the turbopause altitude, which is closely related to the eddy diffusion coefficient. The sensitivity of an individual species to the eddy diffusion coefficient change is a function of the ratio of its atomic mass relative to the atmosphere mixed mean mass. Thus, given that the

www.manaraa.com

atmosphere mixed mean mass is ~28.95 amu near the turbopause, He (4 amu) experiences a larger change due to the turbopause variation than that of N_2 (28 amu) [*Reber,* 1976].

The impact of dynamics (air motions) on an individual species is also a function of its atomic mass relative to the atmosphere mixed mean mass, such that upward air motions tend to decrease the concentration of species whose molar mass is smaller than the atmosphere mean molar mass (~28.95 amu) and increase those whose molar mass is greater than the atmosphere mean molar mass [*Reber,* 1976]. N_2 and O are more photochemically active than He. Helium is an inert gas and its photochemistry can be ignored. The temperature structure of the thermosphere is one of the most important properties for defining the thermosphere preconditioned state.

1.3.5 Escape of the Atmosphere

At the exobase (about 500-800 km on the earth), the mean free path of the particles between collisions is equal to the gas scale height. This marks the transition from a collisional gas to a collisionless gas and constituents of the atmosphere traveling upward in the thermosphere can escape out to space without colliding. The region above the exobase is called the exosphere. The escape condition is met when the kinetic energy of the gas exceeds the gravitational potential energy. Thus, higher temperatures and lighter species will be able to escape most easily and constitute the greatest flux. This describes thermal escape or Jeans escape flux mechanism. For the same species, the Jean's escape flux is larger during solar maximum than during solar minimum.

The lighter species such as He and H have much larger Jean's escape flux than the heavier species N_2 and O. From the first principle of thermal escape equation, for similar conditions,

www.manaraa.com

hydrogen thermal escape is about six orders of magnitude greater than helium. Hydrogen is also more susceptible to charge exchange and polar wind processes producing additional escape flux not experienced by helium. Thus, He thermal escape is not a significant effect on the vertical distribution of He through the thermosphere. The flux due to the non-thermal escape is on the order of 10^7 cm^2s^{-1}, one order less than the thermal escape flux.

1.3.6 Thermosphere Measurements

The types of measurement of thermosphere density and composition include: (1) satellite drag data derived from satellite orbital decay; (2) mass density data from microphone gauge, pressure gauge and accelerometer measurements; (3) mass spectrometer data and (4) optical data based on remote sensing of airglow and auroral emissions and solar and stellar radiation extinction measurements [*Prölss,* 2011]. The types of measurements can be also divided into *in situ* measurements and remote sensing measurements. Many studies have already included the descriptions of the mass density measurements, thus the composition measurement is of interest in this study. The *in situ* composition measurements include mass spectrometers on board satellites or rockets. The mass spectrometers use an electron beam to ionize the sample atmosphere. Through calculating the number of the ions generated by the ionization, the concentration of each constituent of the sample gas can be determined [*Spencer,* 1988]. Almost all of the thermosphere neutral mass spectrometer measurements were made between 1969-1983. These include measurements by the Orbiting Geophysical Observatory (OGO) 6, San Marco satellite 3, Aeros-A, ESRO 4 satellite, Atmosphere Explorer (AE)-C, D, E satellites and the Dynamic Explorer (DE) satellite. The gasses measured by these satellites include N_2, O, He, Ar.

www.manaraa.com

Some satellites also measured O_2 and H. These measurements covered the altitudes ranging from 100 km to 700 km, but with very sparse resolution in both space and time. Rocket experiments provide infrequent, point measurements of the neutral composition distribution with altitude profile. Most of our understanding about the neutral composition below 200 km comes from rocket measurements [*Offermann,* 1974]. There were few measurements of composition and density (above 200 km) during the time period between 1991 and 2001 [*Emmert et al.,* 2006]. However, a new generation of remote-sensing methods using the ultraviolet ariglow technique provides accurate imaging of composition and other thermosphere properties. The far ultraviolet (FUV) imaging from the Global Ultraviolet Imager (GUVI) on board the Thermosphere Ionosphere Mesosphere Energy and Dynamics (TIMED) satellite was used to infer column O/N_2 ratios in nadir-viewing [*Strickland et al.,* 2004] and altitude profiles of O, N_2 and O_2 density from in limb-viewing, respectively [*Emmert et al.,* 2006]. Although a useful contribution to understanding thermosphere composition, these measurements did not contribute to understanding the lighter species of helium and hydrogen. Most of the direct and inferred measurements of helium is from the late 1960's and early 1980's [*Emmert et al.,* 2006].

1.4 Thermosphere Disturbed State

The thermosphere is highly dynamic and regularly disturbed by enhanced solar EUV fluxes due to flares, solar wind field structure, energetic particle precipitation from the magnetosphere, Joule heating through thermosphere/ionosphere coupling, and the various waves propagating from below. This thesis focuses on the geomagnetic storm disturbance associated with the solar

www.manaraa.com

wind field structure, and the energy dissipated through Joule heating and particle precipitation. *Prölss* [2011] summarized the general morphology of thermosphere density during the geomagnetic storm from the literature as:

- Usually, even small enhancements of geomagnetic activity are indicated in the upper thermosphere mass density perturbations. The perturbations may become significant during geomanetic storms.
- Usually, there is a lag of the thermosphere density response to the geomagenetic storm onset by several hours.
- The thermosphere density perturbation due to geomagnetic activity can be observed on a global scale.
- The amplitude of the density pertubation increases with altitude if the associated heating is deposited in the lower thermosphere.

1.4.1 Categories of the geomagnetic storms

The types of geomagentic activity can be broadly divided into coronal mass ejections (CMEs) and corotating interaction regions (CIRs). CMEs are associated with the large clouds of material ejected from the Sun's corona at a very high outward speeds [*Kahler*, 1992]. The shock waves associated with CMEs accelerate interplanetaray particles, interact with the Earth's magnetosphere and cause geomagnetic storms [*Baker et al.,* 1998]. The shock, sheath, ejecta and geomagnetic cloud induced by CME are the various components that cause the CME-driven storm [*Borovsky and Denton,* 2006]. CIRs are connected with the interaction of high-speed and low-speed solar winds. The CIR itself or the high-speed solar wind or both can be the source of

www.manaraa.com

CIR-driven storms.

Borovsky and Denton [2006] provided a detailed comparision of the difference between CMEs-driven storms and CIRs-driven storms. The CME-driven storms occur often in the solar maximum [*Webb,*1991; *Richardson et al.,* 2001; *Yashiro et al.*, 2004] while the CIR-driven storms tend to occur during the late declining phase of the solar cycle [*Mursula and Zeiger,* 1996; *Richardson et al.,* 2001]. The CME storms are irregular and non-recurring while the CIRs storms usually have 27-day recurrence, or subharmonic periods of 27 days, due to the rotation of the Sun [*Borovsky and Denton*, 2006]. The geomagnetic disturbance driven by a CME is usually stronger than that driven by a CIR. However, the CIR storm tends to have a longer main phase than a CME storm, whose integrated effect on the thermosphere can exceed that of CME storms [Turner et al., 2006].

1.4.2 Geomagnetic indices

In order to categorize the disturbance level in the upper atmosphere due to a geomagnetic storm, the geomagnetic indices are used. The K_p index is one of the most widely used geomagnetic indices. The K_p is a 3-hour interval average of the irregular disturbance in the horizontal component of the earth's geomagnetic field from 13 observatories measured at mid-latitudes between 48°N and 63°S. The value of K_p ranges from 0.0 to 9.0, with 1 being quiet and >5 being a strong geomagnetic storm. The scale of K_p is quasi-logarithmic. The a_p index is used as a linear substitute for K_p. A_p index is the daily average of the a_p index. The following table gives a conversion between K_p and a_p:

www.manaraa.com

K_p	0	1	2	3	4	5	6	7	8	9
a_p	0	3	7	15	27	48	80	140	240	400

[http://spidr.ngdc.noaa.gov/spidr/help.do?group=geomInd]

1.4.3 Dependence of geomagnetic disturbance on precondition state

The ability to determine how thermosphere mass density responds to energy input is of critical importance. However, the response also depends on the type of energy input, the altitude distributuion of the energy in the thermosphere, and the initial state of the thermosphere prior to being perturbed, that is, the precondition state of the thermosphere. To tackle this issue requires analysis of multiple types of observations over extended periods of time and numerical simulations of the thermosphere / ionosphere system

As illustrated in Figure 1.5 from an NCAR-TIEGCM simulation, the relative change in mass density at a fixed altitude, 400 km, is greater at solar minimum than at solar maximum given the same amount of geomagnetic energy deposited in each case [*Lei et al.,* 2011]. Thus, in terms of relative change in mass density, the state of the thermosphere prior to geomagnetic activity (i.e., the preconditioned state) is important.

This behavior was confirmed observationally by the statistical study of N_2 perturbations in the polar oval during geomagnetic active periods using the ESRO-4 satellites measurements [*Trinks and von Zahn,* 1975]. See Figure 1.6. The data were normalized to an altitude of 270 km, where O and N_2 are the main species, thus the variation of the N_2 density in some aspects can represent the total mass density perturbations. Figure 1.6 shows the perturbation of N_2 density

www.manaraa.com

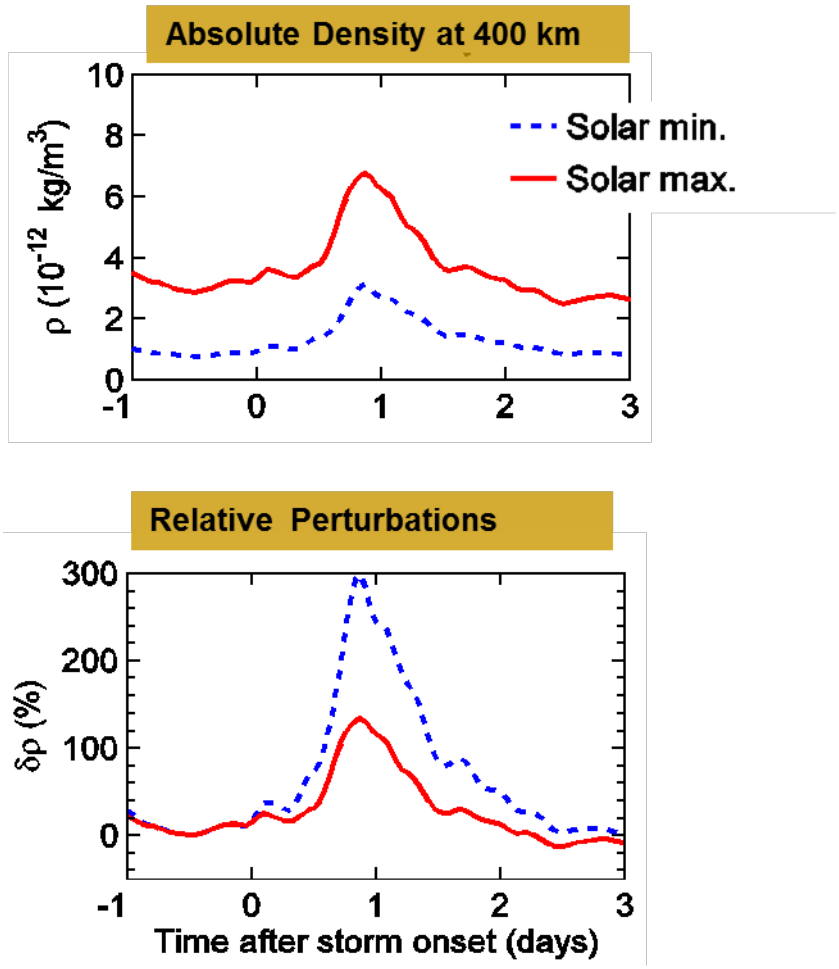

Figure 1.5. The absolute and relative change in mass density at 400 km for the same energy deposition by a geomagnetic storm during solar minimum vs. solar maximum.

response to the magnetic activity index changes, which represent the energy input to the polar heating zone during the geomagnetic active period. This statistical study suggested a higher disturbance in N_2 density during the winter than summer, and higher during low solar activity than during high solar activity for the same geomagnetic energy input. The explanation for a higher relative density perturbation in solar minimum than in solar maximum is that the density perturbation at a fixed altitude is the integral of all the density scale height change below this fixed altitude. Due to the colder temperature, there are more density scale heights integrated

www.manaraa.com

below the fixed altitude in solar minimum than in solar maximum and thus tend to have a larger density scale height perturbation in solar minimum *[Lei et al., 2010]*.

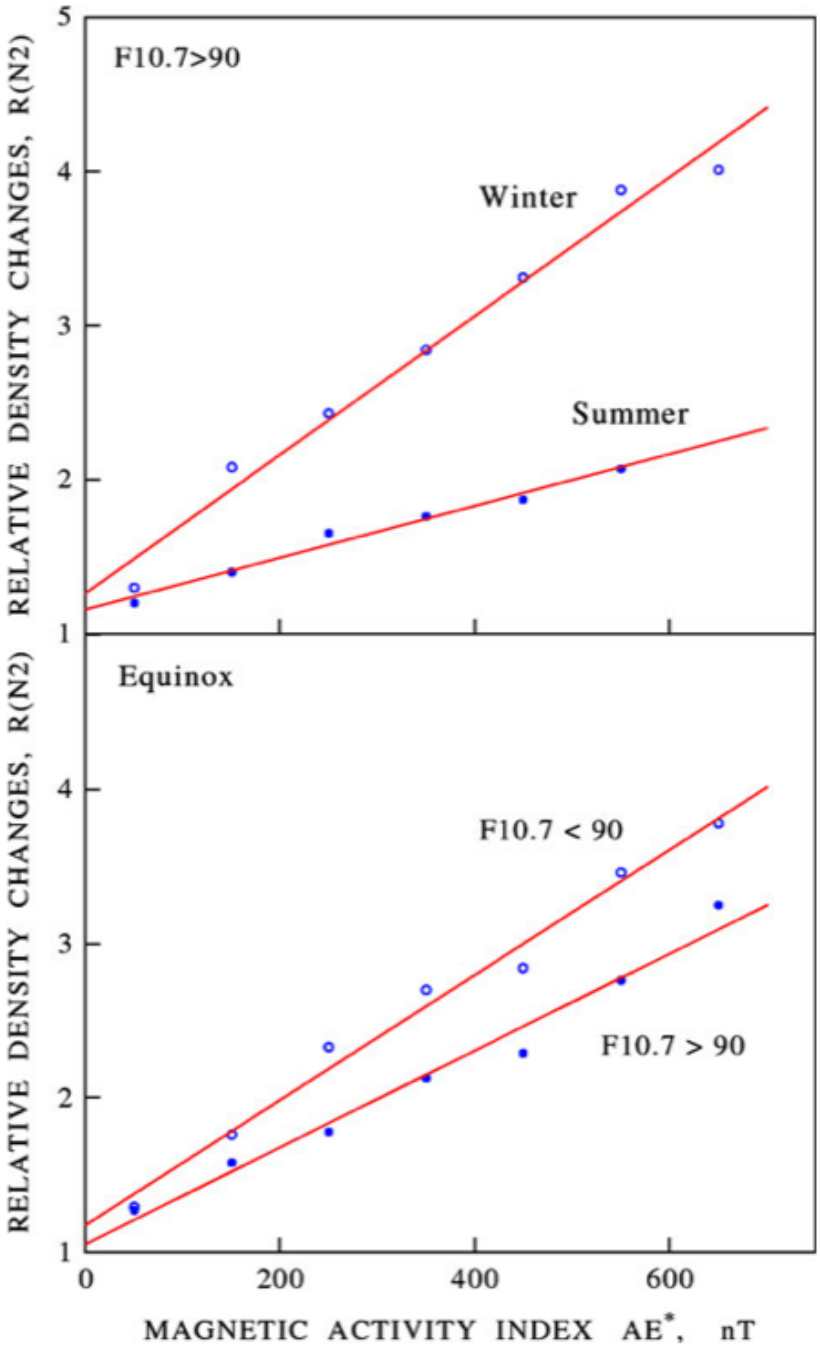

Figure 1.6. The response of the molecular nitrogen density to geomagnetic activities in difference seasons and solar activities. The N_2 data is measured by ESRO-4 satellite and normalized to 270 km. [*Prölss,* 2011]

www.manaraa.com

1.4.4 Thermosphere composition response to geomagnetic forcing

The mass density change is the combined result of changes to each thermosphere species; which will have its own way of change compared to the other species, and the temperature of the gas. At an altitude of 300 km, the heavier species argon (Ar) and molecular nitrogen (N_2) generally increase with increasing geomagnetic activity in the mid and high latitudes. In addition, a substantial depletion in lighter species helium (He) and relatively small decrease in oxygen (O) will occur. This was observed by the ESRO-4 satellite at 280 km where O is the main constituent of the atmosphere as illustrated in Figure 1.7. The bottom panel shows the mass density perturbation, the sum of the changes in all the species, is relatively flat over the latitude. The relative density is larger than 1, which suggests that the density increased during geomagnetic disturbance over all the latitudes but modified by composition change.

There are three mechanisms for the composition change during a geomagnetic storm discussed in the literature: thermal expansion, atmospheric mixing, and upwelling of air [*Johnson*, 1964; *Prölss*, 2011]. The thermal expansion is the rise of the constant pressure level owing to the temperature enhancement during the geomagnetic active period. According to the analysis of *Bates* (1974a,b), a large fraction of polar heating is transferred through thermal expansion of the thermosphere. Note that during the thermal expansion, the amount of the atmospheric gas above the given pressure level is unchanged and no air gas is moving across the pressure level [*Rishbeth and Müller-Wodarg,* 1999], thus the thermal expansion would cause the atmosphere composition change at the fixed altitude, but not at the fixed pressure level. Indeed,

www.manaraa.com

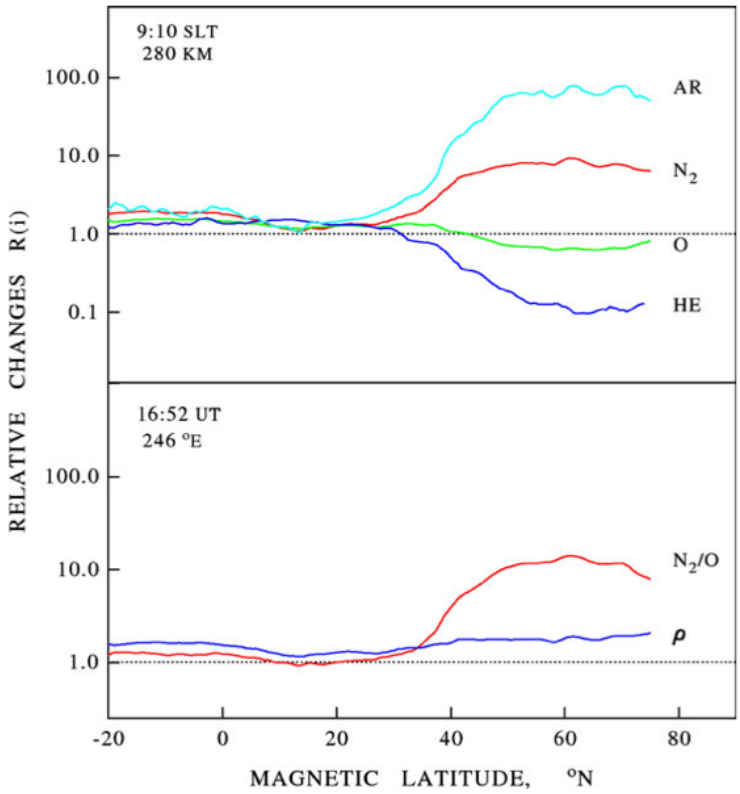

Figure 1.7. The latitudinal variation of the composition and density perturbation during the geomagnetic storm in October 29, 1973 at 09 solar local time. The top panel shows the relative changes in argon (Ar), molecular nitrogen (N_2), atomic oxygen (O) and helium (He) densities referred to the prestorm conditions and normalized to 280 km [*Prölss,* 2011].

the DE-2 satellite data illustrated that the perturbation of composition is observed not only at a fixed altitude but also at a constant pressure level of 10^{-5} Pa (*Prölss*, 1992), which suggests that thermal expansion is not the only mechanism for the storm time composition change.

Reber and Nicolet [1965] reported that the composition change cannot be explained only by temperature increase. They concluded that the increase of the homopause altitude due to the enhancement of turbulence and mixing in the lower atmosphere during the storm time may be part of the mechanism. However, *Prölss* [2011] pointed out the time for the composition perturbation propagating from lower atmosphere to upper atmosphere takes on the order of days.

www.manaraa.com

The upwelling of the gas driven by the wind circulation is the most popular explanation for the composition perturbations [*Prölss*, 2011]. *Mayr et al.* [1978] introduced the concept of wind-induced diffusion with heavier species N_2 and lighter species He as an example. In order to maintain the mass flux continuity, the N_2 velocity is slower than helium velocity in the lower thermosphere, and the velocities of both constituents increases with altitude, however the velocity of N_2 increases faster than the velocity of He because the N_2 concentration decreases faster than the He concentration. Thus, there is a frictional force between the two gases that causes the faster upward He to be dragged down by the N_2 in the lower thermosphere. This 'diffusion barrier' causes an enhancement of heavier constituent N_2 and a depletion of lighter species He. Another way to look at the mechanism of the upwelling of the gas is that adding the frictional forces changes the vertical pressure gradient of the gas in order to balance the force in the vertical direction, thus causing the density to not be in diffusive equilibrium. A last way to look at the upwelling does not require collisions between two constituents. Both species are assumed to move in the same direction with the same velocity. Note that the mass mixing ratio of N_2 decreases with altitude and He increases with altitude. The upward wind due to the divergence of the horizontal winds lifts the air rich in N_2 and poor in He up and causes the composition perturbations [*Shimazaki* 1972; *Hays et al.* 1973].

1.4.5 Thermosphere mass density change at fixed altitude and fixed pressure level

Thermosphere mass density changes at fixed altitudes are more complicated than the mass density changes at fixed pressure level. The thermosphere mass density at fixed altitude involves both the thermal expansion and the upwelling of gas. The mass density change at fixed pressure

www.manaraa.com

level are related to temperature and mean molecular weight changes.

According to the ideal gas law and hydrostatic equation:

$$P = nkT\,, \qquad \frac{dP}{dZ} = -\rho g$$

the general concept of scale height has been applied to assist in the interpretation. The pressure scale height relates to the change in pressure with altitude using the hydrostatic law in the general form as, $H_P = -P/(dP/dz)$. According to Equation 1.14, the pressure scale height can be expanded, using the ideal gas law, into the form

$$H_P = \frac{1}{\frac{1}{m}\frac{dm}{dz} - \frac{1}{\rho}\frac{d\rho}{dz} - \frac{1}{T}\frac{dT}{dz}} \tag{1.24}$$

where m is the molar mass or mean molecular weight of the total gas, ρ is the mass density, and T is the temperature at a given altitude. Density, temperature, and mean molecular weight scale heights can be expressed, using the same general form as pressure scale height, as

$$H_\rho = \frac{-\rho}{d\rho/dz}\;; \qquad H_T = \frac{T}{dT/dz}; \qquad H_m = \frac{-m}{dm/dz} \qquad Eq(1.25)$$

where the sign of all scale height values is kept positive. This leads to a compact form of the pressure scale height given in Equation 1.24 as,

$$H_P = \frac{1}{\frac{1}{H_\rho} - \frac{1}{H_m} - \frac{1}{H_T}} \qquad Eq(1.26)$$

The mass density at fixed altitude can be related to the density scale height, H_ρ, by taking the integral of the density scale height relation in Equation 1.25 over the altitude range between the reference altitude and the fixed altitude,

www.manaraa.com

$$\ln\left(\frac{\rho}{\rho_0}\right)=\int_{z_0}^{z}\frac{-dz}{H_\rho}$$

where z_0 is the reference altitude. Thus the density at quiet and active times can be written as,

$$\frac{\rho^Q}{\rho_0^Q}=\exp\int_{z_0}^{z}\frac{-1}{H_\rho^Q}dz$$

$$\frac{\rho^S}{\rho_0^S}=\exp\int_{z_0}^{z}\frac{-1}{H_\rho^S}dz$$

where the superscript Q stands for 'Quiet' and S stands for 'Storm'. The relative density change during the storm time can be expressed as,

$$\frac{\rho^S}{\rho^Q}=\frac{\rho_0^S}{\rho_0^Q}\exp\int_{z_0}^{z}(\frac{1}{H_\rho^Q}-\frac{1}{H_\rho^S})dz$$

If the perturbation δ is defined as (Storm/Quiet -1), the density perturbation at fixed altitude z can be written as,

$$\frac{\rho^S}{\rho^Q}-1=(\frac{\rho_0^S}{\rho_0^Q}-1+1)\exp\int_{z_0}^{z}(\frac{H_\rho^S-H_\rho^Q}{H_\rho^Q}\frac{1}{H_\rho^S})dz-1$$

which is,

$$\delta\rho=(\delta\rho_0+1)\exp\int_{z_0}^{z}(\delta H_\rho\frac{1}{H_\rho^S})dz-1 \qquad Eq(1.27)$$

Thus the density perturbation $\delta\rho$ at a fixed altitude is relative to the density perturbation at reference altitude $\delta\rho_0$ and the integral of all the changes of the density scale height weighted by storm time density scale height $\delta H_\rho\frac{1}{H_\rho^S}$ below the fixed altitude.

The density change at fixed pressure level is simpler than at fixed altitude. According to the ideal gas law and mass density equation,

www.manaraa.com

$$P = nkT = \frac{\rho}{m} kT$$

where k is the Boltzman constant. The pressure in quiet and active periods can be written as,

$$P^Q = \frac{\rho^Q}{m^Q} kT^Q$$

$$P^S = \frac{\rho^S}{m^S} kT^S$$

Because of the fixed pressure level, thus

$$P^Q = P^S$$

So the change in mass density at fixed pressure level can be written as,

$$\frac{\rho^S}{\rho^Q} = \frac{m^S}{m^Q} / \frac{T^S}{T^Q}$$

The change in the mass density at fixed pressure level is proportional to the mean molecular mass density and inversely proportional to the temperture change.

1.5 Data and Models

1.5.1 CHAMP

The CHAMP (CHAllenging Minisatellite Payload) satellite was launched in July 15, 2000 with an initial altitude of 454 km. The mission ended in September 19 2010, with 58277 orbits of measurements in ten years. The satellite was in a near polar orbit with a high inclination angle of 87.3°, which enabled the satellite to make measurements from pole to pole at different local times. The primary science objectives of CHAMP were the recovery of the gravity and magnetic fields of the Earth and electric field investigations. The payload of the satellite included a magnetometer, accelerometer, star sensor, GPS receiver, laser retro reflector and an ion drift

www.manaraa.com

meter. The data from the accelerometer, which is of particular interest in this study, is used to obtain the thermosphere density.

In this study, the mass density is calculated from acceleration, attitude and orbit ephemeris data provided by the CHAMP Information System and Data Center using standard methods [*Sutton et al.,* 2005, 2007]. The sampling rate of the accelerometer data is 0.1 Hz, which is corresponding to an in-track resolution of ~80 km. The altitude variations in this period studied in this paper are around 350 km.

1.5.2 GRACE

The Gravity Recovery and Climate Experiment (GRACE) is a joint project of NASA and the German Center for Air and Space Flight. The GRACE mission includes two identical spacecraft, GRACE-A and GRACE-B, flying about 220 km apart, and launched into a near-circular 89.5° inclination orbits at 500 km in March 2002 [http://www.csr.utexas.edu/grace/overview.html]. The science objective of the GRACE mission is to accurately map the Earth's gravity field variations. These two spacecraft in this mission are connected by a K-band microware link which can determine the gravity difference through measuring the change of their relative speed and the distance [*Showstack,* 2002].

In this study, the mass density is calculated from the GRACE accelerometer measurements using standard methods [*Sutton et al.,* 2005, 2007]. The sampling rate of the accelerometer data is 1 Hz. The mass densities obtained from GRACE B have very similar variation pattern with that from GRACE A. Thus in this study, only the mass density from the GRACE A is presented.

www.manaraa.com

1.5.3 NRL-MSISE00

The NRLMSISE-00 model [*Picone et al.*, 2002] is an empirical model of the atmosphere. The word 'MSIS' stands for two primary data sources: Mass Spectrometer and Incoherent Scatter Radar, and the word 'E' in the name means that the altitude that the model can cover has been extended from the ground to space. Besides the traditional mass spectrometer and radar databases, the NRLMSISE00 model also takes in the total mass density data derived from satellite drag.

The inputs of the model include solar extreme ultraviolet (EUV) specified in $F_{10.7}$ index and geomagnetic condition indicated by A_p index. The outputs of the model are temperature, composition and total mass density.

1.5.4 NCAR TIEGCM Model

The Thermosphere Ionosphere Electrodynamics General Circulation Model (TIEGCM) by the National Center for Atmospheric Research (NCAR) is a 4D numerical simulation of the Earth's upper atmosphere. The model calculates the dynamics, electrodynamics, photoionization, neutral gas heating, and the compositional structure of the middle and upper atmosphere [*Roble et al.,* 1988; *Richmond et al.,* 1992]. The model simulation covers from approximately 97-500 km in the vertical with a 5° x 5° latitude-longitude grid.

The input parameters for the TIEGCM model include: (1) solar input, i.e., $F_{10.7}$ and $F_{10.7}$ A; (2) magnetospheric input in the form of auroral particle precipitation specified by hemispheric power which is obtained from 3 hour K_p index; and the imposed magnetospheric electric field provided by Heelis model [*Heelis et al.,* 1982] or Weimer model [*Weimer*, 1996]; (3) low

www.manaraa.com

boundary condition, i.e., tides from the lower atmosphere specified by the Global Scale Wave Model (GSWM) [*Hagan and Forbes*, 2002]. The output of the model includes temperatures (ion, neutral, and electron), neutral winds (zonal, meridional, and vertical), composition (major/minor species density), ion and electron temperature and densities and dynamo electric field.

www.manaraa.com

Chapter 2 Observations of Thermosphere Mass Density Response and Inferred Composition Effect

In this Chapter, high-resolution mass density observations derived from accelerometer measurements on the CHAMP and GRACE satellites are employed to investigate the thermosphere mass density response with latitude and altitude to geomagnetic activity during the recent solar minimum. The preconditioned state of a cold and contracted thermosphere during this solar minimum resulted in a predominance of helium in the winter hemisphere near the altitude of the GRACE satellite (~475 km). Solar wind high speed streams were the dominant source of geomagnetic activity. Coplanar orbital periods of CHAMP (~330 km) and GRACE (~475 km) in February 2007 and December 2008 revealed the latitude response in thermosphere mass density at two altitudes separated by about 145 km. Their differing response to geomagnetic activity in the winter hemispheres led to the conclusion that different composition structure and dynamic response at the two different altitudes must be the cause.

Therefore, this chapter investigates the role of composition in explaining observed mass density response to geomagnetic activity near the O to helium transition region during this recent solar minimum.

2.1 Solar Minimum of Cycle 23/24

The cold thermosphere during the recent solar minimum between cycles 23 and 24, extending from 2007 to 2010, led to atmospheric contraction [e.g., *Emmert et al.*, 2010] where

www.manaraa.com

small constituent scale heights result in a more rapid transition from heavy to light neutral species with altitude. This contraction of neutral species and their constituent transport can cause structure in both latitude and altitude of the thermosphere mass density due to changes in the mean molecular weight of the gas. Evidence for the presence of a significant amount of helium in the winter hemisphere this solar minimum at an altitude near 476 km was provided by *Bruinsma and Forbes* [2010]. They based their assessment of helium on anomalous behavior in mass density using satellite accelerometer measurements – anomalous referring to deviations in mass density away from expected behavior due to temperature – in a manner similar to that of the original *Keating and Prior* [1968] satellite drag observations, who coined this inferred abundance in helium as the "winter helium bulge". *Haaser et al.* [2010] also suggests a significant amount of helium present at equatorial latitudes near 400 km altitude this solar minimum based on indirect assessments of measurements made by the neutral wind meter on the C/NOFS satellite and through a satellite-drag analysis of the C/NOFS satellite orbital characteristics.

Although 2008 had extremely low solar EUV fluxes [*Solomon et al.*, 2011], geomagnetic activity due to solar wind disturbances continued [*Lei et al.*, 2011], albeit weaker than in previous years [*Tsurutani et al.*, 2011]. Thus, the preconditioned, contracted state of the thermosphere in 2008, with an abundance of helium, will cause the mass density response to geomagnetic activity for altitudes above about 400 km to be highly dependent on composition. This unique condition can be investigated by the high-spatial resolution mass density estimates

www.manaraa.com

from the accelerometers onboard the CHAMP (Challenging Mini-satellite Payload [*Reigber et al.*, 2000; *Lühr et al.*, 2004]) and GRACE (Gravity Recovery and Climate Experiment [*Tapley et al.*, 2004]) satellites during times of near coplanar orbits.

Composition affects on mass density structure during geomagnetic activity due to the redistribution of O/N_2 has been demonstrated through simulation [e.g., *Lei et al.*, 2010; *Qian et al.*, 2010], but this affect is difficult to discern from mass density observations from a single altitude. To interpret the observations, *Lei et al.* [2010] simulated mass density structure at 400 km altitude during a large geomagnetic storm in November 2004 and illustrated significant deviations in density response from that expected by temperature structure alone. The simulation indicated that significant constituent transport, both vertically and horizontally, of N_2 relative to O at 400 km led to scale height modifications that suppressed mass density changes. In this simulation, the impact of the composition change at high latitudes resulted in suppressing the mass density response that would have been enhanced by 150% if based solely on temperature. *Qian et al.* [2010] simulated similar composition effects on mass density at 400 km for weaker recurrent geomagnetic storms associated with coronal high speed streams and also found that the O/N_2 composition changes suppressed mass density response to geomagnetic activity. Thus, in general, when composition changes at a fixed altitude during a geomagnetic storm the effect on mass density is to suppress the amount of change.

The TIMED/GUVI observations have provided a significant database of O/N_2 behavior through the recent solar cycle [*Zhang and Paxton*, 2011] to assist in the interpretation of mass density changes to geomagnetic activity [e.g., *Lei et al.*, 2010] near the N_2 to O transition

www.manaraa.com

altitude. The O to He behavior in the upper thermosphere at solar minimum has not been observed since the 1970's through measurements made by the Dynamics Explorer satellites [*Carignan et al.*, 1981]. The O to He transition behavior is far less understood, and the transition is at a much lower altitude than normal during this extreme solar minimum in 2008. Furthermore, the effect of the structure in the O to He transition on mass density will be more acute than the N_2 to O transition because of the greater relative change in mean molecular weight. As will be shown, this structuring can dominate the effects due to temperature during this period.

This thesis employs the CHAMP and GRACE accelerometer estimates of mass density during time periods when the two satellites were in common local time planes, but separated in altitude by approximately 145 km, to investigate the thermosphere mass density response to geomagnetic activity at two different altitudes

Bruinsma and Forbes [2010] have shown that there were four time periods when the CHAMP and GRACE satellites were in common local time planes during their concomitant lifetimes. We use the two, month-long, time periods of February 2007 and December 2008 to evaluate the mass density response to geomagnetic activity, with February 2007 representing modest solar minimum conditions and December 2008 representing extreme solar minimum conditions. The February 2007 period is centered near the 10/22 local time (LT) plane and the December 2008 period is centered near the 8 / 20 local time plane.

www.manaraa.com

2.2 CHAMP to GRACE Mass Density Ratio

CHAMP and GRACE accelerometer measurements were evaluated to estimate mass density using the most recent analysis scheme by *Sutton* [2009] which accounts for gas-surface interactions along the elongated shapes of the CHAMP and GRACE satellites. The mass density values were averaged into 3-degree latitude bins and normalized to their respective mean satellite altitudes using the NRLMSISE-00 model [*Picone et al.*, 2002]. The NRLMSISE-00 model is employed to normalize the CHAMP and GRACE mass density to their respective normalized altitudes as follows: $\rho_{h_{norm}} = \rho_h * \rho_{h_{norm}}^{MSIS} / \rho_h^{MSIS}$, where the subscript h_{norm} corresponds to the normalized altitudes, which are near the satellite's respective mean altitude over the orbits, the subscript h is the satellite's altitude in each orbit, and superscript *MSIS* represents the output provided by the NRL-MSISE00 model. The normalized GRACE mass density values, ρ_G, and the normalized CHAMP mass density values, ρ_C, for each 3-degree latitude resolution incremement along the respective satellite orbits were used here to investigate the latitude and altitude behavior in thermosphere mass density. The density percent error, based on the analysis by *Sutton et al.* [2007], for these times periods were estimated to be less than 10%.

Given the unique opportunity to observe the density change at two different altitudes, the general concept of scale height has been applied to assist in the interpretation. The observed CHAMP-to-GRACE (C/G) mass density ratio can be related to the density scale height, H_ρ, by taking the integral of the density scale height relation in Equation 1.25 in Chapter 1 over the altitude range between the CHAMP and GRACE satellites, i.e., $\ln\left(\frac{\rho_G}{\rho_C}\right) = \int_{z_C}^{z_G} \frac{-dz}{H_\rho}$. Taking the

www.manaraa.com

average of the integrand, the height-averaged reciprocal of the density scale height can be estimated from the C/G mass density ratio measurements as $\left\langle \frac{1}{H_\rho} \right\rangle = \frac{1}{z_G - z_C} \ln\left(\frac{\rho_C}{\rho_G} \right)$. Expanding the approach used to arrive at equation (1.26), the height-averaged reciprocal in density scale height can be expressed as,

$$\left\langle \frac{1}{H_\rho} \right\rangle = \left\langle \frac{1}{H_P} \right\rangle + \left\langle \frac{1}{H_M} \right\rangle + \left\langle \frac{1}{H_T} \right\rangle \qquad Eq(2.1)$$

where the symbol < > refers to the average of the integrand over the altitude range between CHAMP and GRACE. In general, the height average of the reciprocal scale height will not be equal to the reciprocal of the height-averaged scale height. Throughout this thesis we will be using the height average of the reciprocal scale height in the analysis. However, when the temperature and mean molecular weight do not change significantly with height, the density scale height will be equal to the pressure scale height. Otherwise, the height-averaged reciprocal in density scale height will always be greater than the height-averaged reciprocal in pressure scale height due to the contributions from the temperature and molecular weight scale heights.

This scale height formulation will be helpful in interpreting the observed C/G mass density ratio because we can rewrite Equation 2.1, based on the observations and the hydrostatic law, as

$$\frac{1}{z_G - z_C} \ln\left(\frac{\rho_C}{\rho_G} \right) = \left\langle \frac{1}{H_P} \right\rangle + \left\langle \frac{1}{H_M} \right\rangle + \left\langle \frac{1}{H_T} \right\rangle = \left\langle \frac{Mg}{RT} \right\rangle + \left\langle -\frac{d \ln M}{dz} \right\rangle + \left\langle \frac{d \ln T}{dz} \right\rangle \qquad Eq(2.2)$$

where R is the universal gas constant, g is the gravitational acceleration, and M is the mean molecular weight at a given altitude. This relation will be exploited to interpret the C/G ratio observations and can be described in terms of height-averaged reciprocal scale heights, or

www.manaraa.com

equally, in terms of height-averaged relations involving mean molecular weight and temperature. The height-averaged relations are useful to describe the physical reasons for the behavior in the C/G ratio with its dependence on the height-averaged mean molecular weight, inverse temperature and vertical gradient of the logarithmic mean molecular weight. Because temperature in the upper thermosphere is essentially exospheric, the temperature scale height term can be neglected for our application. The following section provides a description of the C/G ratio observations and section 2.4 provides an analysis of the terms in Equation 2.2 to explain the observations using the NRLMSISE-00 model.

2.3 Satellite observed C/G mass density ratio in 2007 and 2008

The natural logarithm of the C/G mass density ratio normalized by the altitude difference between satellites (left hand side of Eq 2.2), which equates to the height-averaged reciprocal in density scale height, $<1/H_\rho>$, will be called the C/G ratio. The C/G ratio is displayed for two, month-long, observing periods of February 2007 and December 2008 in figures 2.1 and 2.2, respectively. Figure 2.1 illustrates the C/G ratio near 10 LT for the month of February 2007 when the solar EUV flux proxy, $F_{10.7}$, was near 80 solar flux units (sfu). The CHAMP data were normalized to a mean altitude of 359 km (whose altitude variation over the orbit was ±10 km) and the GRACE data were normalized to a mean altitude of 479 km (whose altitude variation over the orbit was ±15 km). Figure 2.1b illustrates the $F_{10.7}$ and K_p indices during the month. The primary geomagnetic activity during the month is due to corotating interaction regions / high speed streams.

www.manaraa.com

During this late solstice month of 2007, the C/G ratio increases from the summer hemisphere towards the winter hemisphere with maxima residing between 20-40°N. Thus, the summer hemisphere displays an overall smaller C/G ratio than in the winter hemisphere, consistent with higher temperatures in summer than winter as dictated by the inverse dependence on temperature in the first term of Equation 2.2. The overall increasein the C/G ratio as the month progressed is connected with the decrease in the solar EUV flux, as indicated by the decreasing $F_{10.7}$ index, and, again, indicates a temperature effect. However, for latitudes north of 45°, the C/G ratio tends to decrease in a region that is expected to increase due to colder temperatures. This behavior suggests that composition is contributing to the C/G ratio where a decrease in mean molecular weight over this region is contributing to the decrease in the C/G ratio, see middle term of right hand size of Equation 2.2.

Figure 2.1c illustrates the C/G ratio behavior amongst hemispheres by plotting time series of C/G ratios for two polar region latitudes of 59°N and 58°S for the month of February 2007. The winter and summer high latitudes correlate very well in time and decrease at times when the geomagnetic activity increases. The C/G ratio in the winter hemisphere consistently exceeds the summer hemisphere. Fluctuations in C/G ratio values for both hemispheres occurring more frequently than geomagnetic activity changes are attributed to longitudinal effects due to the

www.manaraa.com

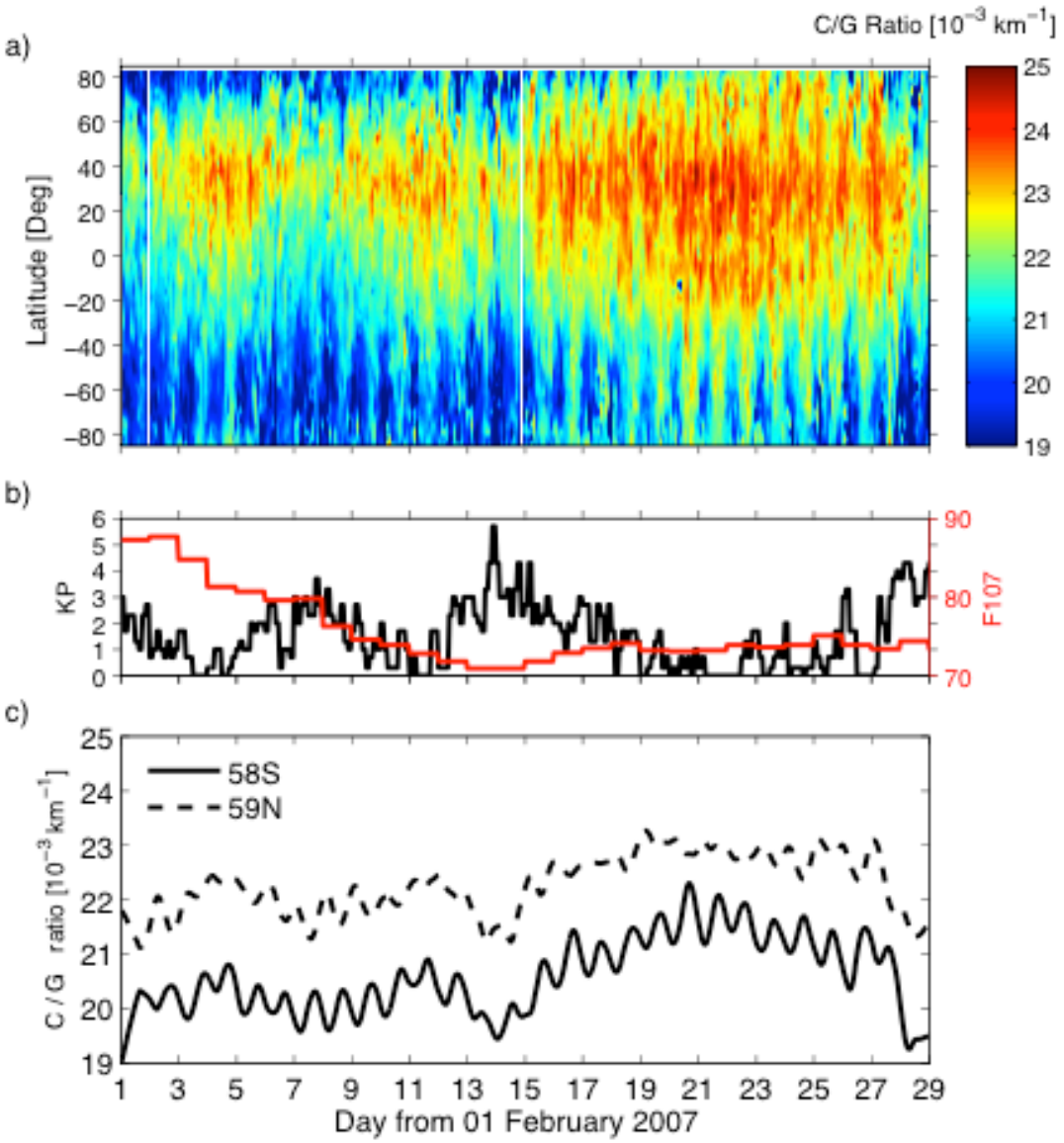

Figure 2.1. a) Latitude-time plot of the natural logarithm of the GRACE and CHAMP mass density ratio normalized by the satellite altitude difference for a 29 day period at 10 SLT starting from February 1, 2007, b) K_p and $F_{10.7}$ indices and c) time series of the data in (a) at the specific latitudes of 58°S and 59°N.

www.manaraa.com

offset between the Earth's geomagnetic pole and the geographic pole [W. Wang, presonal communication, 2012, *Xu et al.* 2013].

Figure 2.2 provides the C/G ratio for the GRACE and CHAMP coplanar period of December 2008 where the solar flux neared its extreme minimum for this solar cycle with a reported $F_{10.7}$ value of about 67 sfu. The CHAMP data were normalized to a mean altitude of 332 km and the GRACE data were normalized to a mean altitude of 476 km. Only the 08 local time results are displayed in Figure 2.2. The C/G ratio response during this solstice month is quite different than in the 2007 solstice period. First, the C/G ratio at subpolar latitudes and in the summer polar region is higher, on average, than the C/G ratio observed in February 2007. This can be explained by the much lower $F_{10.7}$ index in December 2008 as illustrated in Figure 2.2b and consequently colder temperatures. Second, the C/G ratio in the winter polar region is now lower than in the summer during the quiet periods of geomagnetic activity, even though winter temperatures are expected to be less than summer. Third, decreases in the summer polar region C/G ratio expand equatorward with geomagnetic activity while the winter hemisphere C/G ratio displays invariant latitudinal expansion throughout the month. Finally, the variation in C/G ratio during geomagnetic activity is anticorrelated between hemispheres with the winter hemisphere indicating an increase in C/G ratio during active times while in the summer hemisphere the C/G ratio decreased. This can be observed more clearly in Figure 2.2c where the time series of C/G ratio values for 59°N and 58°S are plotted for the month of December 2008. The summer

www.manaraa.com

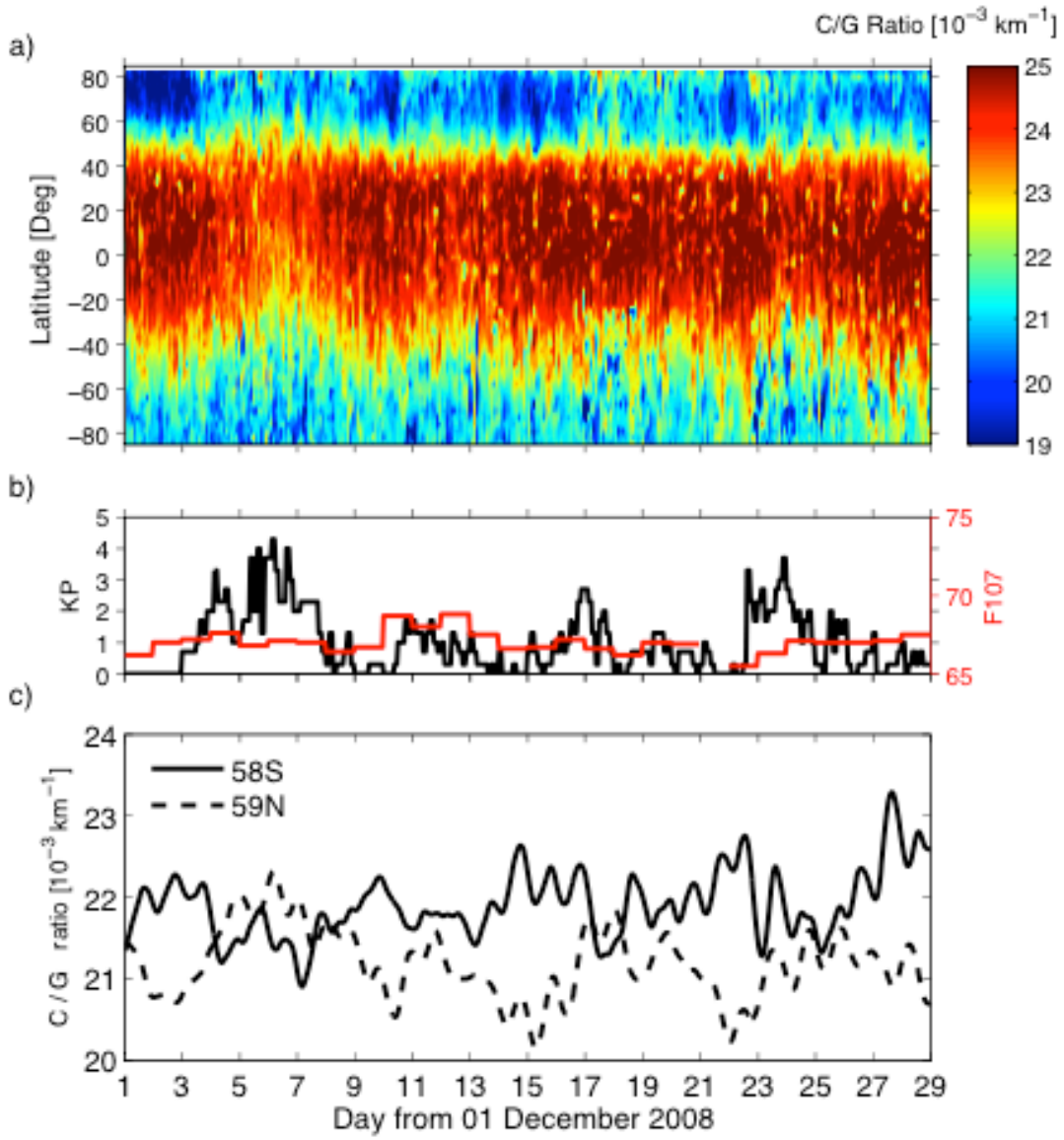

Figure 2.2. a) Latitude-time plot of the natural logarithm of the GRACE and CHAMP mass density ratio normalized by the satellite altitude difference for a 30 day period at 9 SLT starting from December 1, 2008, b) K_p and $F_{10.7}$ indices and c) time series of the data in (a) at the specific latitudes of 58°S and 59°N.

hemisphere C/G ratio values now regularly exceed the wintertime values. Also, the C/G ratio values in the winter and summer now regularly exceed the wintertime values. Also, the C/G ratio values in the winter and summer polar regions show a clear anticorrelation with geomagnetic

www.manaraa.com

activity, in stark contrast to February 2007, even though the geomagnetic activity levels for the two time periods are comparable.

The observed behavior in thermosphere mass density ratio in December 2008 can be explained by composition effects where latitude and geomagnetic variations in the O/He transition altitude significantly impact the changes in scale height and the mass density response. More specifically, the behavior in the C/G ratio is indicative of a significant presence of He in the winter hemisphere for this December 2008 period, as was inferred by *Bruinsma and Forbes* [2010]. The dominant presence of He in the winter hemisphere acts to reduce the mean molecular weight of the thermosphere gas between CHAMP and GRACE altitudes, particularly during quiet geomagnetic times. Thus, although the temperature from the summer to winter poles is expected to decrease, the C/G mass density ratio remains low in the winter hemisphere because of effects related to the behavior in the mean molecular weight.

The December 2008 C/G ratio behavior with geomagnetic activity does not mean that the actual mass density at GRACE altitudes during active times decreases from quiet times – it indeed increases, but that increase is tempered by the mean molecular weight change at GRACE altitudes. As a result, the mass density increases more significantly during active times at CHAMP altitudes than at GRACE altitudes leading to a C/G ratio enhancement in the northern winter hemisphere. This same effect of surpressing mass density change during geomagnetic activity due to composition changes can occur at lower altitudes near the N_2/O transition height [e.g., *Lei et al.*, 2010; *Qian et al.*, 2010], but is not as extreme an effect because of the smaller molecular weight difference and smaller vertical gradient in the natural logarithm of mean

www.manaraa.com

molecular weight. There does not appear to be much evidence of N_2 effects in the two datasets presented, probably due to the contracted thermosphere making this transition region reside below the altitude of CHAMP and because geomagnetic activity was rather weak during these times. Meanwhile, the summer hemisphere response to geomagnetic activity behaves in a manner driven primarily by temperature effects on pressure scale height in an O-dominated thermosphere, similar in behavior to the February 2007 and December 2008 summer observations, where the C/G mass density ratio decreases with geomagnetic activity and expands equatorward.

2.4 MSISE00 Simulations of C/G ratio and Scale Heights in 2007 and 2008

The data presented in section 2.3, by themselves, cannot separate temperature effects from composition effects on mass density, and only indicate when one dominates over the other. Next, we employ the NRLMSISE-00 model to assist in evaluating the temperature and composition effects on mass density response to geomagnetic activity under the preconditioned state of this extreme solar minimum. The MSIS model is run for the conditions of February 2007 and December 2008 and terms from Equation 2.2 are evaluated to assist with the interpretation of the observed behavior in C/G ratio.

The MSIS estimate of the C/G ratio for the February 2007 period is displayed in Figure 2.3 using the geomagnetic and $F_{10.7}$ indices presented in Figure 2.1b and same scale as Figure 2.1a. Comparing with C/G ratio observations in Figure 2.1a, the MSIS estimate shows similar large-scale structure and magnitudes. However, the MSIS C/G ratio in the winter hemisphere

www.manaraa.com

tends to increase continuously to the winter pole where the observations indicate a midlatitude peak and then a relative decrease in C/G ratio

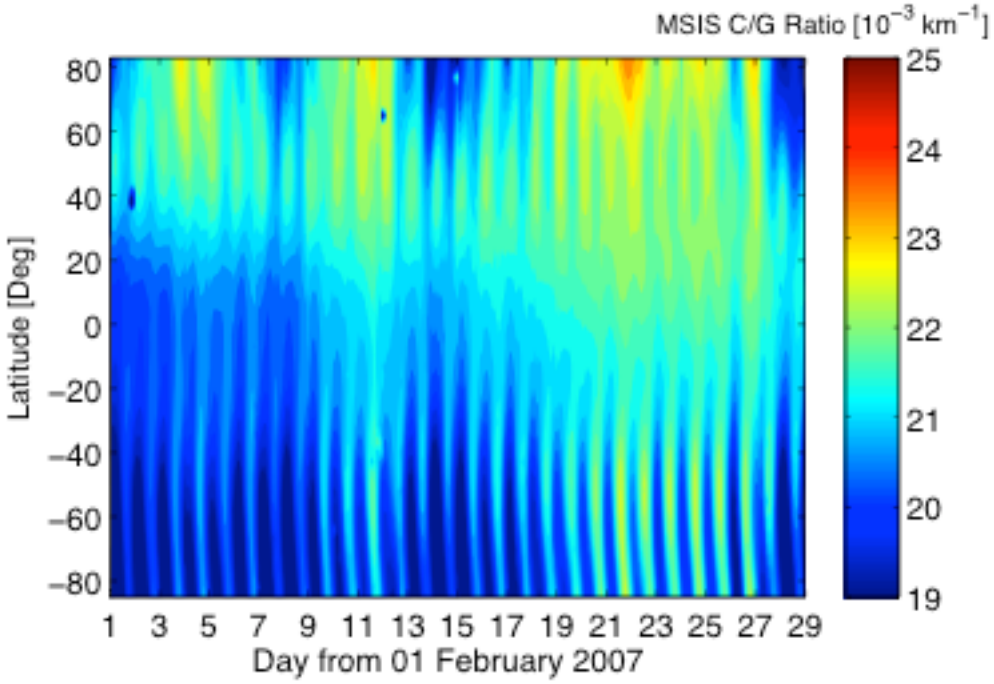

Figure 2.3. Latitude-time plot of the natural logarithm of the MSIS mass density ratio normalized by the altitude difference for CHAMP and GRACE satellites over a 29 day period at 10 SLT starting from February 1, 2007.

towards the winter pole. Based on the discussions in section 2.2, this suggests a composition effect that is not being reproduced by MSIS.

The time series of MSIS C/G ratios for 59°N and 58°S for the month of February 2007 is given in Figure 2.4. In this case, the relative structure, with the winter C/G ratio greater than the summer C/G ratio, and response to geomagnetic activity, with the winter and summer C/G ratio decreasing with activity, is very similar to the observations. MSIS also reproduces the short-term fluctuations assumed to be due to longitudinal effects for the fixed local time measurements.

www.manaraa.com

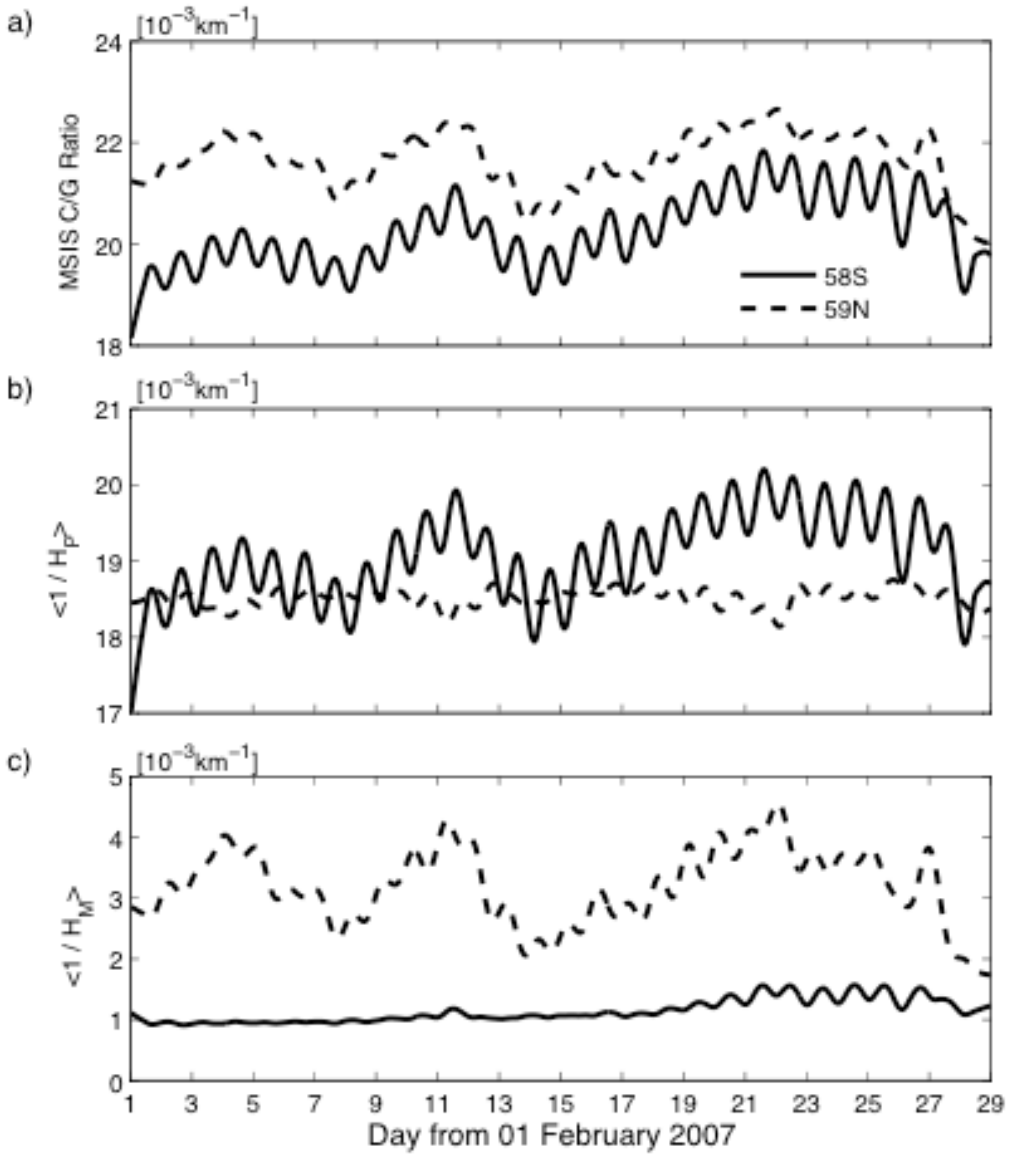

Figure 2.4. a) Time series of the MSIS February 2007 estimates from Figure 2.3, b) Time series of the MSIS reciprocal pressure scale height, and c) Time series of the MSIS reciprocal molecular weight scale height at the specific latitudes of 58°S and 59°N.

The reasonable representation of the observations by the MSIS model for February 2007 allows for further investigation into the cause of the variations in the observed C/G ratio with geomagnetic activity by using the relation given in Equation 2.2. Figure 2.4b,c presents the MSIS estimates of $<1/H_p>$ and $<1/H_M>$ whose addition produces the MSIS C/G ratio.

www.manaraa.com

Comparing Figure 2.4b with Figure 2.4c, the height-averaged reciprocal in the pressure scale height is the dominant term and comparable in magnitude between the winter and summer hemisphere. The height-averaged reciprocal in the molecular weight scale height contribution is significantly different between hemispheres with the winter hemisphere having about a 15% contribution while in the summer hemisphere its contribution is only about 5%. In fact, it is the height-averaged reciprocal of the molecular weight scale height in the winter hemisphere that is responsible for the greater C/G ratio in winter than in summer, and also produces the geomagnetic activity variability observed in the winter hemisphere.

Thus, although the observations indicate the C/G ratio to behave similarly between the summer and winter hemispheres, the reason for their correlation is not caused by the same effect. In the summer hemisphere, the pressure scale height is dominant and its variations are largely caused by temperature changes associated with geomagnetic activity. In the winter hemisphere, the temperature is much colder which lowers the O/He transition altitude to cause the mean molecular weight to decrease and offset the temperature decrease on the pressure scale height – making the two hemispheres have similar reciprocal pressure scale heights during quiet times (Figure 2.4b). However, the lowering of the O/He transition altitude by the colder temperatures also increases the reciprocal of the molecular weight scale height (Figure 2.4c) raising the observed C/G ratio in winter and making it larger than in summer. The reciprocal of the pressure scale height in winter also displays an invariance to geomagnetic activity with the mean molecular weight change offsetting any temperature change. However, the reciprocal of the molecular weight scale height decreases with geomagnetic activity as the O/He transition altitude

www.manaraa.com

rises. Thus, the vertical gradient in logarithmic molecular weight becomes the controlling factor in the February 2007 winter hemisphere response in the C/G ratio to geomagnetic activity.

The MSIS estimate of the C/G ratio for the December 2008 period is displayed in Figure 2.5 using the geomagnetic and $F_{10.7}$ indices presented in Figure 2.2b and the same scale as in Figure 2.2a. By comparison with the observations, the MSIS C/G ratio is underestimated at middle latitudes and not consistent with the observed summer / winter behavior. This is illustrated in Figure 2.6a where the MSIS C/G ratio time series in the winter hemisphere is, on average, greater than the summer hemisphere and shows either a correlation with the summer hemisphere during geomagnetic activity or an invariance to geomagnetic activity. The satellite observations of the C/G ratio (Figure 2.2c) between winter and summer were clearly anticorrelated with geomagnetic activity and the winter hemisphere values were, on average, lower than the summer hemisphere values. Using Equation 2.2 and the same analysis approach as in February 2007, the height-averaged reciprocal pressure scale height and reciprocal molecular weight scale height are displayed in Figure 2.6b,c. The lower $F_{10.7}$ values in December 2008 produce a stronger latitudinal gradient in temperature and molecular weight, causing the reciprocal scale height values to be signficantly different between the two hemispheres, as compared to February 2007. Also, in the winter hemisphere, the height-averaged reciprocal molecular weight scale height contributes more to the C/G ratio during quiet times (about 25%) and responds oppositely to the pressure scale height during geomagnetic activity. This opposing behavior with increasing geomagnetic activity is due to the rise in global temperatures causing the vertical gradient in logarithmic molecular weight to decrease while the mean molecular weight contributing to the

www.manaraa.com

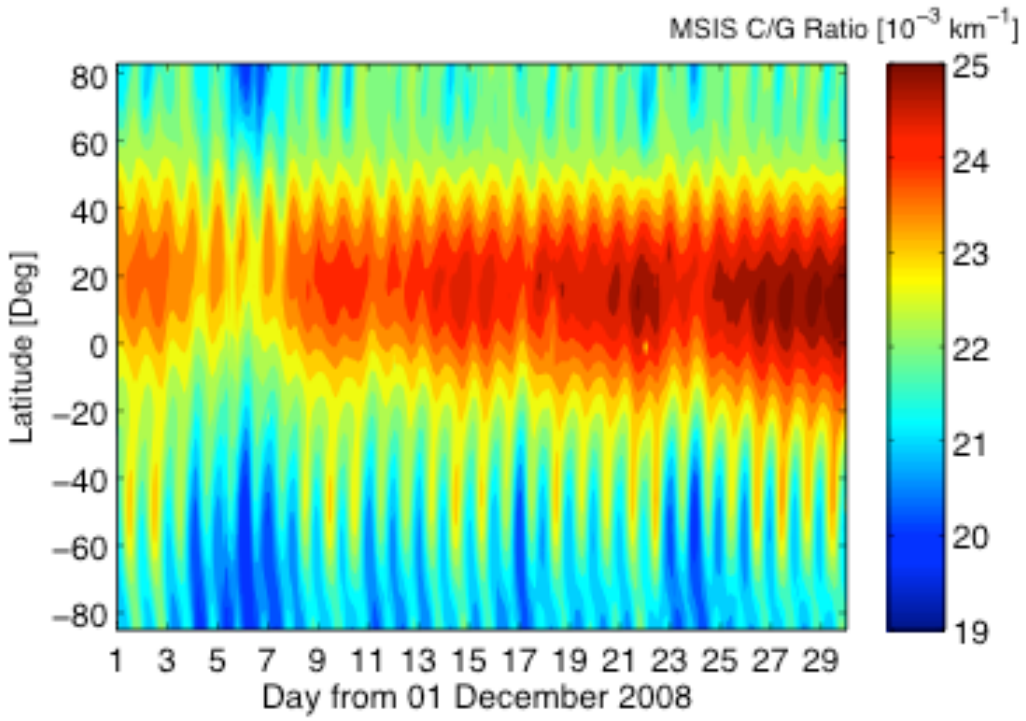

Figure 2.5. Latitude-time plot of the natural logarithm of the MSIS mass density ratio normalized by the altitude difference for CHAMP and GRACE satellites over a 30 day period at 9 SLT starting from December 1, 2008.

www.manaraa.com

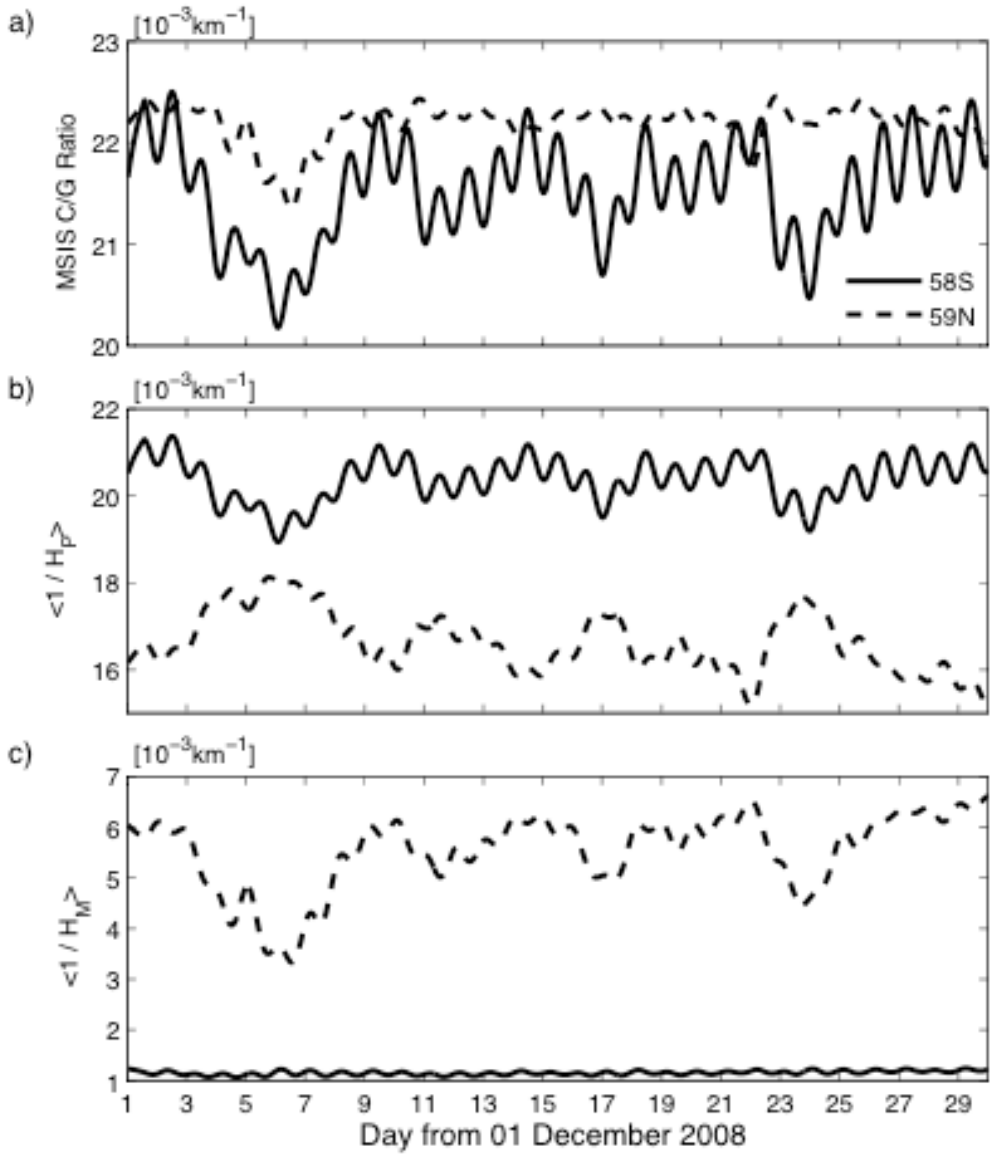

Figure 2.6. a) Time series of the MSIS December 2008 estimates from Figure 2.5, b) Time series of the MSIS reciprocal pressure scale height, and c) Time series of the MSIS reciprocal molecular weight scale height at the specific latitudes of 58°S and 59°N.

pressure scale height will increase. However, for the MSIS C/G ratio it seems the gradient in molecular weight is too significant causing the C/G ratio to decrease or become invariant to geomagnetic activity. Thus, the MSIS composition is not properly describing the observations – a conclusion similar to MSIS estimates in 2007 but with a more significant effect and consistent

www.manaraa.com

with observations reported by *Bruinsma and Forbes* [2010]. The MSIS results shown in Figure 2.6 do illustrate how a greater increase in He can further complicate the C/G ratio response.

The MSIS model requires an adjustment to better represent the December 2008 GRACE and CHAMP observations and the first task is to evaluate the $F_{10.7}$ and A_p indices that are used as input to the model. The two-day, quiet-time period of December 9-10, 2008 is chosen as a typical baseline of mass density data where high concentrations of He in the winter hemisphere were inferred from Figure 2.2. This time period is when the satellites are near the 8.4 LT plane with about 0.1 LT difference between GRACE and CHAMP orbits. This local time plane is close to the expected daily maximum in He concentration based on the results of *Cageao and Kerr* [1984]. The GRACE and CHAMP mass densities at subpolar latitudes (between 40 °N and 40 °S) are used to provide a baseline which MSIS mass density values should approach. We used an iterative scheme of adjusting $F_{10.7}$ input values to MSIS while updating the MSIS normalization factor for the CHAMP and GRACE fixed altitudes of 332 km and 476 km, respectively, until the satellite mass density and MSIS mass density values were within 5% of eachother.

Figure 2.7 displays the two-day averaged CHAMP and GRACE mass density estimates and two-day averaged MSIS mass density estimates with latitude at the two normalization altitudes. The $F_{10.7}$ index required a value of 53 sfu, a reduction of 14 sfu from the original value, for MSIS to best represent the observed densities at CHAMP and GRACE within 5% of their mid-to-low latitude values. This downward adjustment is in agreement with the $M_{10.7}$ index using the Mg II core-to-wing ratio suggested by *Solomon et al.* [2011] and the $F_{10.7}$ overestimate of EUV flux implied by ionosphere f_oF_2 response [*Chen et al.*, 2011]. The A_p values were also

www.manaraa.com

adjusted from between 2 to 4 to account for uncertainty in the very low geomagnetic activity over the two days. Using the more recent accelerometer processing of *Sutton* [2009], no apparent scaling bias between CHAMP and GRACE was necessary. Note that the CHAMP and GRACE normalization process described in section 2.3, and used in Figure 2.2, was based on these revised MSIS densities to minimize the error in normalization. The required downward adjustement of $F_{10.7}$ as input to MSIS explains the issue raised by *Bruinsma and Forbes* [2010] that the MSIS model was overestimating its representation of the mass density observations and confirms our results presented in the previous figures.

Figure 2.7 illustrates very good agreement of MSIS with CHAMP mass densities for all latitudes, except for a 10% deviation in the summer near the pole. At GRACE altitudes, MSIS results indicate excellent agreement in the southern summer hemisphere but a large deviation from the GRACE quiet-time mass densities in the winter northern hemisphere. The MSIS mass density shows an inflection at low northern latitudes indicating the presence of He but significantly underestimates the mass density in the winter mid-to-high latitudes. Presuming the GRACE mass density values are accurate, a 30% increase in He concentration for latitudes above 50°N is required to bring the MSIS values into better agreement, as shown by the dashed black line in figure 2.7. It has been noted in early studies of the wintertime helium bulge that low solar flux leads to a larger latitudinal gradient in He [e.g., *Reber and Hays*, 1973]. The underestimation by MSIS may reflect the extreme conditions of this recent solar minimum and limitations of the model. A separate MSIS mass density curve shown by the black dash-dot line in figure 2.7 excludes He in the mass density estimate. Clearly He is the main contributing

www.manaraa.com

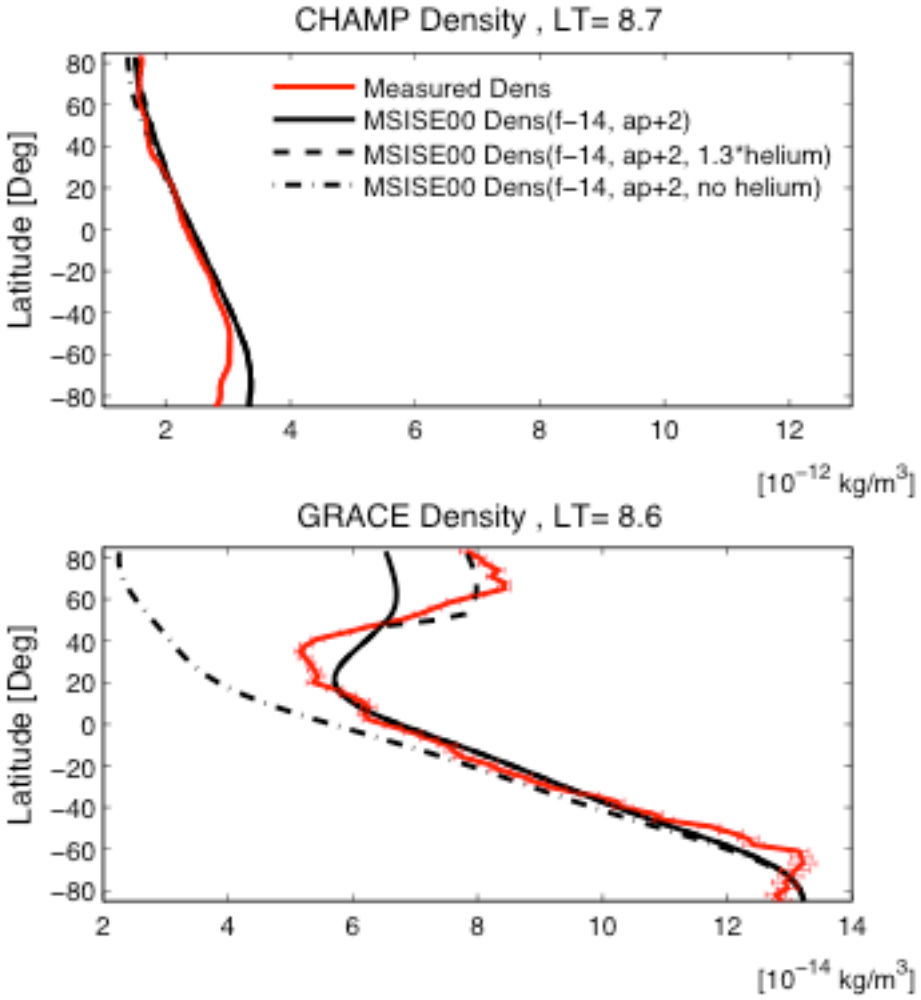

Figure 2.7. CHAMP and GRACE mass density estimates (red line) versus geographic latitude averaged over December 9-10, 2008. Adjusted MSIS mass density estimates after reducing $F_{10.7}$ index by 14 sfu and increasing ap by 2 (black line), further adjustment by increasing helium by 30% above 50° N (black dashed line), and excluding helium in the estimate of MSIS mass density after $F_{10.7}$ and ap adjustment (black dash-dot line). Error bars on GRACE density represent the statistical error of the mean after two-day averaging.

factor to the mass density throughout the winter hemisphere – a He/O mass density ratio of 6:1 is found near 75°N indicating the thermosphere near 476 km altitude is primarily He for this quiet-time period in December 2008.

www.manaraa.com

However, the satellite mass density estimate is not void of uncertainty and could contribute to the difference between MSIS and the observed C/G ratio. The accuracy in estimating mass density from satellite accelerometer data is directly dependent on the accuracy in determining the satellite drag coefficient and cross-sectional area. Gas-surface interactions lead to drag and lift force coefficients that require in-depth modeling and assessment. *Sutton* [2009] has revisited gas-surface interaction assumptions for the CHAMP and GRACE satellites and, using propagation of errors procedure outlined by *Sutton et al.* [2007], estimates for CHAMP and GRACE mass density errors are less than 10% for this data period. Although neutral wind effects are rather uncertain, the dawn-dusk local time track of the orbit in December 2008 would experience little along-track winds.

An additional factor to consider under these unique conditions is the influence of He on the satellite drag coefficient. The presence of He instead of O at the same temperature would act to increase the drag coefficient and subsequently decrease the estimated mass density. However, applying a thorough analysis that accounts for both composition and temperature using the nonadjusted and adjusted $F_{10.7}$ values for input to the MSIS model atmosphere, the effect of the adjusted MSIS atmosphere, i.e. more He but colder temperatures, on the drag coefficient is only a few percent (see appendix material) from the estimate using the nonadjusted MSIS atmosphere for the winter polar latitudes. Thus, assuming no changes in the nature of gas-surface interactions (accommodation or scattering properties) [*Pilinski,* 2010,2011], the drag coefficient is not expected to compensate much for the 30% increase in He required to match MSIS with the winter hemisphere observations - if the drag coefficient is based on an MSIS atmosphere using

www.manaraa.com

the original $F_{10.7}$ value. More challenging regions of uncertainty lie at latitudes where the O/He ratio is closer to one or two (see appendix material).

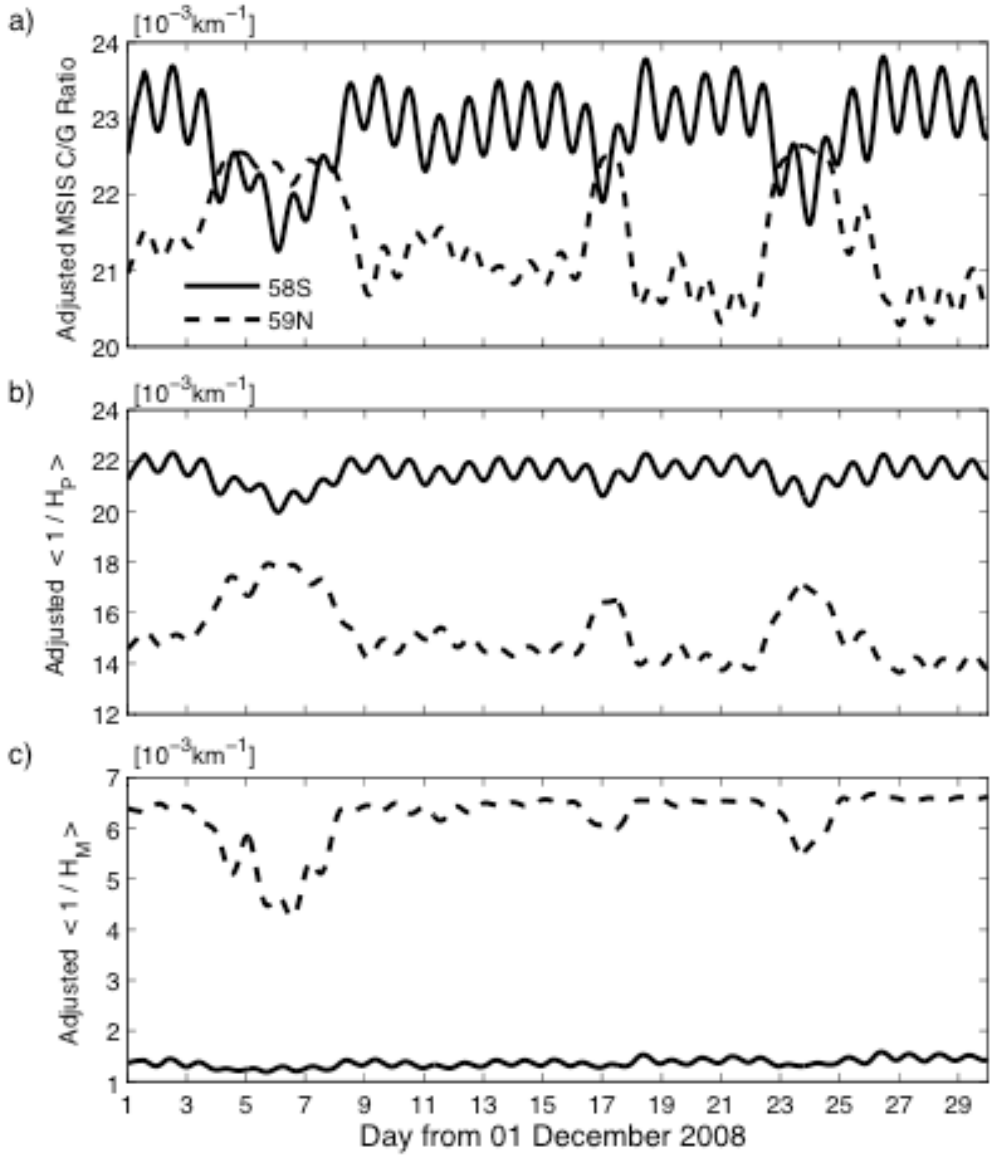

Figure 2.8. a) Time series of the adjusted MSIS December 2008 estimates from Figure 6, b) Time series of the adjusted MSIS reciprocal pressure scale height, and c) Time series of the adjusted MSIS reciprocal molecular weight scale height at the specific latitudes of 58°S and 59°N.

www.manaraa.com

Figure 2.8 is a reproduction of Figure 6 using the adjusted MSIS model described above for the entire month of December 2008. The additional 30% increase in He above 50°N is included in the MSIS output for all times when the A_p index is less than 5, i.e. very quiet conditions. The MSIS C/G ratio in Figure 2.8a is now smaller in winter than summer and its response to geomagnetic activity is anticorrelated between winter and summer in a manner similar to the December 2008 observations shown in Figure 2.2c. The MSIS adjustment caused the relative change in the height-averaged reciprocal pressure scale height from quiet to active conditions to increase in the winter hemisphere while the relative change in the height-averaged reciprocal molecular weight scale height decreased. The increase in the reciprocal pressure scale height can be explained by the mean molecular weight increasing more significantly than temperature in the winter hemisphere during increases in geomagnetoic activity. The decrease in reciprocal molecular weight scale height can be explained by the greater dominance in He concentration between the CHAMP and GRACE satellites for this time period causing the vertical gradient in logarithmic molecular weight change to be less. Consequently the December 2008 anticorrelation in C/G ratio with geomagnetic activity is due primarily to wintertime increases in the mean molecular weight being greater than temperature increases leading to an overall increase in the reciprocal pressure scale height. The relative increase in reciprocal pressure scale height is greater than the relative decrease in the reciprocal molecular weight scale height resulting in an overall increase in the wintertime C/G ratio. This case represents a helium-dominant influence on the C/G mass density ratio response.

www.manaraa.com

2.5 Oxygen / Helium Transition Altitudes

Although the MSIS model does not fully describe the observations, it does provide insight into the role composition plays in producing the observed behavior in the C/G ratio during this preconditioned solar minimum state of the thermosphere. The MSIS winter hemispheres in February 2007, pre-adjusted December 2008, and adjusted December 2008 indicate different responses to geomagnetic activity that depend on the relative concentration of O and He over the CHAMP-GRACE altitude range. In February 2007 and the pre-adjusted December 2008 data, the contribution by the vertical gradient of the logarithmic mean molecular weight was the distinguishing factor in producing the winter hemisphere response to geomagnetic activity. The adjusted December 2008 data were also influenced by the vertical gradient of the logarithmic mean molecular weight but the change in mean molecular weight relative to temperature was more significant in describing the observed behavior in the mass density ratio. Clearly the behavior in the O/He transition altitude needs to be well understood to properly describe the observations.

Figure 2.9 illustrates the altitude where the He and O number density are equal, i.e., the O/He transition height, from the adjusted MSIS model for December 2008. For summer conditions, the transition height lies well above GRACE altitudes resulting in an O-rich thermosphere which makes the reciprocal in molecular weight scale height much smaller than the reciprocal in pressure scale height and does not contribute significantly to the C/G ratio. However, in the quiet-time, winter hemisphere the observations suggest that the reciprocal pressure scale height

www.manaraa.com

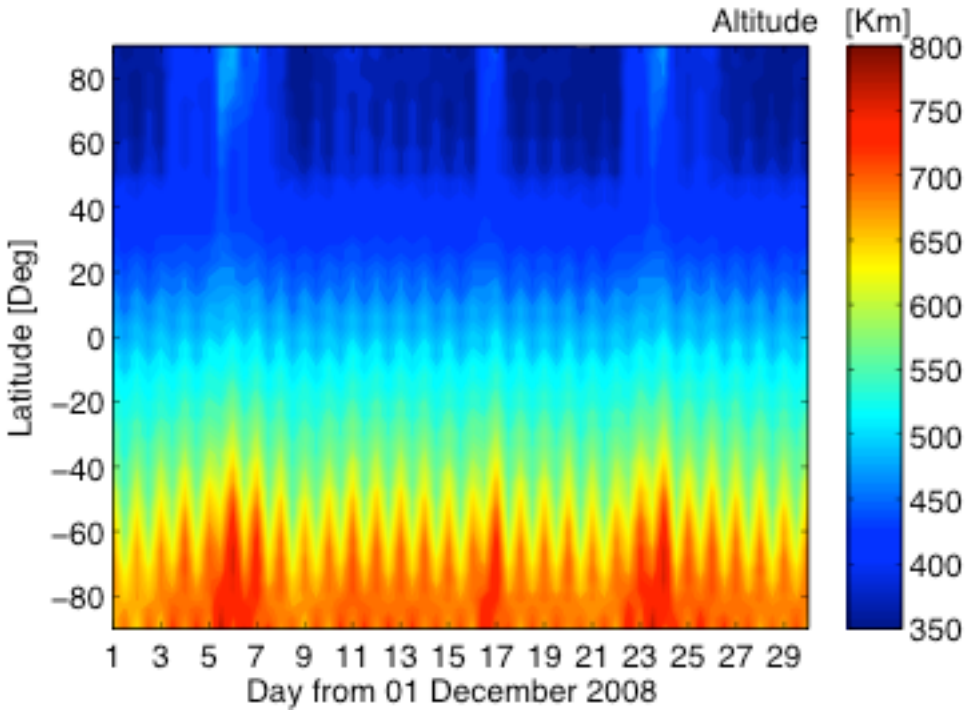

Figure 2.9. The adjusted MSIS oxygen-helium transition altitude for the month of December, 2008.

has decreased under conditions where, if considering only temperature, the reciprocal pressure scale height should increase. This can only be accounted for by having the O/He transition occurring below GRACE altitudes resulting in the mean molecular weight decreasing more than the temperature leading to an overall decrease in the reciprocal pressure scale height.

Figure 2.9 indicates the O/He transition height during quiet times in the polar regions is near 400 km. However, as has been shown, it is also important to consider the vertical gradient of the logarithmic mean molecular weight between the two satellites. A very steep decrease in molecular weight with height will increase the reciprocal molecular weight scale height and offset the decrease in the reciprocal pressure scale height. In fact, the February 2007 and December 2008 C/G ratio observations in the winter hemisphere illustrate the fine balance in the

www.manaraa.com

composition effect decreasing the reciprocal pressure scale height while increasing the reciprocal molecular weight scale height. For the winter hemisphere in February 2007, the O/He transition is at a higher altitude than in December 2008, but still below the GRACE satellite (not shown). This reduced concentration of He led to the reciprocal pressure scale height being invariant to geomagnetic activity, however, the relative change in the molecular weight scale height was significant and caused the C/G ratio in the winter hemisphere to decrease with increasing geomagnetic activity. The winter of December 2008 corresponded with a greater He concentration in the thermosphere and the mean molecular weight dominated the relative change in the reciprocal pressure scale height between quiet and active times. Furthermore, the relative change in molecular weight scale height from quiet to active times was less because of the He dominance with altitude. This resulted in the C/G mass density ratio response to increase with increasing geomagnetic activity. This response will also vary with latitude as the O/He transition height changes from 750 km in the summer polar regions to less than 400 km in the winter polar region. Thus, the relative terms contributing to the C/G mass density response will change with latitude in a manner similar to the different responses observed for varying levels of He present.

During geomagnetically active times, thermosphere temperature increases occur at both CHAMP and GRACE altitudes over all latitudes. Moreover, in the winter hemisphere the O/He transition altitude adjusts from being below GRACE altitudes during quiet times to above GRACE altitudes during active times. This increases the mean molecular weight while decreasing the molecular weight scale height (less impact), such that, the observed C/G mass

www.manaraa.com

density ratio is enhanced during active geomagnetic conditions in the winter hemisphere of December 2008 – opposite to the summer hemisphere response.

The latitudinal structure of the transition from O to He is partly attributed to the thermal structure but is also due to constituent transport processes. The formation of a winter helium bulge, where He concentrations in the winter high latitudes significantly exceed summer concentrations is well known [e.g., *Reber and Hays,* 1973]. Local time phase differences between O and He [e.g., *Hedin et al.,* 1979], geomagnetic effects of O and He redistribution [e.g., *Prölss,* 1981], and differential transport of minor versus major species [e.g., *Mayr et al., 1*978] will further complicate the mass density changes due to composition during solar minimum. *Cageao and Kerr* [1984] have also illustrated significant variations in thermosphere He with local time, season and latitude. These effects will prove very important in evaluating the thermosphere mass density response at GRACE altitudes during this extreme solar minimum owing to the importance of composition changes on mass density response to geomagnetic activity.

2.6 Conclusions

High-resolution mass density observations inferred from accelerometer measurements on the CHAMP and GRACE satellites for coplanar orbital periods in February 2007 and December 2008 provided an opportunity to investigate the mass density response with altitude and latitude to geomagnetic effects under the preconditioned solar minimum state of the thermosphere. The February 2007 data represented typical solar minimum conditions while the December 2008 data

www.manaraa.com

represented extreme solar minimum conditions. The CHAMP-to-GRACE mass density ratio for both solstice periods indicated composition changes are playing a role in describing the mass density ratio structure and response to geomagnetic activity in the winter hemisphere. The description of the C/G mass density ratio in terms of the sum of the reciprocal pressure scale height and the reciprocal molecular weight scale height, or equivalently proportional to the ratio in mean molecular weight to temperature plus the vertical gradient of the logarithmic mean molecular weight, provided insight to the observed behavior.

The February 2007 C/G mass density ratio in the winter hemisphere decreased from mid-latitudes to the pole, counter to expectations based on temperature, indicating He is present between the CHAMP and GRACE altitudes. Furthermore, the February 2007 C/G mass density ratio in the winter polar regions decreased with increasing geomagnetic activity in a manner similar to the summer hemisphere. Yet, this similarity in response between hemispheres is not caused by the same process, as elucidated by employing the MSIS model and expanding the mass density ratio into its contributing terms. The summer hemisphere decrease in C/G ratio with increasing geomagnetic activity is primarily due to the associated increase in temperature leading to a decrease in the reciprocal pressure scale height. Thus, the mass density at GRACE altitudes is increasing more than at CHAMP altitudes due primarily to pressure scale height changes. The winter hemisphere in February 2007 also displays a decrease in C/G ratio with increasing geomagnetic activity but further investigation indicates that this is caused by a decrease in the reciprocal molecular weight scale height (or equivalently a decrease in the vertical gradient of the logarithmic mean molecular weight). Effectively the reciprocal in the pressure scale height in

www.manaraa.com

the winter hemisphere was invariant to geomagnetic activity, as the expected change in temperature was offset by an equivalent change in mean molecular weight. However, the vertical gradient in logarithmic molecular weight between CHAMP and GRACE decreases due to the temperature increase and causes the C/G ratio to decrease with increasing geomagnetic activity.

The December 2008 period displayed even more diverse mass density ratio structure and response to geomagnetic activity in the winter hemisphere. Differences from February 2007 observations included the C/G mass density ratio in the winter hemisphere was, on average, 1) less than the summer hemisphere, 2) anticorrelated to the summer hemisphere C/G mass density ratio response to geomagnetic activity - winter hemisphere C/G ratio increased with an increase in geomagnetic activity while in the summer hemisphere C/G ratio decreased, and 3) displayed little latitudinal expansion during enhanced geomagnetic activity than the summer hemisphere. Essentially this diverse behavior can be explained by a much more significant amount of He present between CHAMP and GRACE altitudes.

The MSIS model required significant adjustment to better represent the data and to help explain the observed behavior. MSIS estimates of mass density in December 2008 required a reduction in $F_{10.7}$ in order to properly represent the observed subpolar mass density latitude structure observed by CHAMP and GRACE. However, the model seemed to underestimate the total amount of He in the winter hemisphere and a 30% increase in He above 50°N was required to best match the observations. Once adjusted, the MSIS model supported the dominant presence of He in the winter hemisphere between CHAMP and GRACE. This additional requirement of

www.manaraa.com

He may indicate that He transport processes forming the winter helium bulge are more significant under these extreme conditions and that MSIS cannot adequately account for this process.

The explanation for the diverse behavior in the winter hemisphere mass density ratio for December 2008 again involves the offsetting effects of composition and temperature. The lower C/G ratio in the winter than summer hemisphere is due to a lower value for the height-averaged reciprocal in pressure scale height and equates to the low mean molecular weight of the winter hemisphere. The increase in C/G ratio with increasing geomagnetic activity is due to the height-averaged reciprocal in pressure scale height increasing more significantly than the height-averaged reciprocal in the molecular weight scale height decreasing. The height-averaged reciprocal in pressure scale height increases with geomagnetic activity because the mean molecular weight increases more significantly than the temperature. The lack of latitudinal expansion in the winter hemisphere during geomagnetic activity is due to a dynamic balance between the reciprocal in pressure scale height and the reciprocal in the molecular weight scale height.

Thus, the structure and response of the C/G mass density ratio during this recent solar minimum is dependent on the temperature and composition distribution for the latitude, altitude range, and season of observation. The diverse behavior in the wintertime thermosphere mass density between February 2007 and December 2008 is an indication of the temperature and composition interplay and will be an important attribute throughout this recent solar minimum period in the interpretation of mass density change and satellite drag prediction. The February

www.manaraa.com

2007 period represented nominal solar minimum conditions and displayed He-influenced affects on the C/G mass density ratio in the winter hemisphere, while the December 2008 period represented extreme solar minimum conditions and displayed He-dominant affects on the C/G mass density ratio in the winter hemisphere. The dynamics of the O/He transition height will prove very important in evaluating the latitudinal thermosphere mass density response at GRACE altitudes as it resides above the satellite in the summer polar regions (~750 km in December 2008) and below the satellite in the winter polar regions (~400 km in December 2008). The dynamical exchange between light and heavy constituents and strong thermal gradients will make the interpretation of mass density response with altitude and latitude during this solar minimum more complex as composition effects combine with temperature effects to produce the observed response.

www.manaraa.com

Chapter 3 Altitude Variations of the Thermosphere Mass Density Response

Chapter 2 demonstrated complex responses in thermosphere mass density to geomagnetic activity at the altitude of the GRACE satellite (~500 km) during the recent solar minimum, and associated this behavior to the dynamic action of the O to He gas transition in this altitude range. This chapter develops a more comprehensive understanding of the causes for altitude variations in thermosphere mass density when responding to geomagnetic activity.

3.1 Background Introduction

Upper atmosphere disturbances in mass density during geomagnetic storms have been well studied in terms of latitude variation [e.g., *Rothwell and McIIwain* 1960; *Jacchia and Slowey* 1968; *Devries et al.,* 1967; *Jacobs* 1967, and references therein], local time variation *[Hedin and Carignan* 1985*; Rentz and Lühr* 2008*; müller et al.,* 2009*]*, longitude variations *[Prölss* 1985*],* seasonal variations *[Allen and Kroehl* 1975*; Prölss and von Zahn* 1977*],* solar rotation effect *[Lei et al.,* 2008*; Thayer et al.,* 2008*; Matsuo and Forbes* 2010*; Crowley et al.,* 2008], and so on; however, the altitude variation of the thermosphere mass density response to geomagnetic storms is far less understood. *Emmert et al.* [2010], using globally averaged daily mass density data from the past three solar cycles, applied their empirical Global Average Mass Density Model (GAMDM) to calculate the density anomaly as a function of height between 200 and 600 km

www.manaraa.com

during the solar minimum period 2008.3 to 2009.3. They found that the mass density anomaly is maximum at 500 km near the transition region of O to He.

As described in Chapter 1, the altitude distribution of the major gases in the quiet-time thermosphere is to first order described by diffusive equilibrium with species separating out with altitude by their respective molecular weights. Consequently, the neutral atmosphere from 150 km to 800 km progresses from a molecular-nitrogen (N_2) dominant region, molecular nitrogen to oxygen (N_2/O) transition region, oxygen-dominant (O) region, oxygen to helium (O/He) transition region and a helium-dominant (He) region. The altitude where these transitions occur is temperature dependent through their individual scale heights and therefore varies with latitude, longitude and universal time.

This extreme solar minimum has resulted in much smaller scale heights for each constituent and more rapid transitions with altitude between composition regions. This contraction of the thermosphere will lead to much steeper altitude gradients in the constituents and more nonlinear behavior in the mean molecular weight which will impact the gas response to geomagnetic activity. As will be shown, it will be very important to represent the altitude distribution of the quiet-time thermosphere gas adequately in order to study its mass density response to geomagnetic activity. As described in Chapter 2, the mass density scale height is determined by the sum of the mean molecular weight to temperature ratio and the vertical gradient of the logarithmic mean molecular weight. Thus, the manner in which composition transitions with height and varies with geomagnetic activity will impact the mass density response.

The study in Chapter 2 on the O/He transition region is based on two particular altitudes,

www.manaraa.com

around 332 km for CHAMP and 476 km for GRACE during solar minimum, The studies by *Lei et al.* [2010] and *Qian et al.* [2010] were concerned with the O/N_2 composition effect on the mass density response at a single altitude near 400 km during the declining phase of the solar cycle in 2004, 2005 respectively. This chapter is intended to give a more comprehensive understanding of the altitude variation of the mass density response to a geomagnetic storm. As will be shown, the level of response of the thermosphere mass density will be altitude dependent with significant contributions provided by the relative dynamics of the thermosphere composition.

The mass density observations from accelerometer measurements onboard the CHAMP and GRACE satellites are employed in this study during the time period when these two satellites are in coplanar orbits, Dec 01-10, 2008. Helium and oxygen concentrations at the GRACE altitude are estimated from CHAMP and GRACE mass density measurements in section 3.2 and in appendix B. Section 3.3 illustrates the impact of the thermosphere composition variation on the mass density response to a geomagnetic storm. Section 3.4 evaluates the storm-time mass density perturbation using the MSIS model and assesses the parameters that affect the mass density perturbation. The coplanar orbits enable investigation of the mass density scale height variation with storm activity. The density scale height relationship to the mass density perturbation at a fixed altitude is provided, and the contributing factors that lead to density scale height changes are evaluated. A particular focus is on the O/He transition region which is found to have a significant influence on the mass density scale height and, therefore, on the response of mass density at GRACE altitudes. Section 3.5 provides a summary of the

www.manaraa.com

findings in this chapter.

3.2 Mass Density Observation from CHAMP and GRACE

The thermosphere mass density observations are obtained from accelerometer measurements onboard CHAMP and GRACE. This is essentially the same analysis as performed in Chapter 2 for this same time period.

The top panel in Figure 3.1 shows the CHAMP satellite mass density estimates normalized to an altitude of 350 km and the second panel displays the GRACE satellite mass density observations normalized to an altitude of 500 km for the time series from 01-10 December 2008. The bottom panel in figure 3.1 shows the solar EUV flux proxy, $F_{10.7}$, and geomagnetic acitivity indices K_p. The primary source of geomagnetic activity in our study period is due to a corotating interaction region / high speed stream (CIR/HSS) event. The $F_{10.7}$ index, ranging from 66 to 68 solar flux units (sfu), could be treated as almost invariant during this time period. The K_p index shows that the geomagnetic activity was exceptionally quiet before the CIR/HSS storm onset with a K_p~0. A CIR/HSS event perturbs the mass density during 4-7 December 2008. K_p values varied from 2-4 during the CIR/HSS storm, which characterize this event as moderate geomagnetic activity.

The mass density plots in Figure 3.1a and Figure 3.1b illustrate during the quiet periods the expectation of the largest mass density occurring in the summer hemisphere due to the higher temperature and subsequently larger scale height at both CHAMP and GRACE satellite altitudes. The mass density also displays the general response of increasing at a fixed altitude during

www.manaraa.com

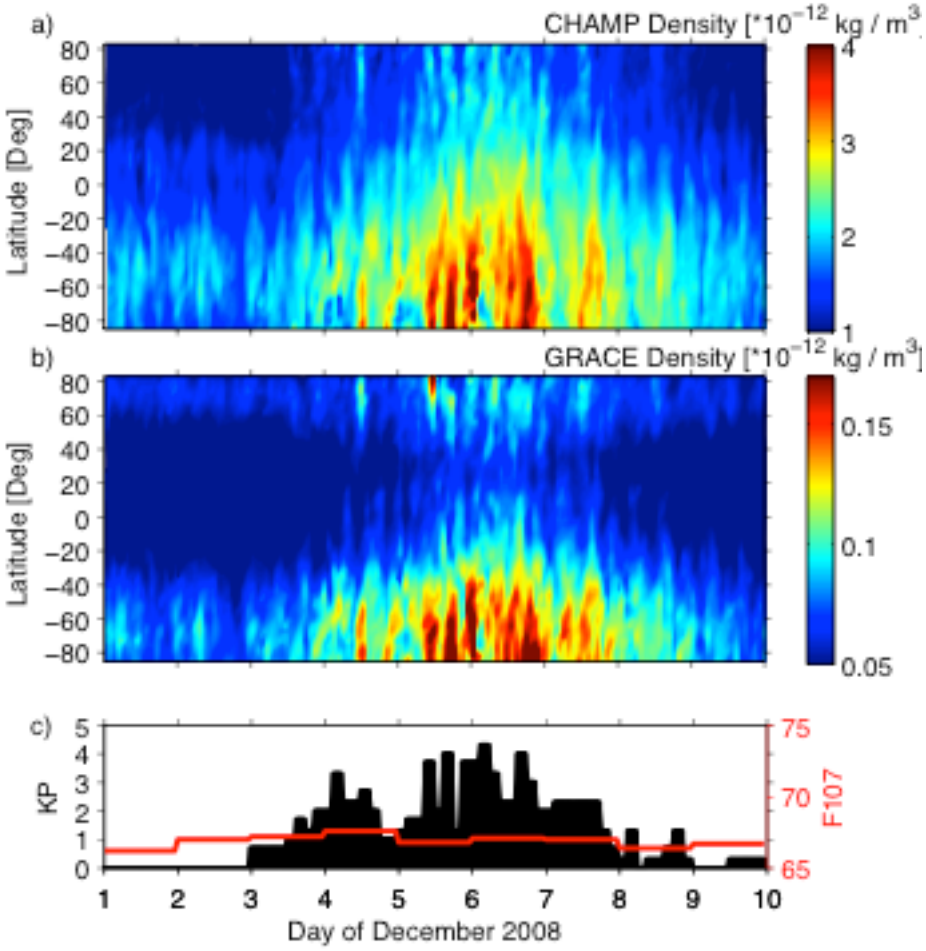

Figure 3.1. Latitudinal and UT variation of the thermosphere mass density near 09 LT from (a) CHAMP measurements normalized to 350 km and (b) GRACE measurements normalized to 500 km; (c) UT variations of the K_p index and $F_{10.7}$ index.

geomagnetically active times. However, the density structure progressing in latitude from the southern summer hemisphere to the northern winter hemisphere is different for the two fixed altitudes. This has been identified in previous studies [e.g., *Bruinsma and Forbes*, 2010; *Thayer et al.*, 2012] and Chapter 2 as a signature of a significant amount of He present at GRACE altitudes. This raises the question as to how would the neutral mass density be structured in

www.manaraa.com

latitude and altitude over the entire thermosphere. This Chapter investigates the latitude and altitude structure in neutral mass density throughout the thermosphere during this recent extreme solar minimum period and its response to geomagnetic activity.

3.3 Helium Estimation from CHAMP and GRACE Measurement

The claims stated in Chapter 2 and also concluded by *Bruinsma and Forbes* [2010] and *Thayer et al.* [2012] of substantial He in the winter hemisphere during this solar minimum are inferred from the relative difference in mass density between CHAMP and GRACE with latitude. There is no satellite presently in orbit carrying a neutral mass spectrometer to directly measure the upper atmosphere He concentration. Almost all the satellites carrying neutral mass spectrometers for *in situ* He measurements were flown in the 70's as described in Chapter 1. In this section, high-resolution accelerometer measurements from CHAMP and GRACE satellites are employed to extract the global distribution of the He concentration at the GRACE normalized altitude, ~500 km, during 01-10 December, 2008, when these two satellites were in coplanar orbits and separated in altitude by about 145 km. The method used to estimate the He concentration at the GRACE satellite altitude is provided in Appendix B.

Figure 3.2a,b shows the latitude variation of extracted He and O number densities using the method described in Appendix B, respectively, at the GRACE normalized altitude from 01-10 December 2008. This is the first time since the 1970's that the He number density with high spatial and temporal resolution can be estimated. It is the significant altitude separation between the two coplanar orbits that benefits the extraction of He. In essence CHAMP is low enough to

www.manaraa.com

serve as a reference for exospheric temperature variations with latitude and time assuming the CHAMP mass density is

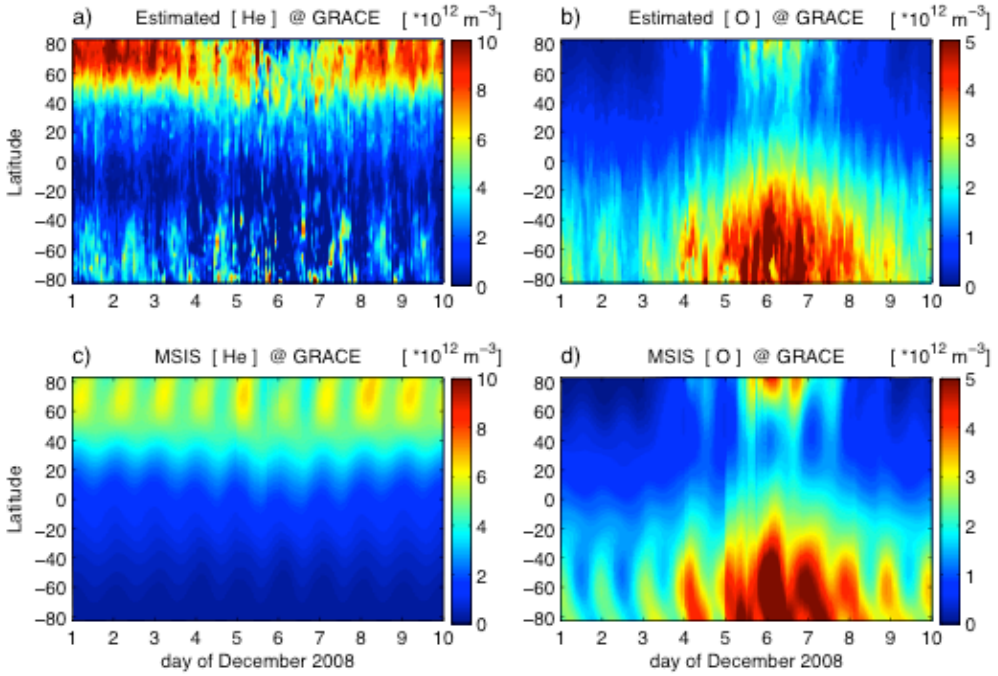

Figure 3.2. Latitudinal and UT variation of (a) helium and (b) oxygen number density at GRACE altitude estimated from CHAMP and GRACE satellite measurements; (c) The helium and (d) oxygen number density from adjusted MSIS estimation at GRACE altitude at 9 SLT.

composed primarily of O. That temperature structure can then be used to vertically extrapolate the O concentrations to the GRACE normalized altitude assuming O is in diffusive equilibrium. The difference between the extrapolated mass density from CHAMP to that of GRACE results in an estimate of He concentration that does not rely on He being in diffusive equilibrium.

Figure 3.2a illustrates a significantly larger amount of He concentrated in the winter hemisphere than in the summer. This clearly illustrates the phenomenon coined as the "winter

www.manaraa.com

helium bulge" by *Keating and Prior* [1968]. This study period provides an opportunity to observe the behavior of He and O at GRACE altitudes in the winter hemisphere from quiet geomagnetic activity (Dec 1-3), to active (Dec 4-7), back to quiet (Dec 8-10). The process of composition change due to geomagnetic activity has been studied extensively, particularly the behavior of atomic O and N_2 [*e.g., Duncan,* 1969*; Prölss et al.,* 1976*; Stubbe,* 1972; *Hays et al.,* 1973*; Rishbeth et al.,* 1985*; Fuller-Rowell et al.,* 1990, *Burns et al.,* 1995 and references therein]. Yet, it is helpful for later discussions to describe here the observed behavior of atomic O and He at a fixed altitude. As described by *Rishbeth et al.* [1987], vertical motions of constituents can be described in two forms: 1) by their contribution to satisfying the horizontal divergence of mass flux, "divergent" motion, and 2) by vertical expansion due to thermal enhancements, "barometric" motion. For a two-constituent gas, barometric motion of the two species is equal and at an altitude undergoing thermal expansion the constituents will increase based on the newly established pressure with the heavier species increasing in concentration more than the lighter species. This behavior is observed in Figure 3.2b where atomic O concentrations increase during geomagnetic activity. However, it is clear that He concentrations decrease during geomagnetic activity. The decrease in He must be associated with the concomitant presence of upward, vertical velocities due to divergent motion.

According to the Equation 1.23 in Chapter 1, the amount of departure from a diffusive equilibrium profile for the minor species due to vertical motion is $-\frac{u_z n_i(z) m_i}{H_P}[1-\frac{m_i}{m}]$, after combining the minor species momentum equation with its continuity equation. Here n_i is the

www.manaraa.com

number density of minor gas, U_z is the mass-averaged vertical wind, H_P is the pressure scale height of the major gas, m_i is the molecular mass of the minor gas and m is the mean molecular mass of the major gas. *Reber and Hays* [1973] demonstrated similar conclusions when they combined the minor species momentum and continuity equation with the major species momentum equation. Essentially the effect of a downward wind on a minor gas concentration whose molecular weight is less than the mean molecular weight is to increase the concentration of the minor gas. Similarly the effect of an upward wind is to decrease the concentration of the lighter minor gas. This can be shown by considering the wind term of the continuity equation where a downward wind is negative and with a lighter minor species the term becomes positive thus causing an increase in species concentration with time. The opposite is true for a minor species whose molecular weight is greater than the mean molecular weight. The end result is a redistribution of the species with altitude working to balance the molecular diffusion term with the vertical motion term in the continuity equation such that the species are not in diffusive equilibrium.

Helium, as a minor and lighter species during the active conditions, experiences a decrease in concentration as shown in figure 3.2a. This reduction in the winter helium bulge due to localized joule heating has been demonstrated, for example, by the AE-C mass spectrometer data [e.g., *Cageao et al.,* 1984]. This is indicative of upward vertical winds during the storm activity leading to a decrease in He density. The barometric vertical wind could offset some of the decrease in the He vertical distribution but, given helium's large pressure scale height, this mechanism is not very effective. For atomic O, the barometric change is larger while the vertical

www.manaraa.com

wind effect is weaker leading to an overall increase at GRACE altitudes. In our estimate of He described in the appendix, O was assumed to be in diffusive equilibrium. If accounting for any deviation from diffusive equilibrium due to upward vertical winds, the O concentration would be even higher than estimated at GRACE altitudes and the amount of He during active times would be estimated to be at an even lesser concentration.

In the quiet periods of Figure 3.2a,b, the winter hemisphere demonstrates a dramatic increase in He poleward of 40° N. This illustrates the departure of He from diffusive equilibrium due to downward divergent vertical velocities. In a similar but opposite manner to that described for active times, downward vertical velocities over the winter hemisphere during the quiet conditions will cause an increase in He concentration. With its inert nature and low molecular weight, helium is an excellent tracer of transport processes in the thermosphere.

Figure 3.2c and 3.2d display similar plots of the He and O number density from the NRL-MSIS00 model after the $F_{10.7}$ input to the model has been adjusted to better represent the low and middle latitude satellite observations, as described in the Appendix B. The NRL-MSIS00 model estimates a 30-70% lower He number density in the winter hemisphere during the quiet periods compared with the satellite estimated He number density shown in Figure 3.2a. The decrease in He number density during the active period is represented in the MSIS output, however, the magnitude of the depletion is much weaker in MSIS than the satellite estimation. The O number density from MSIS is very close to the satellite estimation in both quiet and active periods. The underestimation of He by MSIS may be associated with the extreme conditions of this solar minimum. Most of the He data in MSIS during solar minimum

www.manaraa.com

come from the AE satellite measurements near and during the 1976 solar minimum period. The solar minimum in 2008 was deeper than during that time and the functional representation of MSIS to extrapolate to the present minimum may not be appropriate. An explanation for excessive He in the winter hemisphere for this solar minimum may be related to the more contracted thermosphere resulting in steeper vertical gradients of the major species and greater diffusion of He upward.

The occurrence of He number density enhancements in the summer polar region in Figure 3.2a may be indicative of the uncertainties incurred using the method described in the appendix. One of the possible reasons is the longitudinal variation of exosphere temperature is too strong in the MSIS model, leading to a stronger oscillation of O density than expected. The enhancement of He density in the summer hemisphere is located exactly where the O density oscillates towards a minimum. Given the near constant local time over this period of observation, longitudinal effects will be observed in the data set. *Xu et al.* [2013] reported less than 16% relative longitudinal variation of daily mean mass density from the 2003 to 2008 CHAMP and GRACE data. However the longitudinal variation of O number density extracted in Figure 3.2b is more than 70%, indicating a stronger longitude variation in MSIS exosphere temperature than expected. Further descriptions of the conditions are needed to resolve uncertainties in the He concentrations in the summer polar region.

The contour plot shown in figure 3.3a is the latitude variation of $\log_{10}([He]/[O])$ at GRACE altitudes (~500 km) during the period 01-10 December 2008. The violet line indicates where the He number density, [He], is equal to the O number density [O]. The winter [He] in the

www.manaraa.com

polar region is

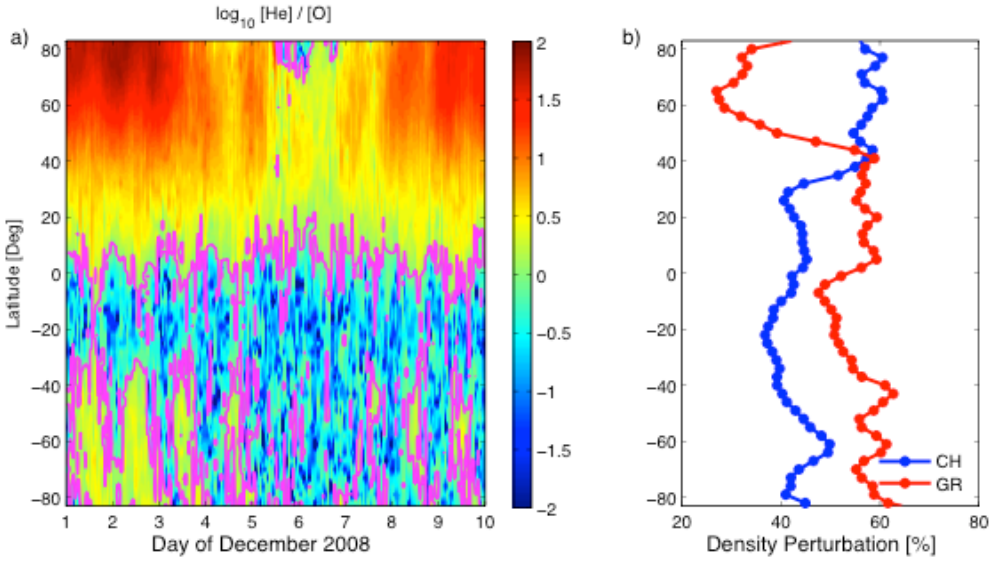

Figure 3.3 (a) Latitudinal and UT variation of the logarithm of the helium to oxygen number density ratio at GRACE altitude, (b) The latitudinal profile of the mass density perturbation in percent change (%) during the geomagnetic active period Dec 05-06, 2008 at CHAMP and GRACE altitudes.

nearly 70 times greater than the [O] before the storm started and about 30-40 times greater in the recovery period following the storm. Oxygen is dominant throughout the summer hemisphere. During the storm-time period, the neutral gas in the winter polar region switches from being predominantly He to predominantly O. The predominate gas at CHAMP altitudes remains atomic O for all latitudes from summer to winter for both geomagnetic quiet and active periods. Chapter 2 shows that the mass density response to geomagnetic activity is the combined influence of variations in temperature and composition change and that the response at GRACE altitudes will prove complex due to the dynamics of the He/O transition region. So, when comparing the mass density perturbation difference at CHAMP and GRACE during a

www.manaraa.com

geomagnetic storm, the differing behavior of He and O with altitude will result in a structured mass density response.

In order to investigate the mass density response to a geomagnetic storm in the He/O composition transition region, a comparison between CHAMP and GRACE mass density perturbations has been carried out and displayed in Figure 3.3b. Figure 3.3b is the latitude variation of the density perturbation expressed as a percent change by $(\frac{\rho^{Storm}}{\rho^{Quiet}}-1)\times 100$. Here the storm-time mean density is the mean over the storm main phase period 05-06 December 2008 and the quiet-time mean density is the mean over the recovering post-storm period 09-10 December 2008. Note the thermosphere was extremely quiet before the storm, and the MSISE00 modeling cannot well represent the mass density in the extreme geomagnetic quiet period in this solar minimum, so the post-storm period was chosen as the reference period. Because about 98% of the constituents of the gas are He and O at the altitude range between CHAMP and GRACE altitudes during this solar minimum, the mean molecular weight $\overline{m}$ can be approximately written as a function of $[He]/[O]$,

$$\overline{m}=\frac{4([He]/[O]+4)}{[He]/[O]+1} \qquad Eq\ (3.1)$$

The mean molecular weight, $\overline{m}$, decreases as the [He]/[O] increases but in a nonlinear manner. The [He]/[O] variation in Figure 3.3a serves as a reference of mean molecular weight variation at GRACE according to Equation (3.1), and Figure 3.3b is the density disturbance due to the combined influence of both temperature and mean molecular weight change. The density perturbation from quiet to active conditions is positive for all latitudes indicating the mass

www.manaraa.com

density increases from quiet to active conditions, as expected, but with a great deal of variability with latitude in the amount of change. From the summer hemisphere through the equatorial region, mass density perturbations at GRACE altitudes exceed those at CHAMP altitudes. This is indicative of mostly temperature influencing the response with little composition change, and is supported by Figure 3.3a with the composition being primarily O over this latitude region. Northward of about 40°N, the perturbation in mass density at GRACE altitudes increases less than at lower latitudes and less than at CHAMP altitudes. This response is indicative of composition change offsetting the temperature resulting in the density perturbation being less than in the summer hemisphere. In the winter polar region at GRACE altitudes, He concentrations dominate during geomagnetic quiet times, while O dominates during geomagnetic active times, which makes the mean molecular weight change significant in this region, as implied by Figure 3.3a.

The above description illustrates the tradeoff between temperature enhancements and mean molecular weight enhancements, such that, the corresponding density perturbation to geomagnetic storms varies with latitude and altitude. Note that besides temperature and mean molecular weight change, the change of vertical gradient of mean molecular weight will also modify the density response to geomagnetic storm as demonstrated in Chapter 2. A more complete and comprehensive study on how these factors affect the storm period mass density perturbation requires the inclusion of He in general circulation models (GCMs) of the thermosphere. This capability is lacking in GCM's but an effort to include He as a major and minor gas in the TIEGCM is described in Chapter 4 and 5. The following discussion will use the

www.manaraa.com

NRL-MSISE00 model to help describe the observed behavior but not provide the physical descriptions necessary to elucidate explicitly the processes at play.

3.4 Mass Density and Scale Height Perturbations

3.4.1 Storm time mass density perturbation in MSIS

As mentioned in the observation section, the altitude variation of the mass density response to the geomagnetic storm is related to the mass density scale height change during storm time, which is impacted by temperature and composition changes. Owing to the present exclusion of He in community thermospheric general circulation models, the NRL-MSISE00 is employed to describe how the changing composition with height impacts the mass density response to geomagnetic storms throughout the thermosphere. In order for the MSIS model to better represent this extreme solar minimum, the same adjustments as shown in Chapter 2 have been applied to the MSISE00 model. Figure 3.4 shows the MSIS estimate of the mass density perturbation with latitude and altitude during the same storm time period as shown in the observation section (section 3.3). As before, the mass density perturbation in Figure 3.4 is calculated using percent change, $(\frac{\rho^{Storm}}{\rho^{Quiet}} - 1) \times 100$. The storm-time value is the mean over the period 05-06 December 2008 and the referenced quiet-time value is the mean over the post-storm period 09-10 December 2008, for here and all the following MSIS estimates. The purple line displayed in Figure 3.4 indicates the altitude where the maximum density percent change occurs.

www.manaraa.com

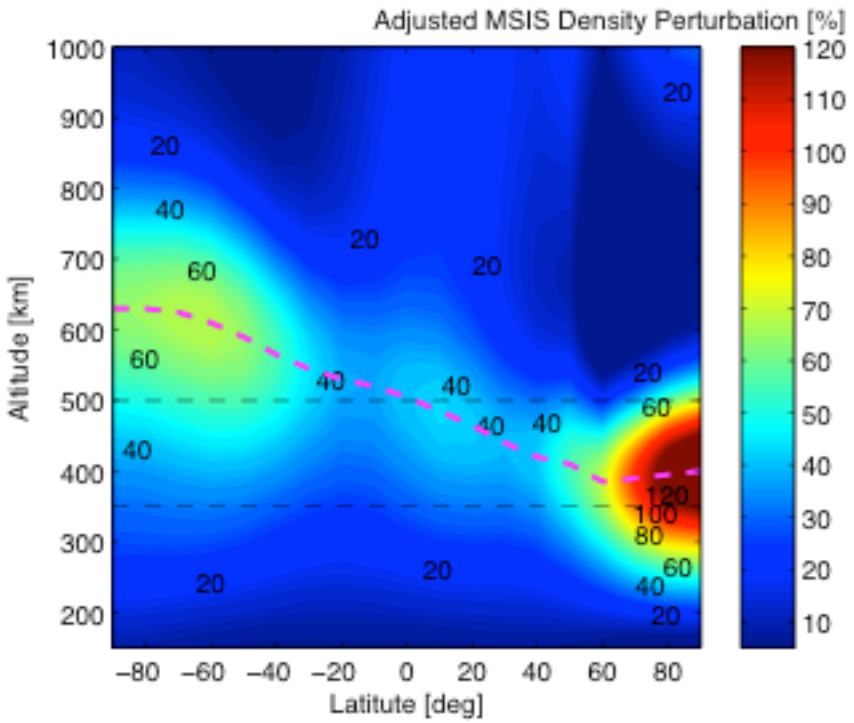

Figure 3.4. Altitudinal and latitudinal variations of the mass density perturbation in percent change (%) during the Dec 05-06, 2008 geomagnetic storm from the adjusted NRL-MSISE00 estimation. The black dash lines indicate the CHAMP and GRACE altitudes.

The adjusted MSIS estimates of mass density percent change at GRACE and CHAMP mean altitudes are indicated by the dashed line in Figure 3.4 and can be directly compared to the observations presented in Figure 3.3b. As illustrated in Figure 3.3b, southward of 40° N, the density percent change increases with height (GRACE density perturbation > CHAMP density perturbation). This variation is consistent with the MSIS estimates in the lower altitude region below the purple line in Figure 3.4. Near 45° N, the GRACE density perturbation is approximately equal to the CHAMP density perturbation followed by the GRACE density perturbation decreasing with increasing northward latitude (GRACE density perturbation < CHAMP density perturbation). This variation is consistent with the MSIS estimate in the higher altitude region above the purple line in Figure 3.4, where there is rapid change in the density

www.manaraa.com

response with altitude when progressing towards the winter pole. Note that the GRACE density perturbation begins to increase again in Figure 3.3b from 65° N poleward and this is reflected in the adjusted MSIS estimate, suggesting a latitude structure in He at GRACE altitudes with the minimum perturbation occurring near 65° N. Furthermore, CHAMP observes an increase in mass density perturbation north of 40° N that is consistent with the behavior described by the adjusted MSIS in Figure 3.4.

This described behavior is consistent with a changing O/He transition altitude with latitude. Because the thermosphere temperature is uniform above ~200 km, composition change plays a critical role in the altitude response of mass density perturbations during geomagnetic activity. The altitude variations of the density perturbation behave in an expected manner when dominated by a single species; the density perturbation increases with height due to the pressure scale height being driven by primarily temperature changes. However, in composition transition regions, like He/O or O/N_2, significant composition effects suppress the altitude behavior of the density perturbation and make the density enhancement less significant with altitude. The extreme solar minimum conditions accentuate this effect as the atmosphere is more contracted and thus transition regions occur over shorter altitude ranges and have greater variability.

3.4.2 Parameters that affect the mass density perturbations

Given that the adjusted MSIS model provides reasonable description of the observations, a quantitative assessment of the contributing parameters that affect the mass density response to geomagnetic activity can be made by expressing the density temporal ratio as:

www.manaraa.com

$$\frac{\rho^{Storm}}{\rho^{Quiet}} = \frac{\overline{m}^{Storm}}{\overline{m}^{Quiet}} \frac{P^{Storm}}{P^{Quiet}} \frac{T^{Quiet}}{T^{Storm}} \qquad Eq\ (3.2)$$

where T is the temperature and P is the atmosphere pressure. The superscript *Quiet* means the quiet time period and *Storm* means the active period described above and the contributing variables to the mass density percent change are provided in Figure 3.5 for summer and winter conditions. Figure 3.5a shows the mean molecular weight with altitude during quiet times and storm times for 75° S in the summer hemisphere. The mean molecular weight variation in Figure 3.5a illustrates that the mean molecular weight is near 16 from 350 km to 500 km in the polar region of the summer hemisphere indicating an O-dominated region. Under this circumstance, Figure 3.5b gives the altitude variation for each term in Equation (3.2). The temperature variation T^{Quiet} / T^{Storm} is unchanged over this altitude range. The mean molecular weight enhancement $\overline{m}^{Storm} / \overline{m}^{Quiet}$ is quite small and almost remains unchanged below 500 km because of the dominance in O before and during the storm. The pressure perturbation P^{Storm} / P^{Quiet} is the dominant contributor to the density temporal ratio $\rho^{Storm} / \rho^{Quiet}$ in the summer hemisphere at 75° S. The green dashed lines in Figure 3.5b show the mean altitude of CHAMP and GRACE satellite and the density perturbation $\rho^{Storm} / \rho^{Quiet}$ is greater at GRACE altitudes than CHAMP altitudes, as expected from discussions related to Figures 3.3 and 3.4.

Figures 3.5c and 3.5d apply the same MSIS estimation as in 3.5a and 3.5b but for the winter hemisphere near 75° N. The quiet time mean molecular weight in Figure 3.5c demonstrates that He is dominant near GRACE altitudes with a weak mixture of He in the more dominant O atmosphere at CHAMP altitudes. The transition altitude from O dominant to He dominant

www.manaraa.com

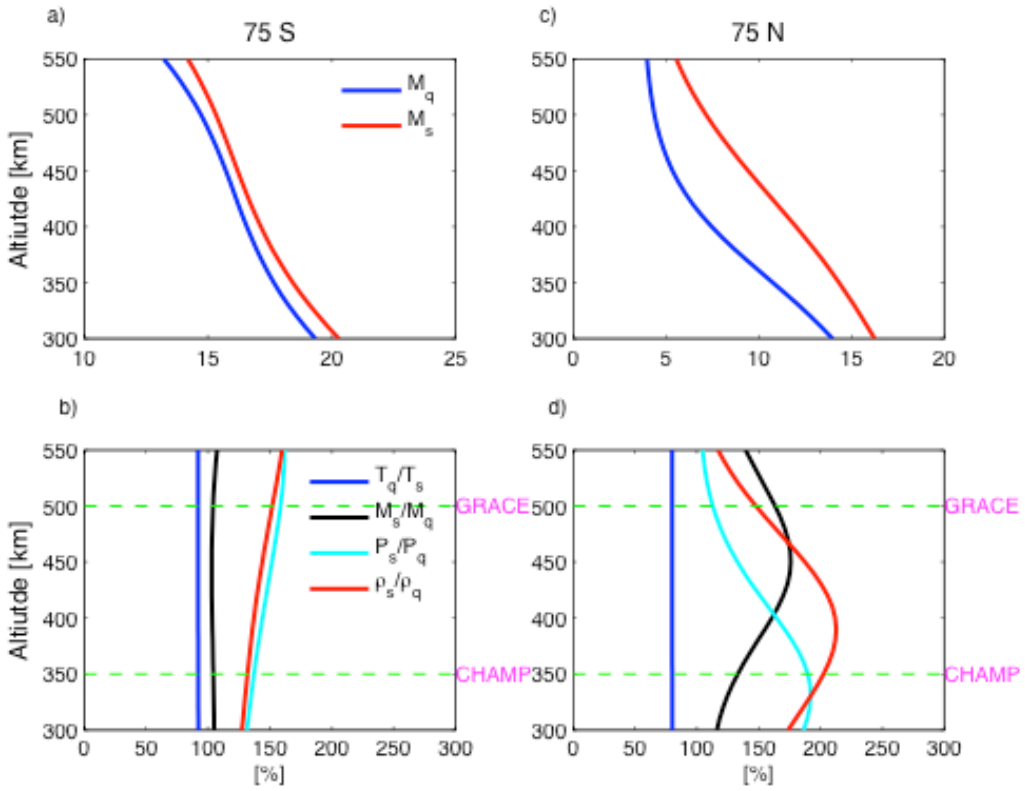

Figure 3.5. (a) Altitudinal variation of mean molecular weight averaged over the geomagnetic quiet and active period at 75 S, (b) Altitude variation of the temperature percent change, mean molecular weight percent change, pressure percent change and density percent change during the geomagnetic storm at 75 S; (c) and (d) are similar to (a) and (b) but at 75 N. All the results in Figure 5 are from NRL-MSISE00 estimation. The quiet period is Dec 09-10 and the active period is Dec 05-06, 2008.

lies between the CHAMP and GRACE altitudes in the winter hemisphere. Under this circumstance, the mean molecular weight perturbation $\overline{m}^{Storm} / \overline{m}^{Quiet}$ is significantly enhanced and the O/He transition region lies near 350 km as shown in Figure 3.5c. The pressure perturbation P^{Storm} / P^{Quiet} is the main contributor to the density perturbation below 400 km, however, above 400 km the mean molecular weight perturbation $\overline{m}^{Storm} / \overline{m}^{Quiet}$ exceeds the pressure perturbation and becomes the main reason for the behavior in the density perturbation.

www.manaraa.com

3.4.3 Parameters that affect mass density scale height perturbations

The previous section, 3.4.2, analyzed the contribution of pressure, mean molecular weight and temperature to temporal changes in mass density at specific latitudes. To describe how the mass density will behave with altitude at a specific time, the mass density scale height, H_ρ, is applied.

The altitude distribution of mass density at any one time will depend on the vertical distributions of pressure, mean molecular weight and temperature. To observe the effects of geomagnetic activity on the altitude distribution of mass density, the percent change in the mass density scale height from quiet to active conditions is calculated, $\delta H_\rho = (\frac{H_\rho^{Storm}}{H_\rho^{Quiet}} - 1) \times 100$, in a similar manner as the adjusted MSIS mass density percent change was calculated in Figure 3.4. According to the Equation 1.27 in Chapter 1, The mass density percent change can be expressed in terms of its scale height percent change as $\delta\rho = (\delta\rho_0 + 1)\exp(\int_{h_0}^{h} \delta H_\rho \frac{1}{H_\rho^{Storm}} dh) - 1$. Thus, the mass density percent change $\delta\rho$ is related to the integral of the density scale height percent change δH_ρ weighted by the storm time inverse density scale height $\frac{1}{H_\rho^{Storm}}$.

The purple line, originally displayed in Figure 3.4 indicating the altitude where the maximum density perturbation occurs, is also included in Figure 3.6. Notice this purple line in Figure 3.6 is located exactly where the mass density scale height perturbation is zero, meaning there is no scale height change at this altitude when transitioning from quiet to active conditions. As illustrated in Figure 3.6, the density scale height perturbation below the purple line is positive,

www.manaraa.com

so the mass density response to the storm will increase with altitude, as shown in Figure 3.4, due to the integrated effect of the scale height change. In the altitude band above the purple line (about 650-1000 km in summer and 400-700 km in winter), the density scale height perturbation is negative, and the mass density response from quiet to active conditions will not increase as much as at lower altitudes. The O/He transition has a much greater impact on the density scale height perturbation than the O/N_2 transition. The O/He transition reverses the altitude trend in mass density scale height. This explains the relatively smaller

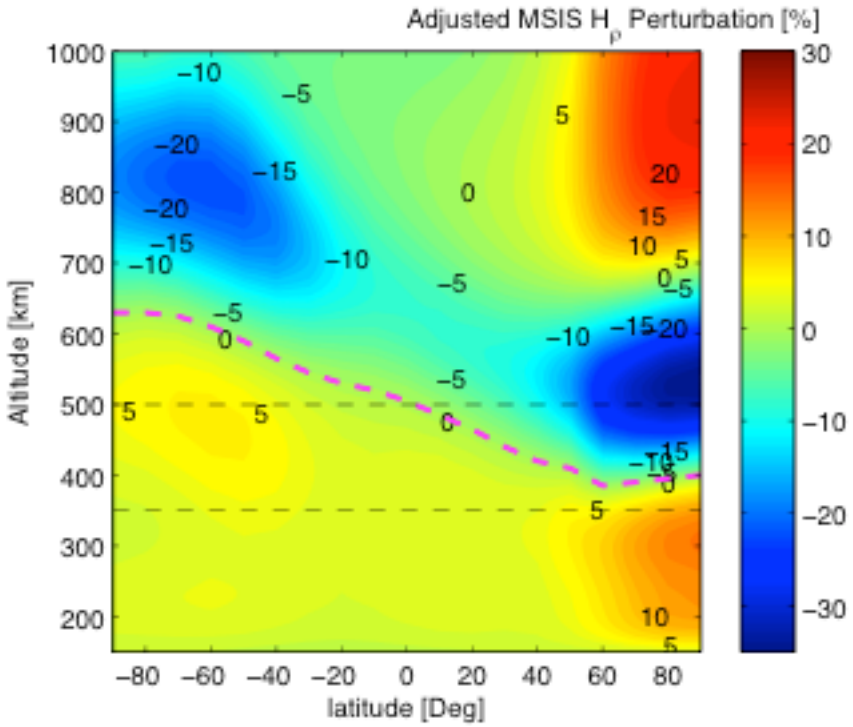

Figure 3.6. Altitudinal and latitudinal variations of the mass density scale height perturbation in percent change (%) during the Dec 05-06, 2008 geomagnetic storm from the adjusted MSIS estimation. The black dash lines indicate the CHAMP and GRACE altitudes. The purple dash line, originally displayed in Figure 3.4, indicating the altitude where the maximum density perturbation occurs.

response in density perturbation with altitude above the purple line shown in Figure 3.4. Note above 700 km in the winter hemisphere, there is another layer with greater density scale height

www.manaraa.com

perturbation, the dominant species in this layer is pure He both in quiet time and storm time, so the temperature enhancement effect becomes dominant again. This layer should also exist in the summer hemisphere but the altitude will be above the 1000 km altitude due to the summer hemisphere being much more expanded than the more contracted winter hemisphere during this solar minimum. Although composition change is clearly the factor that influences how the mass density will respond in altitude to geomagnetic activity, the explicit contribution requires further elaboration of pressure and molecular weight scale height contributions.

3.4.3.1 Contribution of the H_P perturbation to the H_ρ variations

In order to simplify the text, the total mass density scale height, H_ρ, will be symbolized as ρ scale height, the pressure scale height, H_P, will be symbolized as P scale height, and the mean molecular weight scale height, $H_{\overline{m}}$, will be symbolized as $\overline{m}$ scale height in the following discussion.

Because temperature is almost unchanged with altitude above 250 km, the ρ scale height is determined by both the P scale height and the $\overline{m}$ scale height above 250 km. When the vertical gradient of the logarithmic mean molecular weight is very small, $\overline{m}$ scale height is negligible and the ρ scale height variation is approximately equal to the P scale height variation. The P scale height is a combination of both temperature and mean molecular weight. Figure 3.7 illustrates the perturbation of temperature, mean molecular weight, and P scale height during the December 05-06, 2008 geomagnetic storm. Again, perturbation values are calculated as a percent change between quiet and active periods. The temperature enhancement with altitude over all latitudes, shown in Figure 3.7a, supports that the temperature enhancement is

www.manaraa.com

uniform above 200 km. The temperature perturbation is larger in the winter hemisphere than the summer hemisphere and is more significant in the polar region than the equatorial region. The mean molecular weight perturbation shown in Figure 3.7b clearly illustrates a band of increased mean molecular weight during storm conditions that is associated with the dynamics of the O/He transition region. The increased perturbation in molecular weight is due to the increase in atomic O accompanied by a decrease in He at these altitudes during storm conditions, as shown in Figure 3.2 and described in section 3.3. Also, a larger enhancement occurs in the winter hemisphere than in the summer hemisphere due to the colder and more contracted winter hemisphere. The composition change with altitude in the winter hemisphere is more rapid resulting in a more significant disturbance of mean molecular weight during geomagnetically active times. The mean molecular weight perturbation near the O/He transition region is far more significant than the increase that occurs near the O/N_2 transition at lower altitudes. Furthermore, the O/He mean molecular weight perturbation is about twice the temperature perturbation in both summer and winter. Consequently, in the region near the O/He transition, the P scale height perturbation shown in Figure 3.7c is negative indicating that the P scale height actually decreases in this band of composition change. A much weaker decrease in P scale height, while still remaining positive, can also be seen near the O/N_2 transition region in the summer hemisphere of Figure 3.7c. In the regions where composition does not change significantly from quiet to storm conditions, the P scale height perturbation is positive, driven primarily by the increase in temperature.

www.manaraa.com

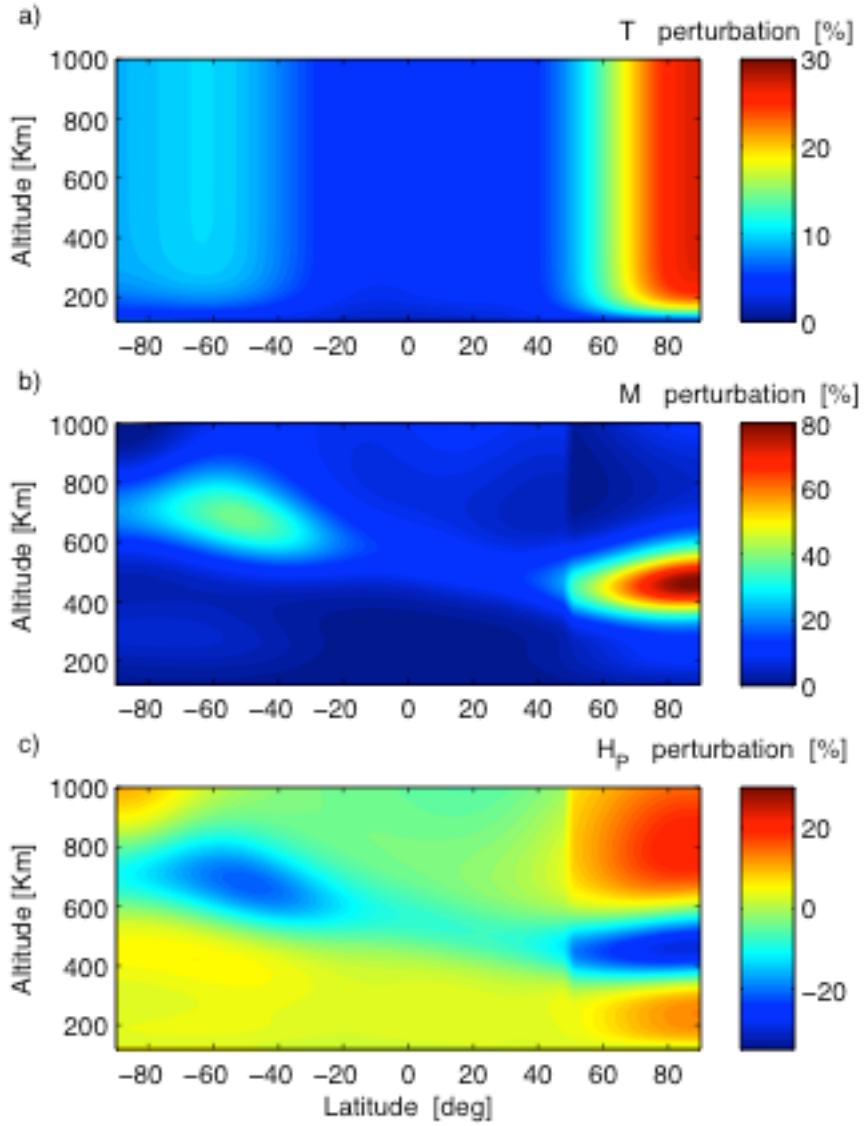

Figure 3.7. Altitudinal and latitudinal variation of the (a) temperature percent change (b) mean molecular weight percent change (c) pressure scale height percent change during geomagnetic active period Dec 05-06, 2008 by the adjusted MSIS estimation. The reference quiet time period is Dec 09-10, 2008.

The pattern of the P scale height perturbation with altitude described above is similar to the ρ scale height perturbation with altitude shown in Figure 3.6 with all of the altitude structure attributed to composition dynamics. However, there is also a shift in altitude of the

www.manaraa.com

relative positions in structure that results in differences between these two patterns. That difference is related to the $\overline{m}$ scale height perturbation.

3.4.3.2 Contribution of the $H_{\overline{m}}$ perturbation to the H_{ρ} variations

Little attention has been paid to the $\overline{m}$ scale height in former research on mass density changes because it is often very large compared to P scale height – recall that it is the inverse of these scale heights that contribute to density change. However, Chapter 2 demonstrates the importance of the $\overline{m}$ scale height in the O/He transition region to describe mass density change at GRACE altitudes during this recent solar minimum. Figure 3.8 shows the relation among number density, transition height, mean molecular weight and $\overline{m}$ scale height. All the values shown in Figure 3.8 are the average of adjusted MSIS model output over the quiet-time and active periods at 75° N winter hemisphere. Figure 3.8a illustrates the altitude variation of the fractional amount of He number density to O number density during quiet and active conditions, and indicates the location of the transition altitude where the two concentrations are equal. The transition point where the O concentration equals the He concentration is about 360 km for the quiet time period. Figure 3.8b is similar to Figure 3.8a but for the N_2/O transition region. The transition altitude from N_2 to O in number density is near 160 km during quiet conditions. Figure 3.8c illustrates the distribution of the mean molecular weight with altitude. The mean molecular weight is about 22 at 160 km, decreases to about 4 above 500 km and approaches 1 at 1000 km. The decrease of the mean molecular weight with altitude is not linear. Figure 3.8c shows a decrease of mean molecular weight around the N_2/O transition region (150~200 km) and another

www.manaraa.com

more significant decrease near the O/He transition region (350~400 km). A larger decrease in mean molecular weight indicates a smaller $\overline{m}$ scale height as illustrated in Figure 3.8d. Large $\overline{m}$ scale heights indicate regions of uniform composition while transitions in composition lie near minima in $\overline{m}$ scale height. The minima are not collocated with the transition altitudes shown in Figure 3.7a,b because the $\overline{m}$ scale height is the inverse of the natural logarithm of the vertical gradient in molecular weight, such that, both the mean molecular weight value and its gradient contribute to the scale height. The minima are important because it is the inverse of the $\overline{m}$ scale height that contributes to the mass density change. There are two minima in $\overline{m}$ scale

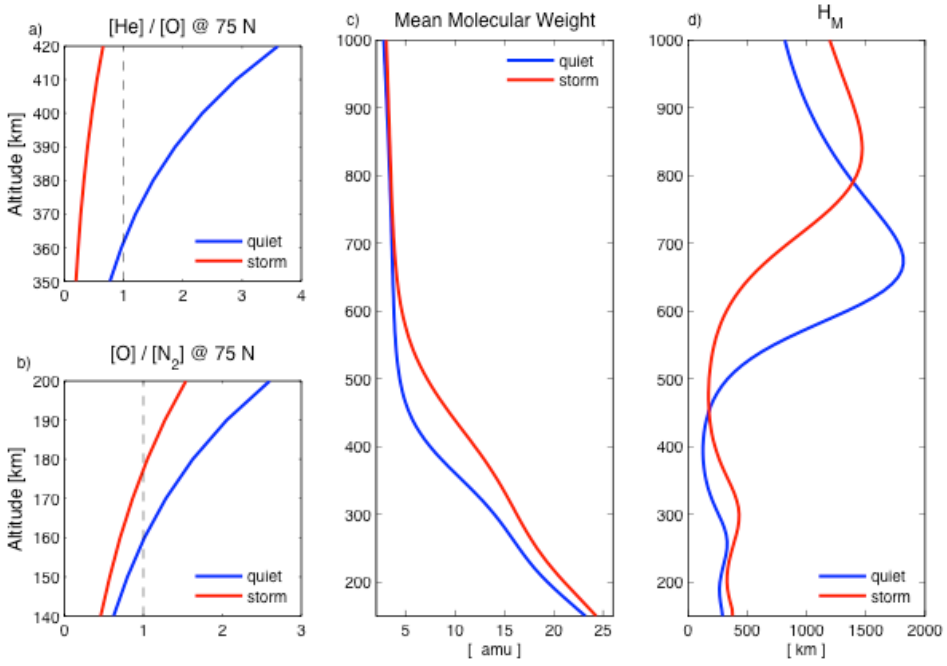

Figure 3.8. Altitudinal variation of the (a) helium to oxygen number density ratio (b) oxygen to molecular nitrogen number density ratio (c) mean molecular weight (d) mean molecular weight scale height during geomagnetic quiet and active period; All the results in Figure 8 are from adjusted MSIS estimation. The quiet period is Dec 09-10 and the active period is Dec 05-06, 2008.

www.manaraa.com

height with altitude, the first is near 180 km and is associated with the N_2/O transition region, and the second is near 400 km and is associated with the O/He transition region. These minima shift in altitude with increasing geomagnetic activity due to the expansion of heavier species to higher altitudes and the decrease in lighter species due to vertical winds.

Figure 3.9a illustrates the $\overline{m}$ scale height perturbation in the same manner as the P scale height perturbation shown in Figure 3.7. The latitude and altitude structure are similar to the P scale height perturbation with maximum contributions coming near composition transition

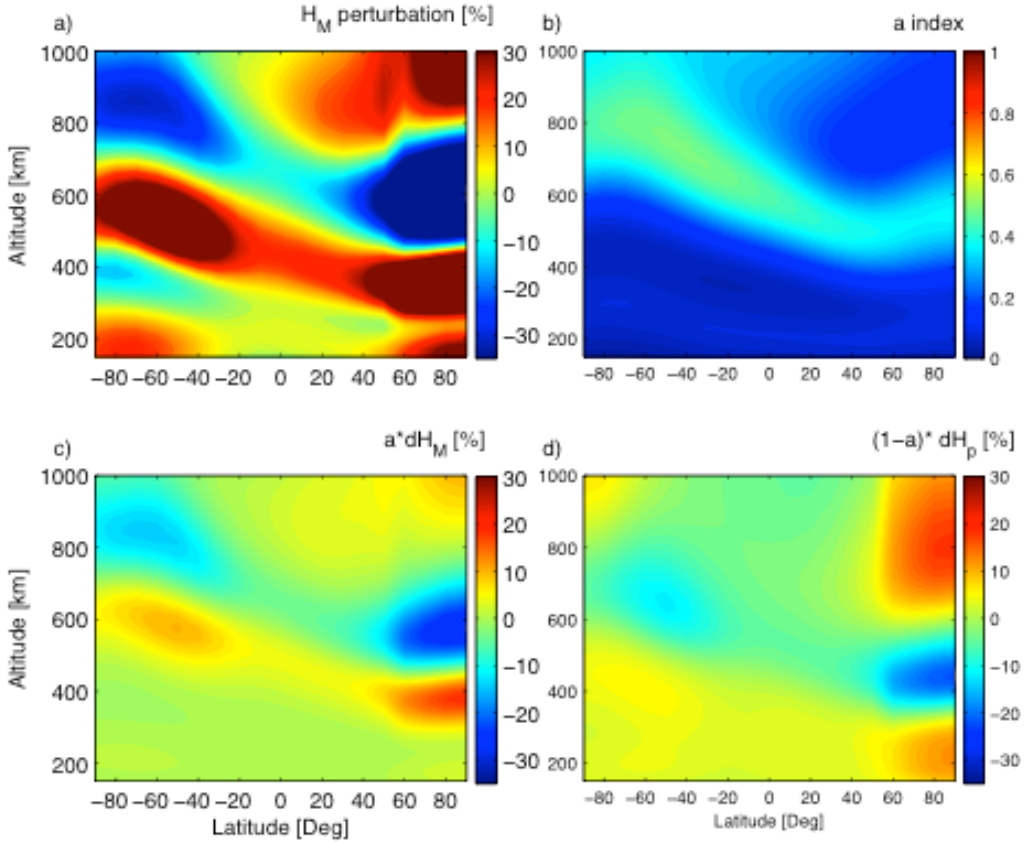

Figure 3.9 Altitudinal and latitudinal variation of (a) the mean molecular weight scale height perturbations (b) storm-time weighting factor a index (c) weighted mean molecular weight scale height perturbation (d) weighted pressure scale height perturbation during geomagnetic active period Dec 05-06, 2008 by the adjusted MSIS estimation. The reference quiet time period is Dec 09-10, 2008.

www.manaraa.com

altitudes – see Figure 3.8d. The $\overline{m}$ scale height perturbation is more dynamic than the P scale height perturbation. There are essentially two minima troughs of $\overline{m}$ scale height with altitude, and the position of these two troughs goes up during geomagnetic activity without significant changes in the troughs values. This makes the $\overline{m}$ scale height perturbation alternate between positive and negative perturbations with altitude. However, the position of the maxima and minima are not in phase with the P scale height perturbations leading to competing contributions to the ρ scale height perturbation. A direct relationship equating the ρ scale height perturbation, δH_{ρ}, to the $\overline{m}$ scale height perturbation, $\delta H_{\overline{m}}$, and the P scale height perturbation, dH_p, at fixed altitude can be derived and written as,

$$\delta H_{\rho} = a\delta H_{\overline{m}} + (1-a)\delta H_{P} \;,\; where\; a = \frac{H_p^{Storm}}{H_{\overline{m}}^{Storm} + H_p^{Storm}}$$

This relationship indicates a weighting factor, a index, between the two contributions that depends on the values of the actual P scale height and $\overline{m}$ scale heights during storm time. When the weighting factor is small due to a large storm-time $\overline{m}$ scale height, the ρ scale height perturbation will closely follow the P scale height perturbation. The $\overline{m}$ scale height during the storm period has been shown in Figure 8d to be generally quite large, but at certain altitudes minimum values of less than 300 km can occur. In these minima regions the storm-time weighting factor will be largest and the $\overline{m}$ scale height perturbations will increase its relative contribution to ρ scale height perturbations. Figure 3.9b is a plot of the storm-time weighting factor. Two bands of enhanced weighting factor can be identified. The weakest band is about

www.manaraa.com

100 km in vertical extent near an altitude of 400 km in summer and stretches to the winter hemisphere where it is thinner and peaks near 200 km altitude. The strongest band is a few hundred kilometers in altitude extent in the summer centered at 800 km altitude and stretches to the winter hemisphere where it narrows to just 100 km and is centered near 550 km altitude. In the higher altitude band the storm-time weighting factor nearly reaches a value of 0.5 indicating that the storm-time P scale height and $\overline{m}$ scale heights are nearly the same. This is likely to occur in this higher band as the P scale height increases with decreasing molecular weight through the O/He transition while the $\overline{m}$ scale height actually decreases through the same region.

Figure 3.9c,d provides the storm-time weighted values of the $\overline{m}$ scale height perturbation and P scale height perturbation that add to give the ρ scale height perturbation shown in Figure 3.6. These are basically the same format as in Figures 3.9a and 3.7c but weighted in latitude and altitude by the storm-time weighting factor. In comparison, the two contributions are of similar values but their distributions with altitude differ. This difference in altitude between the two patterns is expected given that the P scale height perturbation structure with altitude depends on the change in the mean molecular weight value while the $\overline{m}$ scale height perturbation structure with altitude depends on the change in the logarithmic vertical gradient of mean molecular weight. As such, the maxima and minima between the two contributions are close but will not be aligned with altitude. This results in the ρ scale height perturbation having broader regions of positive and negative values with reduced maxima and minima.

A revisit of the maximum density perturbation line in Figure 3.4, or the equivalent zero line

www.manaraa.com

perturbation in ρ scale height perturbation shown in Figure 3.6, can now be examined in terms of the contributing factors. This region must be where the storm-time weighted P scale height perturbation, *(1-a)* dH_p, equals the storm-time weighted $\overline{m}$ scale height perturbation, $a\delta H_{\overline{m}}$. By inspection, the value of the *a* index along the line is rather small. However, the $\overline{m}$ scale height perturbation is near maximum along the line while the P scale height perturbation is going through a minimum - as the mean molecular weight increases more significantly than the temperature. Consequently the two terms equate to produce no change in the ρ scale height perturbation. The increase in mean molecular weight is caused by the enhancement in O over He in the active times, as was shown and discussed in Figure 3.3. This composition change causes the $\overline{m}$ scale height to increase and offset the decrease in the P scale height, resulting in no change in the ρ scale height. The zero line is inclined with latitude due to the effect of temperature on the local transition region from O to He.

3.5 Conclusion

The O/He transition region is a critical region for the study of understanding the thermosphere mass density behavior during the recent solar minimum. The cold, contracted solar minimum thermosphere resulted in extremely low O/He transition altitudes in the winter hemisphere leading to complex behavior in mass density response to geomagnetic activity. Using coplanar orbits of CHAMP and GRACE accelerometer data, He number densities at GRACE altitudes were extracted and analyzed for the period from 01-10 December 2008 near 09 LT. The interpreted estimates of He represent the most detailed, spatially and temporally, description of

www.manaraa.com

winter-time, solar-minimum He since it was first measured during the solar minimum period around 1976. The winter hemisphere helium bulge is clearly observed with He concentrations during quiet geomagnetic activity exceeding estimates from the $F_{10.7}$-adjusted NRLMSIS00 model by 30-70%. The He estimates at GRACE altitudes also displayed dynamic changes in concentration in the winter hemisphere during geomagnetic activity with a decrease in concentration in regions presumably composed of upward vertical velocities. Concurrently atomic O concentrations increased due to the associated thermal expansion and upward vertical winds during geomagnetic activity.

The change in relative O/He concentrations significantly modifies the vertical distribution of molecular weight and pressure at these altitudes and has a direct consequence on the vertical behavior of the thermosphere mass density when transitioning from quiet to active conditions. Upon adjusting MSIS to better represent the observations, the model was used to study the altitude variations in thermosphere mass density when transitioning from quiet to active times imposed by composition changes. The following summarizes the conclusions: 1) The thermosphere mass density perturbation is positive over all altitudes in response to geomagnetic activity with the maximum perturbation occurring near the O/He transition region and a much weaker maximum near the N_2/O transition region. 2) The altitude of maximum density perturbation occurs where there is no change in the density scale height. For this to occur, the perturbation in the weighted pressure scale height must be equal and opposite to the perturbation in the weighted mean molecular weight scale height – an altitude close, but not exactly, at the location of the O/He transition altitude in number density. Above this altitude of maximum

www.manaraa.com

response, the mass density perturbation to geomagnetic activity is suppressed and can result in a lesser increase than at lower altitudes; as observed with the mass density perturbation at GRACE altitudes being less than at CHAMP altitudes in the winter polar regions during the December 2008 period. This behavior is very sensitive to the dynamics of the O/He transition region compared with the other altitudes.

Analysis of the change in mass density scale height to geomagnetic activity using an adjusted MSIS model revealed altitude regions of positive and negative change. This altitude structure resulted from the combined influences of pressure scale height change and molecular weight scale height change. The contribution of the mean molecular weight scale height perturbation to the density scale height perturbation could reach 50% around the O/He transition region during the 2008 solar minimum period. Consequently using the pressure scale height to analyze the mass density perturbation will be significantly in error near the O/He transition region. It is important to get the He concentration and the O/He transition altitude correct in the model to better simulate the mass density response to geomagnetic storm in O/He transition region, which enable a better study of the satellite drag at these altitudes.

www.manaraa.com

Chapter 4 TIEGCM with Helium module

4.1 Introduction

The altitudes where He concentrations exceed O occur at a much lower altitude in the thermosphere with steeper vertical gradients during the recent solar minimum 2007-2010, particularly in the winter hemisphere because of the existence of the winter helium bulge. Thus, the impact of He in physics-based thermosphere models cannot be neglected at the higher altitudes, especially during extreme solar minima. However, the physics-based models in general do not include the He constituent in their description of the thermosphere.

Kim et al. [2012] incorporated He from the NRL-MSISE00 model into the NCAR-TIEGCM model to indicate the changes that would occur to certain thermosphere properties. They found significant changes to the values for specific heat and thermal conductivity, minor changes to molecular viscosity, leading to some decrease in the mass density at the CHAMP altitude. However, the method to couple the He from MSISE00 into the TIEGCM is not self-consistent, and thus the model parameters such as temperature, wind, mass mixing ratio of the atmosphere constituent will not re-adjust to the He implemented using this method. In addition, *Thayer et al.* [2012] and Chapter 2 and 3 suggest the NRL-MSIS00 simulation does not represent the observations well in the extreme solar minimum in 2008.

In this chapter, the TIEGCM with an augmented He module developed by Eric Sutton [private communication] treats He as a major species in the model. In this approach, the He gas

www.manaraa.com

interacts with the other major gases of the thermosphere and the changes of He distribution in the model can influence the properties of the thermosphere. This is the first time such an implementation has been attempted and requires thorough evaluation to insure the module is functioning properly. The research described in Chapter's 2 and 3 provide a means to evaluate the major He module in the TIEGCM. Thus, in this chapter, differences between the modeling results of the TIEGCM without He and with He will be analyzed.

4.2 Numerical experiments

The He was implemented into the TIEGCM as a major species by Eric Sutton [private communication] over this last year. In the He major species model, the morphology of N_2, O_2 and O are affected by the He distribution. The mass mixing ratio of each species readjusts, and as a result causes significant decreases in mean molecular weight and increases in scale height. These changes to the mass mixing ratio will lead to changes in the model's thermosphere mass density and its response to geomagnetic activity.

The mass mixing ratio, ψ, in TIEGCM without He is expressed as,

$$\Psi_{N2} = 1 - \Psi_{O2} - \Psi_{O} \qquad Eq\ (4.1)$$

The mass mixing ratio, ψ, in TIEGCM with He as:

$$\Psi_{N2} = 1 - \Psi_{O2} - \Psi_{O} - \Psi_{He} \qquad Eq\ (4.2)$$

In the He major species model, the continuity equation for the major species mass mixing ratio is:

www.manaraa.com

$$\frac{\partial \widetilde{\Psi}}{\partial t} = -e^{Z}\tau^{-1}\frac{\partial}{\partial Z}[\frac{\overline{m}}{m_{N2}}\left(\frac{T_{\infty}}{T}\right)^{0.25}\alpha^{-1}L\widetilde{\Psi}] + e^{Z}\frac{\partial}{\partial Z}\left[e^{-Z}K(Z)\left(\frac{\partial}{\partial Z}+\frac{1}{\overline{m}}\frac{\partial \overline{m}}{\partial Z}\right)\widetilde{\Psi}\right]$$
$$-\left(\vec{V}\bullet\nabla\widetilde{\Psi}+w\frac{\partial\widetilde{\Psi}}{\partial Z}\right)+\tilde{S}-\tilde{R} \qquad Eq(4.3)$$

[*Dickinson et al.,* 1984], where Ψ is the mass mixing ratio of each species, *t* is time, Z=ln(P_0/P) is the vertical coordinate with *P* as pressure and P_0 as the reference pressure(50 μpa), τ is the diffusion time scale, $\overline{m}$ is the mean molecular weight, m_i is the molecular weight of species i, *T* is temperature, *V* is the horizontal velocity, *w* is vertical motion, *K(Z)* is the eddy diffusion coefficient, the matrix α varies as the inverse of diffusive coefficients, the matrix operator *L* is diagonal, which defines diffusive equilibrium solutions through $L\Psi = 0$, *S* is the photodissociation source term, and *R* is the chemical recombination term.

The alpha matrix, in Equation 5.3 was expanded from a 2x2 matrix to a 3x3 matrix to include the thermal diffusion between He and other major species N_2, O_2, O. Also He was added to the calculation of geopotential altitude, density, mean molecular weight, specific heat, thermal conductivity and other relevant model parameters. The lower boundary condition of the He major model is constant He mass mixing ratio, and the upper boundary condition is a non-escaping flux. This upper boundary condition accounts for He following ballistic trajectories in a collision-less exosphere as approximated by *Hodges and Johnson* [1968] and *Hodges* [1973] with no net He escaping from the model domain [*Sutton*, private communication].

This chapter compares the difference in the results between TIEGCM without He and with He as a major species, which are referred to as TIEGCM w/ He and TIEGCM w/o He in the following analysis. The thermosphere parameters compared in this chapter are thermosphere

www.manaraa.com

mass density, temperature, O mass mixing ratio, thermosphere mean molecular weight, and He behavior.

The time period simulated in this chapter is from day 336 (December 01) to day 345 (December 10) of the year 2008 to match the observations analyzed in Chapters 2 and 3. The northern hemisphere is winter and the southern hemisphere is summer. The solar and geomagnetic conditions are illustrated in Figure 3.1c.

The TIEGCM has 29 constant pressure levels ranging from -7.0 to 7.0 with half a scale-height resolution in the vertical. The corresponding altitude is from approximately 97 km to about 500~700 km depending on the solar cycle. The relationship between the height and pressure level are:

$$Z = -7 + \int_{h_0}^{h} \frac{dh}{H_P} \; and \; h = h_0 + \int_{-7}^{Z} H_P \, dZ \qquad Eq\ (4.4)$$

where Z is the reduced height. In this model, ilev=1 corresponding to Z=-7.0 and ilev=29 corresponding to Z=7. H_P stands for the pressure scale height and h is the geopotential height which is ~97 km at the lower boundary (ilev=1, Z=-7.0). In the following section, the comparisons at two constant altitudes, 200 km and 400 km. and at two constant pressure surfaces, pressure level 15 (ilev15) and pressure level 26 (ilev26), which correspond roughly to 200 km and 400 km, respectively, will be illustrated.

4.3 Analysis and Results

4.3.1 Change in Thermosphere parameters of TIEGCM at fixed altitudes

www.manaraa.com

Figure 4.1a-d shows the latitude and UT time variations of mass density, temperature, O mass mixing ratio and the mean molecular weight from TIEGCM w/o He at 200 km in the top panels. The Figure 4.1e-h displays the same parameters as Figure 4.1a-d from the TIEGCM w/ He modeling. The comparison between these two models suggests there is no change in the latitude structure at 200 km due to the implementation of He because He is very minor compared to O and N_2 at 200 km.

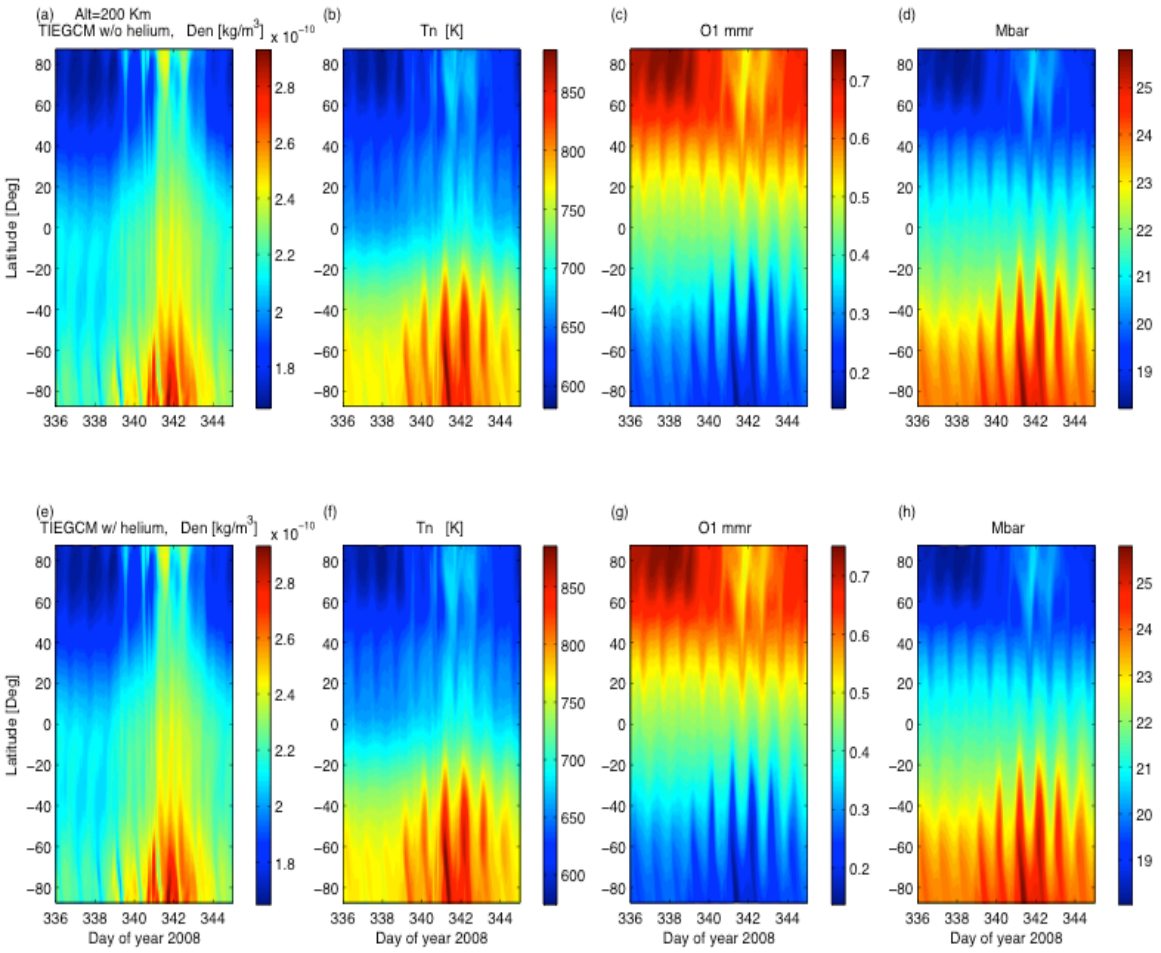

Figure 4.1. Top panels from left to right are the latitudinal and UT variations of the TIEGCM w/o helium results of thermosphere mass density (kg/m^3), neutral temperature (K), mass mixing ratio of atomic oxygen and thermosphere mean molecular weight at 200 km, fixed 09 SLT. The bottom panels are similar to the top but are the results of TIEGCM w/ helium module.

www.manaraa.com

Figure 4.2 shows the percent changes in the thermosphere parameters at 200 km after adding He. The percent changes in this plot is calculated by (TIEGCM w/ He / TIEGCM w/o He -1)*100. As illustrated in Figure 4.2, the changes in these thermosphere parameters are less than 2% at 200 km. The decrease in the temperature in Figure 4.2b could be due to the increase of the specific heat and the molecular thermal conductivity after adding He [*Kim et al.,* 2012]. The reduction in the mean molecular weight in Figure 4.2d is due to the winter helium bulge and therefore a decrease in the O mass mixing ratio.

The change in mass density at the fixed altitude is proportional to the integral of all the changes in mass density scale height below this altitude as demonstrated in Chapter 3. The mass density scale height change is approximately equal to the change in pressure scale height below 200 km, which is proportional to the changes in the ratio of temperature to the mean molecular weight. The change in temperature is larger than the change in the mean molecular weight at 200 km and below, which makes the density variation pattern similar to the temperature change in Figure 4.2.

Figure 4.3 displays the same results as Figure 4.1, but at 400 km. Figure 4.3a-d are results of TIEGCM w/o He and Figure 4.3e-h are of TIEGCM w/ He. As shown in this figure, the latitude patterns of the thermosphere mass density and temperature are higher in the summer hemisphere and lower density in the winter hemisphere for TIEGCM w/ and w/o He. The atomic O mass mixing ratio is lower in the winter hemisphere than in the summer hemisphere in TIEGCM w/ He, however it is lower in the summer than in the winter in TIEGCM w/o He. The atomic O mass mixing ratio in Figure 4.3c reduces from nearly 100% to less than 70% in Figure 4.3g when

www.manaraa.com

the amount of He becomes significant during the quiet time period of the winter hemisphere at 400 km. Note that the changes

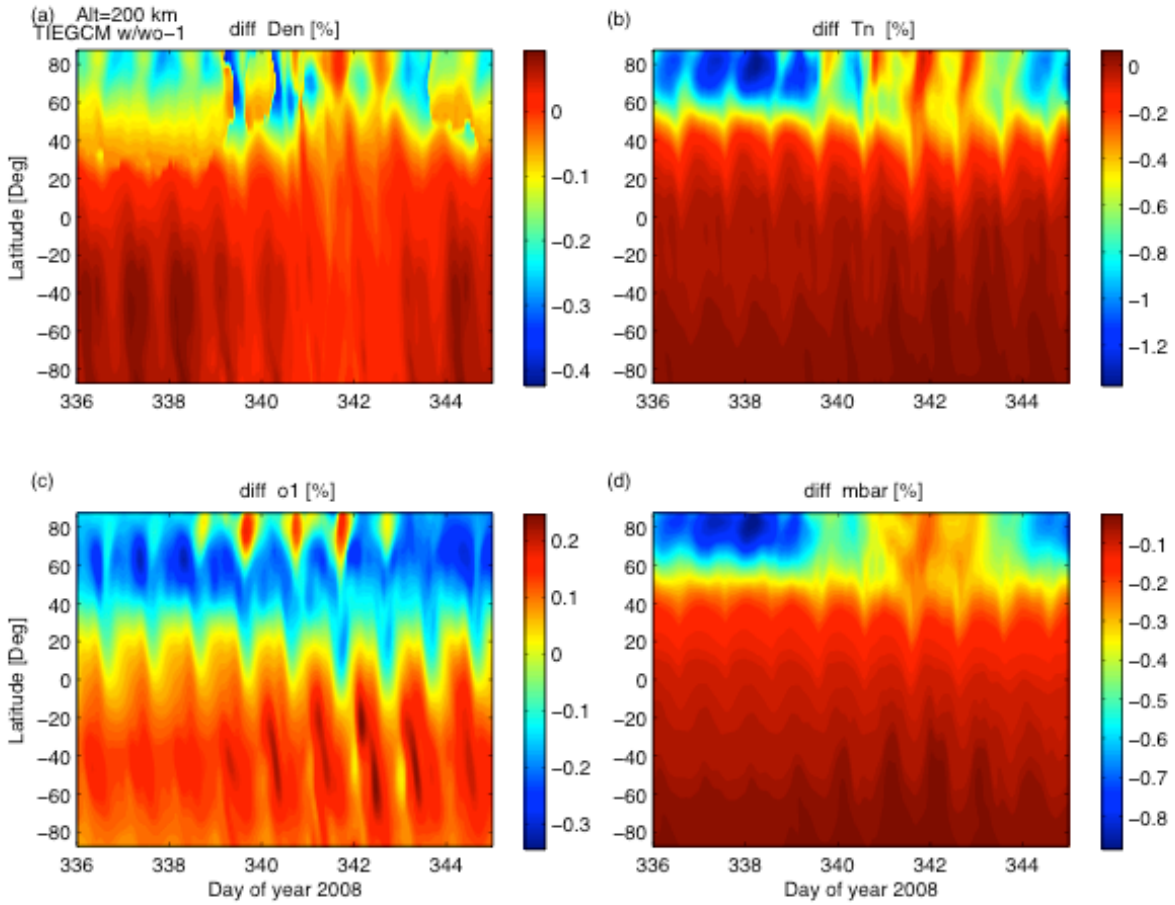

Figure 4.2. The latitudinal and UT variations of the percent difference of TIEGCM after implementing the helium module in thermosphere mass density (Den), temperature (Tn), atomic oxygen mass mixing ratio (o1) and mean molecular weight (mbar) at 200 km, fixed 09 SLT.

in O during the storm time period and in the summer hemisphere are quite small. The mean molecular weight in Figure 4.3d drops from about 16 in TIEGCM w/o He to less than 10 in TIEGCM w/ He in Figure 4.3h due to the ratio of O and He decrease in the quiet time winter hemisphere.

www.manaraa.com

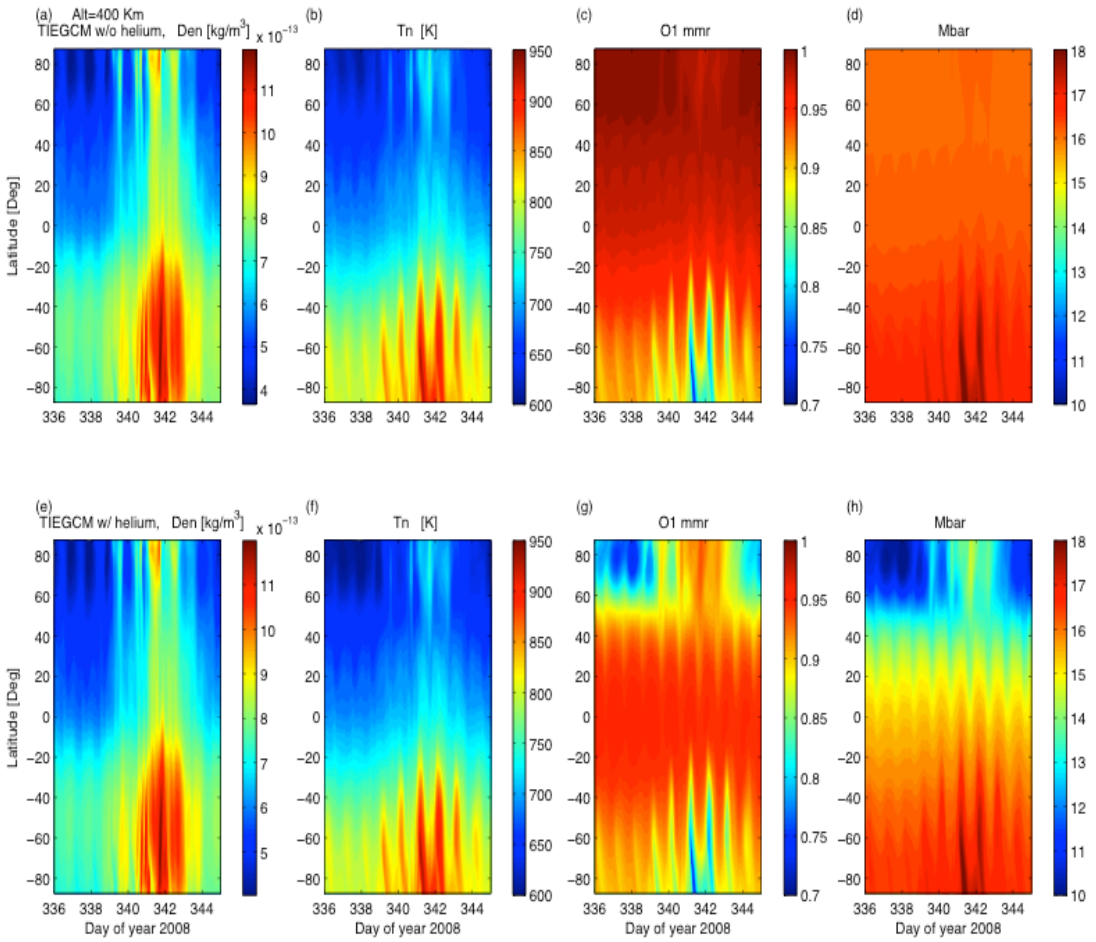

Figure 4.3. Similar to the Figure 4.1, but at 400km

Figure 4.4 provides plots of percent difference for the TIEGCM properties displayed in Figure 4.3. The changes in mass density that were negative at 200 km in Figure 4.3a are now positive at 400 km as illustrated in Figure 4.4a. The change in mass density is inversely proportional to the change in the ratio of temperature to the mean molecular weight. Unlike the case at 200 km, the change in mean molecular weight is much larger than that in temperature at 400 km. There is about a 2.5% decrease in the temperature in Figure 4.4b and a 35% decrease in the mean molecular weight in Figure 4.4d with He included. This makes the mass density scale height much larger after adding He, which makes the mass density increase about 10% during

www.manaraa.com

the quiet time period in the winter hemisphere at 400 km. Note that during the geomagnetically active times and in the summer hemisphere, the effects of adding He to the model have little affect on the temperature, mean molecular weight and density because O is the dominant species at this altitude.

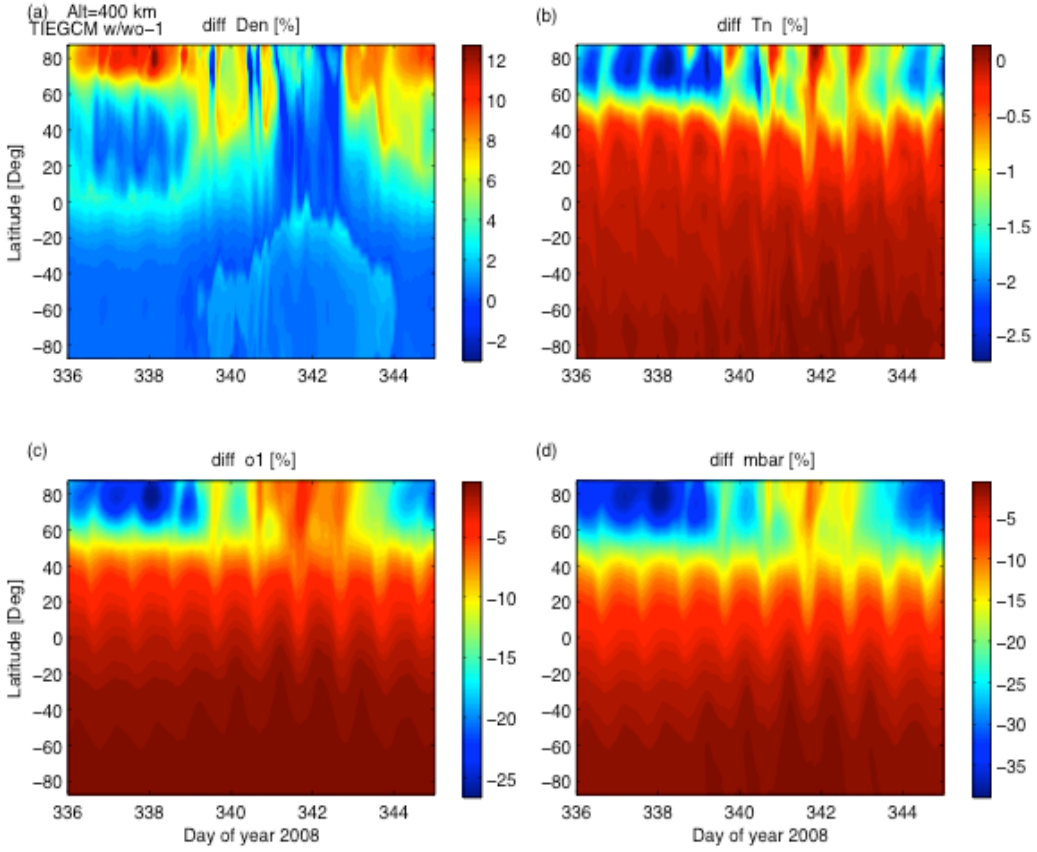

Figure 4.4. Similar to the Figure 4.2, but at 400 km.

4.3.2 Changes in altitude profiles of thermosphere parameters in TIEGCM

The section 4.3.1 illustrated the changes in TIEGCM at two fixed altitudes. To reveal the changes in the model fields with altitude, Figure 4.5a-c shows the altitude profiles of mass density, temperature and mean molecular weight at 09 local solar time, 12 universal time and

www.manaraa.com

72.5° N in the winter hemisphere. The TIEGCM without He results are in blue and with He are in red. Figure 4.5d-f are the corresponding percent differences calculated by (with He/ without He)-1. Figure 4.5a shows the logarithm of thermosphere mass density. The difference in mass density with He vs. without is shown in Figure 4.5d and is negative below 350 km and positive above 400 km. The explanation is that the temperature decrease is larger than the mean molecular weight decrease below 350 km, while the decrease in mean molecular weight is larger than the decrease in temperature above 400 km as compared in Figure 4.5e with 4.5f.

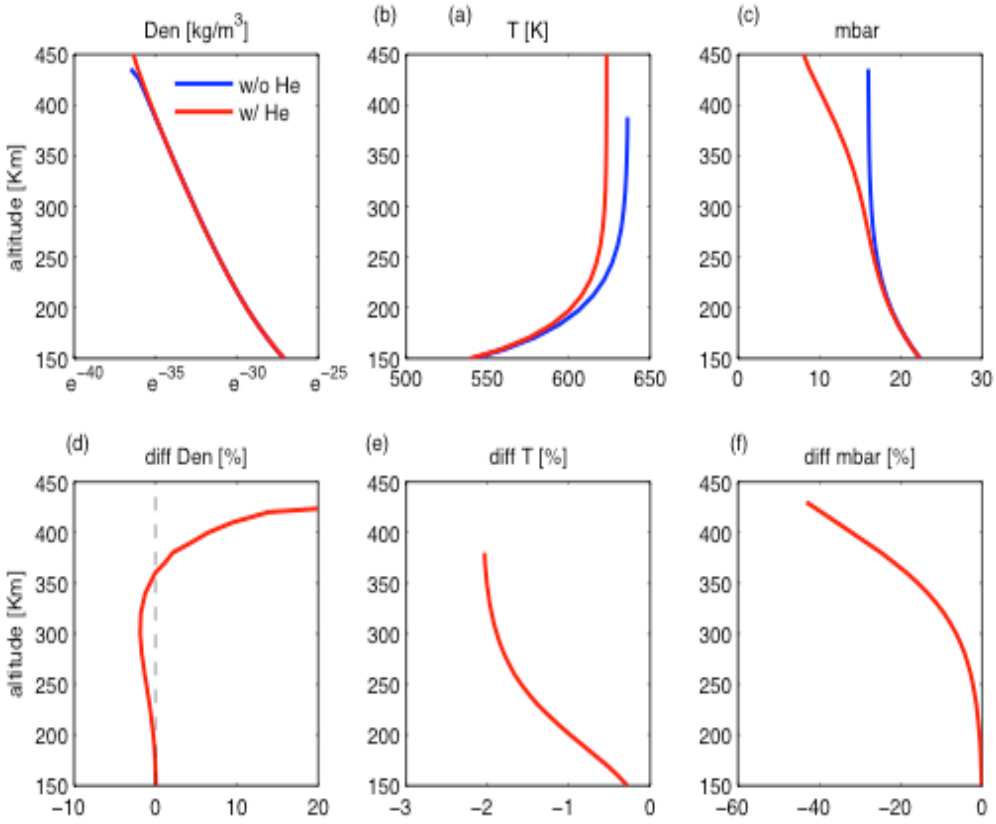

Figure 4.5. Altitude variations of dairy mean mass density (unit: kg/m^3), temperature (unit: K) and atomic oxygen mass mixing ratio from left to right panel. The tops are the absolute values from the modeling without helium in blue and modeling with helium in red. The bottoms are the relative values calculated by (without/with-1)*100. The simulation is for day 336th of 2008 at fixed 09 SLT.

www.manaraa.com

4.3.3 Changes in thermosphere parameters of TIEGCM at fixed pressure level

The analysis of the mass densities from satellite observations is in general on fixed altitudes, however, the results of the TIEGCM model are simulated on pressure levels because it is more convenient to calculate the model fields in fixed pressure levels than in fixed altitudes.

The changes at both the pressure level 15 (ilev15) and the pressure level 26 (ilev26) are studied in this section. The reason for choosing these two pressure levels is that their mean are near 200 km and 400 km, respectively. This allows a cross comparison between fixed altitude and fixed pressure altitude. What is more important is that the He concentration is small at ilev15 and significant at ilev26, thus by comparing the simulation results between ilev15 and ilev26, the impact of He can be illustrated.

As illustrated in Figure 4.6, the mass density, temperature, O mass mixing ratio and mean molecular weight from these two models at ilev15 are very similar in both the magnitude and the latitude structure. The mass density is higher in the winter than in the summer at fixed pressure level in Figure 4.6a,e. By comparison the mass density is higher in the summer than in the winter at fixed altitude in Figure 4.1a,e. The scale height is smaller in the winter than that in the summer at ilev15, thus the geopotential altitude corresponding to ilev15 is at lower altitude; hence the mass density is higher in the winter than in the summer.

Both the temperature and the mean molecular weight are higher in the summer than in the winter as illustrated in Figure 4.6b,f and Figure 4.6d,h. The atomic O mass mixing ratio is higher in the winter than that in the summer in Figure 4.6c,g due to the summer being occupied by N_2, as suggested by the mean molecular weight plot in Figure 4.6d,h.

www.manaraa.com

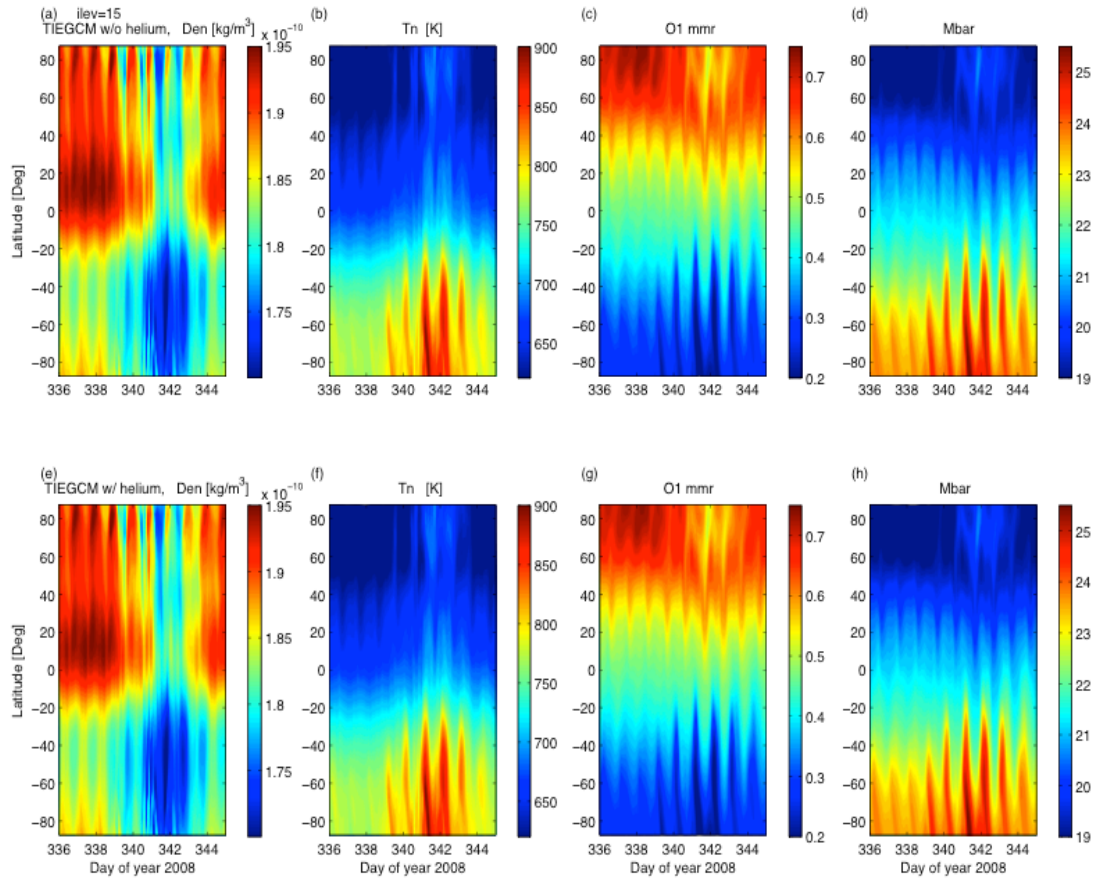

Figure 4.6. Top panels from left to right are the latitudinal and UT variations of the TIEGCM w/o helium modeling results of thermosphere mass density (kg/m^3), neutral temperature (K), mass mixing ratio of atomic oxygen and thermosphere mean molecular weight at fixed pressure level 15, 09 local time. The bottom panels are similar to the top panels but are the results of TIEGCM w/ helium module.

Figure 4.7 illustrates a plot similar to Figure 4.6 but at ilev26. Figure 4.7a suggests the mass density is higher in the winter hemisphere than in summer because the geopotential altitude for ilev26 is lower in the winter than in the summer when He is not included. However, Figure 4.7e shows a lower density in the winter hemisphere than in the summer because the geopotential altitude for ilev26 is higher in the winter than in the summer when including He in the TIEGCM. The latitude pattern of the mass density has significant changes after adding He at this pressure level.

www.manaraa.com

The temperature in both models are higher in summer than in winter as shown in Figure 4.7b,f. The O mass mixing ratio and mean molecular weight decrease substantially in the winter hemisphere because a large amount of He appears in the winter at ilev26 in TIEGCM w/ He. Without He the O concentration is near 100%, and the mean molecular weight is about 16. The inclusion of He decreases mean molecular weight to near 10 at ilev26.

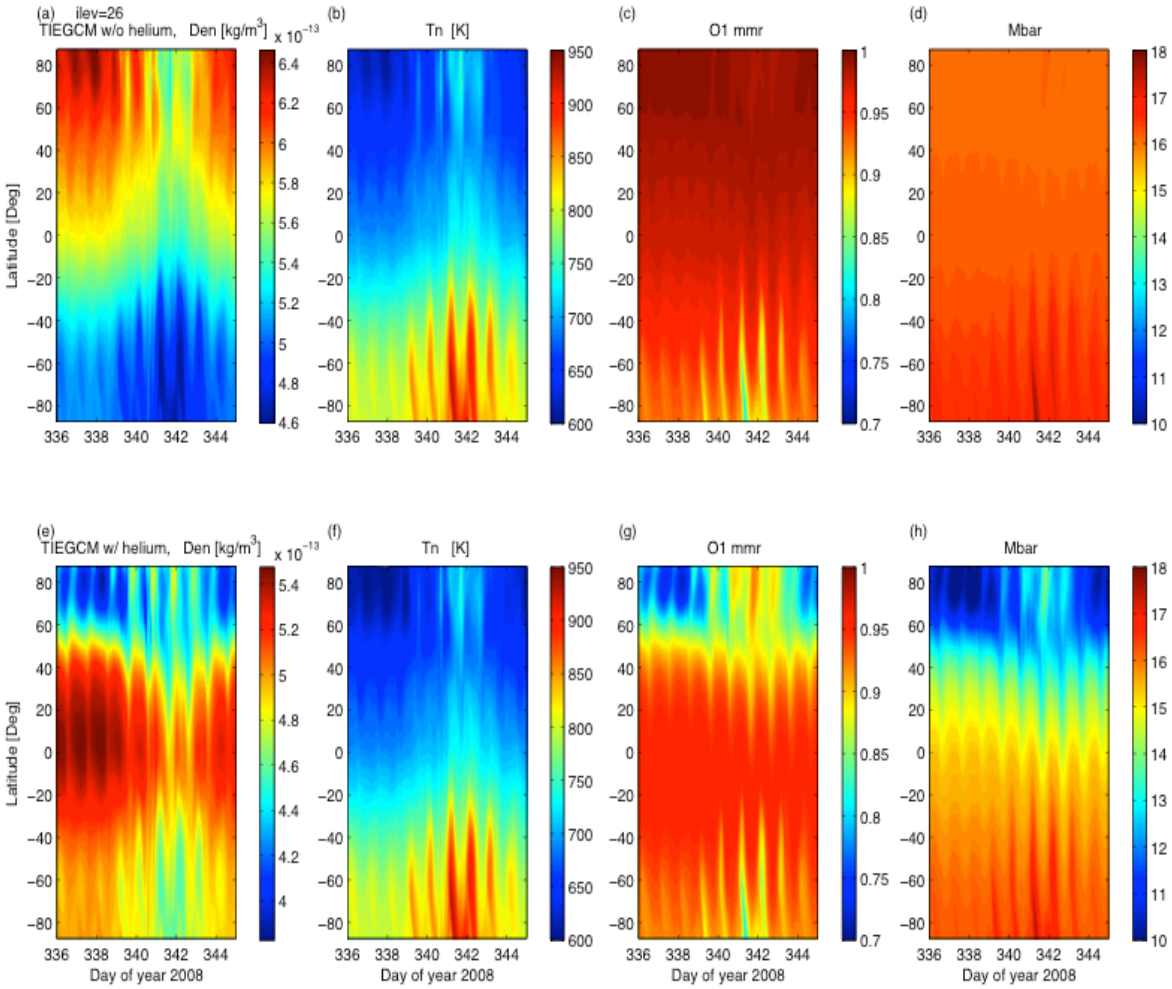

Figure 4.7. Similar to Figure 4.6, but at fixed pressure level 26.

According to the ideal gas law $P = nkT \quad and \quad \rho = n\bar{m} * amu$, with P being the pressure, n the number density, k the Boltzmann constant, T the neutral temperature, ρ the mass density,

www.manaraa.com

$\bar{m}$ the mean molecular weight and *amu* is the atomic mass unit (1.67x10^{-27} kg). The function between the atmosphere pressure, density, temperature and mean molecular weight is

$$\frac{\rho'}{\rho} = \frac{P'}{P}\frac{T}{T'}\frac{\bar{m}'}{\bar{m}} \qquad Eq\ (4.5)$$

where $P, \rho, T, \bar{m}$ are the model fields of TIEGCM w/o He and $P', \rho', T', \bar{m}'$ are the model fields of TIEGCM w/ He. The changes in the mass density at fixed pressure level are inversely proportional to the changes in temperature and proportional to changes in the mean molecular weight according to Equation 5.5. The density variations at fixed pressure level is determined by whether the change in the temperature overcomes the mean molecular weight or the other way around.

Figure 4.8, illustrates the changes in thermosphere parameters after adding He, as a function of latitude and time at ilev15 and ilev26, respectively. The percent differences of these parameters $(\frac{\rho'}{\rho}-1, \frac{\bar{m}'}{\bar{m}}-1, \frac{T'}{T}-1)$ x100 are within ±1% at ilev15. Note that at a fixed pressure level, $\frac{\rho'}{\rho} = \frac{\bar{m}'}{\bar{m}} / \frac{T'}{T}$ according to equation 5.5. The corresponding mass density difference is positive in the winter quiet time at ilev15 because the difference in temperature is larger than that in the mean molecular weight.

For the lower pressure at ilev26, the impacts of adding He in the model on the thermosphere parameters are more significant. The changes of thermosphere parameters are larger in the winter than in the summer, and larger during the quiet time than during the active period. In the winter there is nearly a 40% decrease in mean molecular weight and a 2.5% decrease in temperature. As

www.manaraa.com

a result, the mass density reduced by about 35% in the winter quiet time.

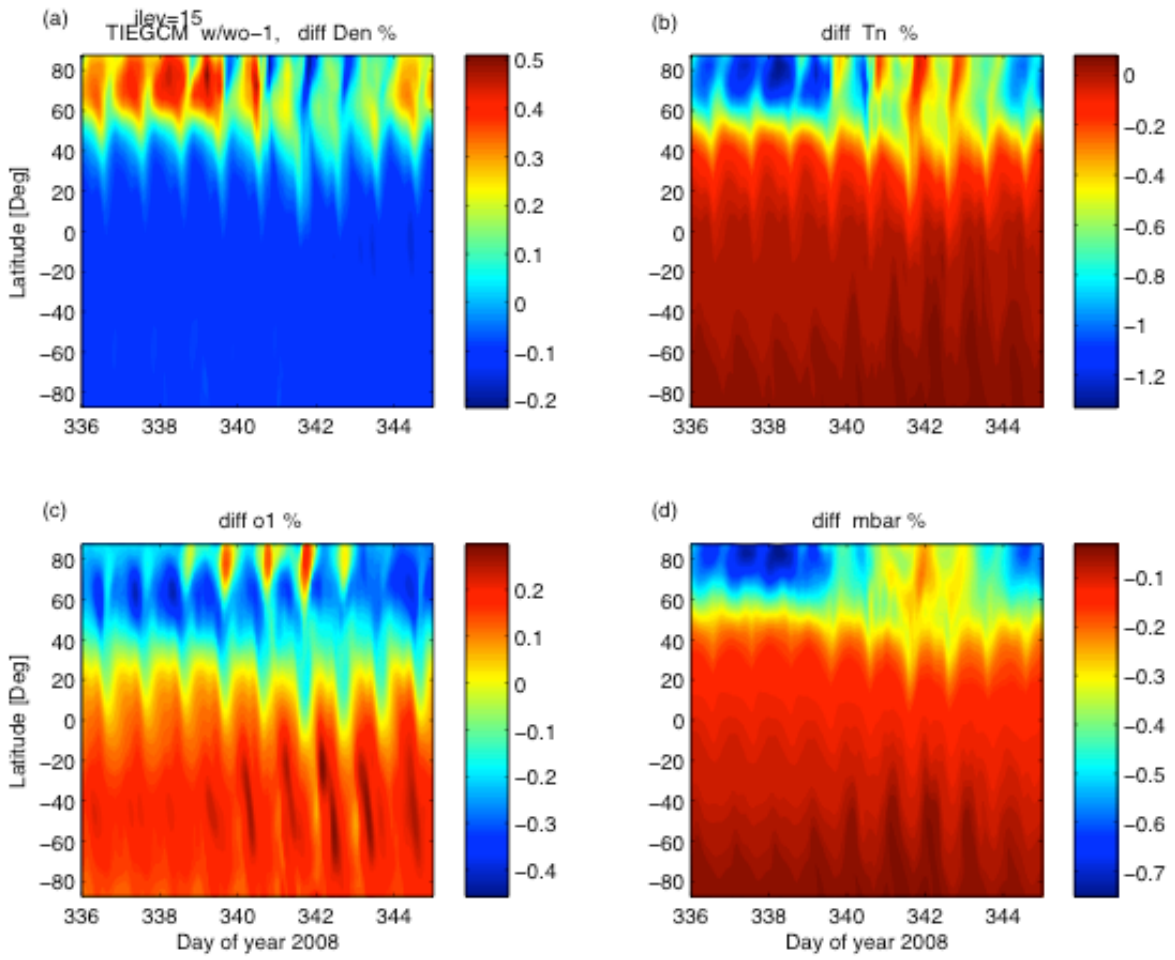

Figure 4.8. The latitudinal and UT variations of the percent difference [%] of TIEGCM after implementing the helium module in thermosphere mass density (top left), temperature (top right), atomic oxygen mass mixing ratio (bottom left) and mean molecular weight (bottom right) at fixed pressure level 15, fixed 09 SLT.

www.manaraa.com

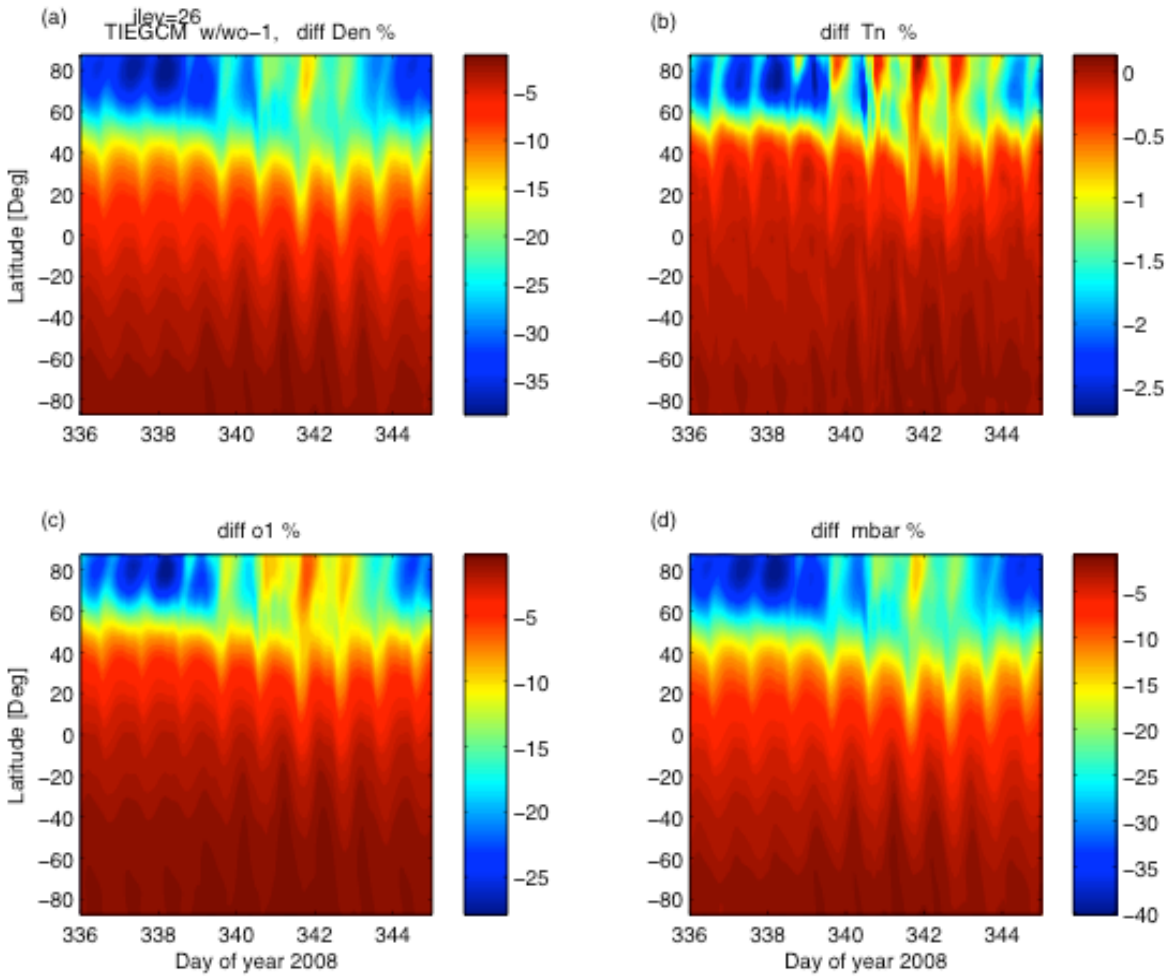

Figure 4.9. Similar to the Figure 4.8, but at fixed pressure level 26.

4.4 Test of helium in TIEGCM

The implementation of He in the TIEGCM as a major species makes the model more complete and better represents the physics. This is the first time that the He morphology in the model is being tested. This section illustrates the model's ability to reproduce the He perturbation during storm time in TIEGCM w/ He and compared to the He derived data from the satellite observations presented in Chapter 3. This section also reproduces the altitude profile of the mass density perturbation and tests the He modifying effect on the mass density response

www.manaraa.com

investigated in Chapter 3.

Figure 4.10 shows the comparison of the He and O number densities from the extracted data of satellite measurements, TIEGCM w/ He modeling, and NRL-MSISE00 simulation at 450 km. Figure 4.10a,b demonstrate the latitudinal and time variations of extracted He and O number densities from CHAMP and GRACE measurements at 450 km. Figure 4.10c, d display similar figures but from TIEGCM w/He modeling. Figure 4.10e,f display similar properties from NRL-MSISE00 simulations. Note that the contour plots of these three different sources are displayed using the same color scale. There is clearly a winter helium bulge in the TIEGCM w/ He output. The composition perturbations during storm time suggest the depletion in He and enhancement of O number densities. These latitude patterns and storm time variation patterns are consistent with the CHAMP and GRACE satellite observations and empirical model simulation of MSISE00. Note the magnitude of the He number density from TIEGCM w/ He modeling is closer to the He data inferred from CHAMP and GRACE observation. The He concentration from the MSISE00 is lower than the observations and TIEGCM w/He model, which is consistent with the conclusion in Chapter 2 that the MSISE00 underestimates the He by 30-70% during the extreme solar minimum in 2008.

This section reproduces the altitude profiles of the mass density perturbation in Figure 3.4 using the TIEGCM model w/He instead of the adjusted MSISE00 model. Figure 4.11a is the result of TIEGCM w/He and Figure 4.11b is the result of TIEGCM w/o He. The difference in the upper boundary altitude between the two plots is due to the difference in geopotential height when including He.

www.manaraa.com

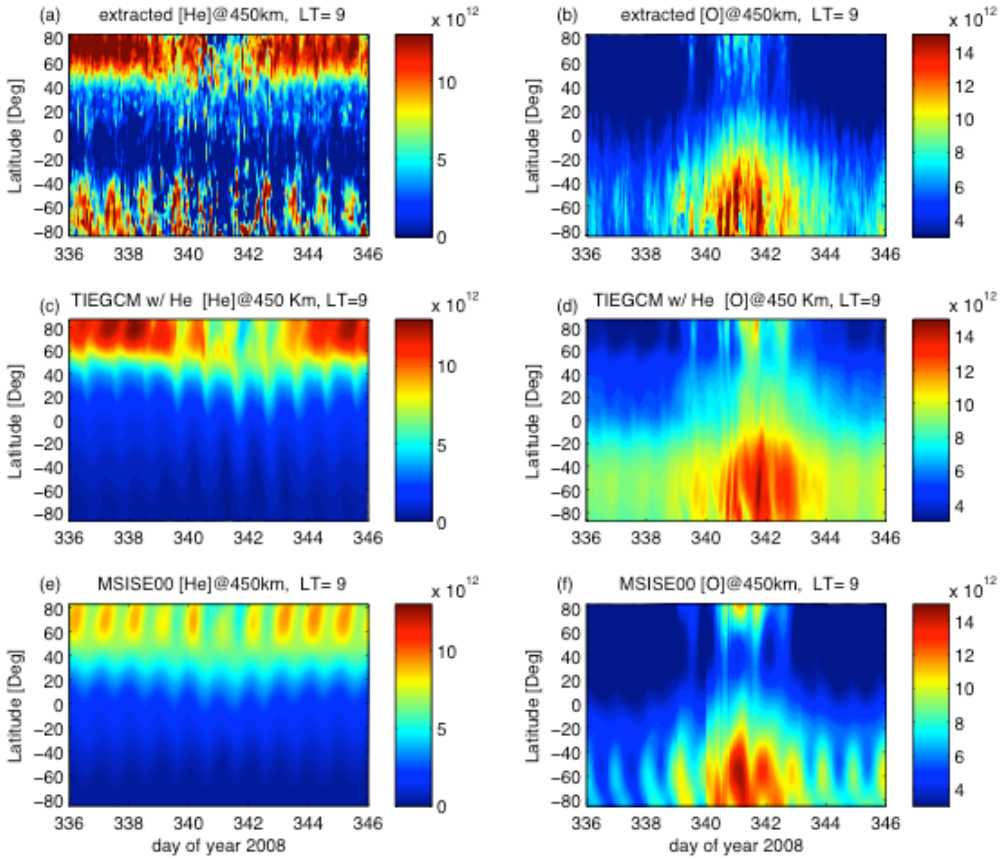

Figure 4.10. Latitudinal and UT variation of (a) helium and (b) oxygen number density at 450 km estimated from CHAMP and GRACE satellite measurements; (c) The helium and (d) oxygen number density from TIEGCM w/ helium at 450 km. (e) The helium and (f) oxygen number density from adjusted MSIS estimation at 450 km at fixed 09 SLT. The unit for the number density is [m^{-3}].

The result in Figure 4.11a is consistent with the theory in Chapter 3 and further validates the He implementation including the He flux boundary condition implemented at the top of the model. The density perturbations first increase with altitude and reach a maximum around the O/He transition region around 400 km in the winter hemisphere as shown in Figure 4.11a, illustrating the model captures the modifying influence of O/He composition change on mass

www.manaraa.com

density response. The modifying effect of the N_2/O transition region on the mass density response can be distinguished around 200-300 km in the summer hemisphere. The TIEGCM w/ He simulation in Figure 4.11a is consistent with the adjusted MSISE00 result in Figure 3.4. In the TIEGCM w/o He model, the composition effect in N_2/O is also much weaker as shown in Figure 4.11b and the mass density response to geomagnetic activity continues to increase with altitude.

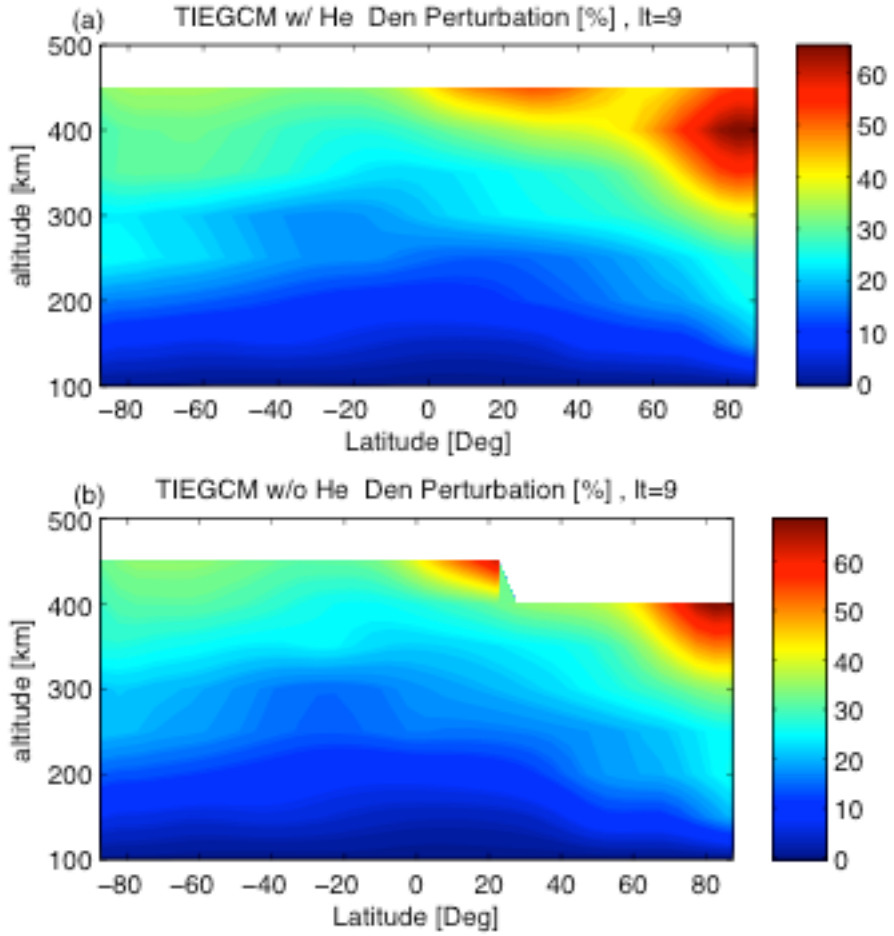

Figure 4.11. (a) Altitudinal and latitudinal variations of the mass density perturbation in percent change (%) during the day 340-341 (Dec 05-06) of 2008 geomagnetic storm from TIEGCM w/ helium, (b) Same as (a), but the result from TIEGCM w/o helium.

www.manaraa.com

4.5 Discussion and Conclusions

The incorporation of He into the TIEGCM as a major species is a self-consistent process that shows consistency with observations. There are two possible mechanisms that change the thermosphere parameters after adding He. In the first mechanism, the thermosphere temperature and the mass mixing ratios of other major constituents N_2, O_2 and O readjust correspondingly to the He implementation. The changes in mass density scale height associated with the changes in the ratio of temperature to mean molecular weight alter the value of the thermosphere mass density and even its latitude structure when the He concentration is significant. This is particularly evident during this recent extreme solar minimum. In the second mechanism, the implementation of He in the TIEGCM increases the specific heat, thermal conductivity and molecular viscosity [*Kim et al.,* 2012], and consequently changes the thermodynamic properties. Considering the above two mechanisms, the effect of the changes in mass density scale height is responsible for most of the differences in thermosphere parameters [*Eric Sutton*, private communication].

The He concentrations are very minor at low altitudes and high pressure levels, hence the effect of adding He on the mass density are negligible, and the density change are within ± 1%, primarily due to temperature changes. The He concentration increases significantly when going towards the higher altitudes and lower pressure levels, causing the changes in mean molecular weight and mass density to be significant. This is especially evident in the winter hemisphere where the winter helium bulge appears, the change in mass density could be up to 35%.

www.manaraa.com

The change in mass density at fixed altitude is determined by the integration of all the scale heights change below this altitude. The altitude profile of the mass density change illustrates negative changes at low altitudes because the change is larger in temperature than in mean molecular weight (Figure 4.5d). The mass density change is positive in high altitudes because the change is larger in mean molecular weight than in temperature due to a large amount of He existing at high altitudes.

At the fixed pressure level, the mass density change is proportional to the change in mean molecular weight and inverse proportional to the change in temperature. At the pressure level 26, the latitude pattern of the mass density from TIEGCM w/o He suggests higher density in the summer than in the winter (Figure 4.7e). This latitude structure reverses to higher density in the winter than in the summer after implementing He (Figure 4.7a), which causes a significant change in the mass density of about 35%.

www.manaraa.com

Chapter 5 A Revisit of the Winter Helium Bulge Formation

Through the test of the He morphology in the TIEGCM model in Chapter 4, it is clear the TIEGCM w/ He model could be used to study the He behavior, particularly the wintertime helium bulge. However, the benefit of completely integrating He as a major gas makes diagnosing its behavior in the model complex. Consequently another He module was implemented assuming He behaves as a minor gas throughout the thermosphere. Although not as complete as treating it as a major gas, it does allow for the behavior of He to be evaluated when it is a minor gas. Also, the two types of implementation can be compared to evaluate any significant differences.

In the He minor species model, the He distribution is affected by the major species such as N_2, O_2 and O, however the changes in He do not impact the major species. This form of the implementation enables individual terms in the He minor species equation to be evaluated to determine which terms contribute to the helium bulge formation. In addition, the evaluation is conducted at altitudes less than 400 km in this chapter, thus the assumption of He as a minor species in the model is reasonable.

The TIEGCM w/ He minor model is used to revisit the mechanism responsible for the winter helium bulge formation. Both the effects of horizontal transport between hemispheres and vertical advection are examined to investigate the formation of the helium bulge in the model. The TIEGCM modeling result suggests that vertical wind structure and molecular diffusion are

www.manaraa.com

the main sources for the winter helium bulge formation. The altitude distribution of the He number density departs from diffusive equilibrium due to local vertical winds. Downward winds in the winter hemisphere enhance the He concentration while upward winds in the summer hemisphere depress the He concentration at an altitude where He is a minor species. The horizontal transport between hemispheres, pushes the peak location of the helium bulge poleward, however it is a minor effect to the formation of the winter helium bulge.

5.1 Introduction

The winter helium bulge, a 1~2 orders higher He concentration in winter hemisphere than in the summer hemisphere, was first discovered by *Keating and Prior* [1968] and *Reber et al* [1968] from satellite drag measurements. Later studies confirmed the existence of the winter helium bulge by directly measuring He concentrations using satellite-borne mass spectrometers [*Reber et al.,* 1971; *von Zahn,* 1975; *Mauersberger et al.,* 1976a, 1976b]. The winter helium bulge has been used to explain anomalous behavior in mass density inferred from satellite drag measurements [*Keating and Prior,* 1968; *Jacchia,* 1968; *Bruinsma and Forbes*, 2010; *Thayer et al*., 2012].

The observational features of the winter helium bulge have been well studied in the 1970s when there were sufficient *in situ* measurements of He number density by satellites. The peak of the winter helium bulge is located near the geomagnetic pole [*Reber and Hays*, 1973]. The local time, seasonal and altitude variations of He concentration were reported by *Cageao and Kerr* [1984] using the AE-C satellite measurements. Although lacking a coupled general circulation

www.manaraa.com

upper atmosphere model in the 70's, the possible physical processes of the formation of the winter helium bulge had been related to 1) the change in eddy mixing and the associated turbopause altitude variations in the lower thermosphere, 2) the thermosphere wind systems and the lateral transport in the exosphere [Kockarts and Nicolet, 1962; Reber and Nicolet, 1965; McAfee, 1967; Hartmann et al., 1968; Hodges and Johnson, 1968, Johnson and Gottllieb, 1969, 1970; Reber et al., 1971, 1973; Kockarts, 1972; Mayr et al., 1978]. Among these, the most frequently mentioned mechanism for the winter helium bulge formation has been associated with the thermosphere wind effect.

The wind in the earth thermosphere system in solstice is directed from the summer to winter hemisphere due to the higher temperature and associated higher pressure levels in summer. This large-scale meridional flow from summer to winter implies upward vertical winds in the summer hemisphere and downward vertical winds in the winter hemisphere according to the mass continuity equation. *Johnson and Gottlieb* [1969, 1970] suggested the winter helium bulge is due to the large-scale meridional circulation system moving He from summer pole to winter pole. *Mayr et al.* [1978] and *Cageao and Kerr* [1984] explained the formation of the winter helium bulge as: "more helium is transported by horizontal advection to the winter pole than is returned to the summer pole by the lateral transport due to the large scale height of helium. In addition, the vertical diffusion barrier becomes affected as N_2 density increase toward lower altitude, preventing helium from diffusing downward over the winter hemisphere." Besides the large-scale horizontal transport, the effect of the vertical wind on the helium bulge formation is included in the study of *Reber and Hays* [1973], who reproduced the latitude distribution of He

www.manaraa.com

number density measurements by the OGO 6 satellite after combining the effects of both the horizontal transport across hemispheres and vertical winds. However, the study of *Reber and Hays* [1973] did not evaluate the horizontal advection affect and the vertical wind effect separately, and *Reber and Hays* [1973] included neither the temperature variation nor the major gas density variation with latitude.

The horizontal advection effect and the vertical wind effect on the winter helium bulge formation will be evaluated separately here for the first time since they were considered in the 1970s. It is warranted to revisit the winter bulge formation using the first principles, self-consistent TIEGCM after implementing a He module that treats He as a minor species.

5.2 TIEGCM Helium Minor vs. Helium Major

Figure 5.1 and Figure 5.2 shows the comparison of the He number density and vertical wind output between TIEGCM w/ He as a minor species and TIEGCM w/ He as a major species at 150km and 400km, using the same solar and geomagnetic conditions $F_{10.7}$=70 and K_p=2, respectively. The lower boundary conditions are the same for He minor and He major. The result in Figure 5.1 suggests that the latitude pattern of He number density is consistent in the He minor species module compared to the He major species module. The magnitude of He number densities from the He minor species module is similar from the He major species module, which are 10^{13} m^{-3} in 150 km and 10^{12} m^{-3} in 400km. The absolute values are slightly larger from the minor He module than in the major He module and its explanation needs further investigation.

www.manaraa.com

The vertical wind patterns and values from the He minor species module is exactly the same as the He major species module as illustrated in Figure 5.2.

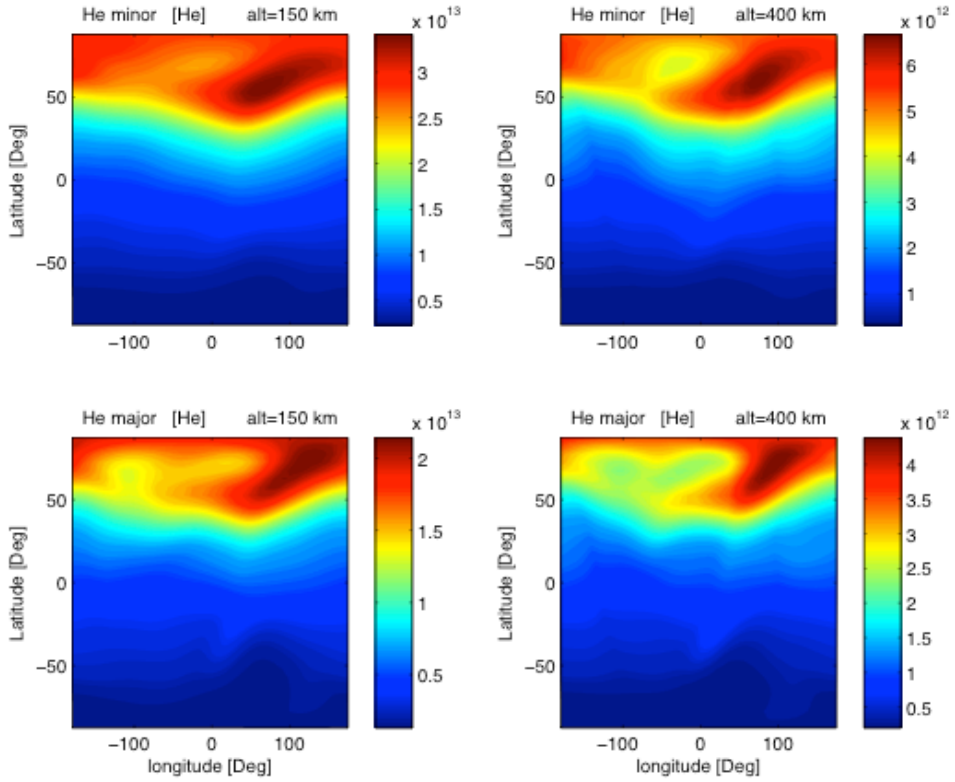

Figure 5.1. The latitudinal and longitudinal variations of the helium number density [m^{-3}] by TIEGCM w/ helium as minor species (Top) and w/helium as major species (Bottom) in day 326 of year 2008. The left are the results at 150 km and the right are the results at 400 km. Fixed $F_{10.7}$=70 sfu, K_p=2, UT=4. The upper boundary flux for the helium module is zero flux.

www.manaraa.com

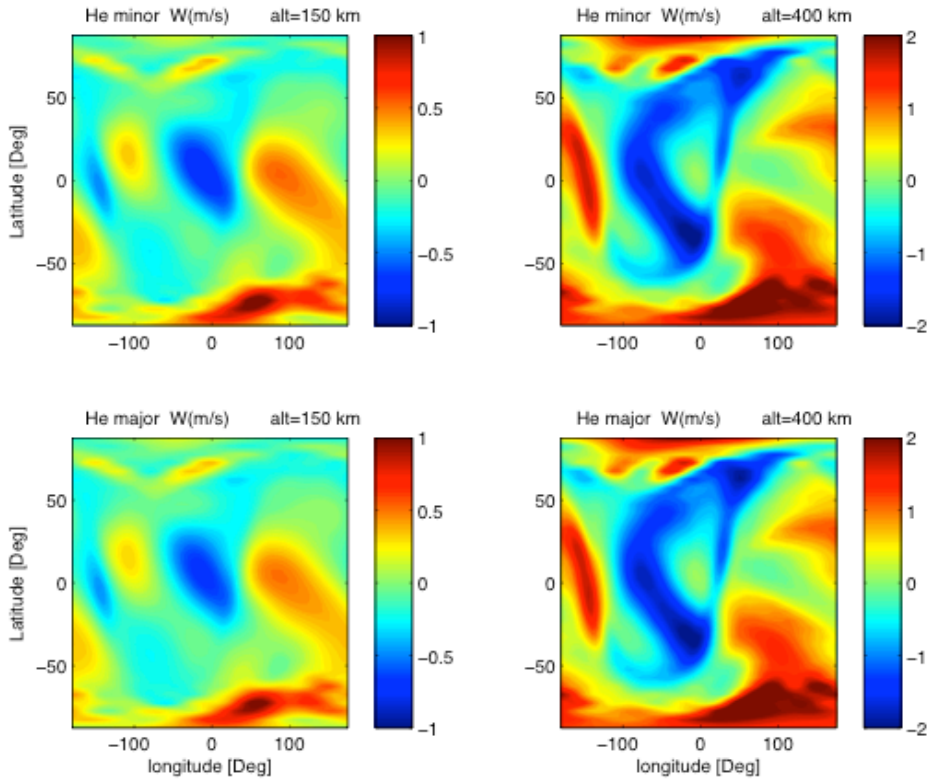

Figure 5.2. Similar to Figure 5.1, but the plots of the vertical wind.

5.3 TIEGCM Helium Minor Numerical experiments

The He minor species equation has been implemented into the TIEGCM model and coupled with the other major gas equations. Because He is an inert gas, the neutral wind transport effect needs only to be considered. According to *Roble et al.* [1988], the continuity function of He in the TIEGCM is written as:

$$\frac{\partial \widetilde{\Psi}}{\partial t} = -e^{Z}\frac{\partial}{\partial Z}[\widetilde{A}\left(\frac{\partial}{\partial Z}-\widetilde{E}\right)\widetilde{\Psi}]+\widetilde{S}-\widetilde{R}-\left(\vec{V}\bullet\nabla\widetilde{\Psi}+w\frac{\partial\widetilde{\Psi}}{\partial Z}\right)+e^{Z}\left[e^{-Z}K_{E}(Z)\left(\frac{\partial}{\partial Z}+\frac{1}{\overline{m}}\frac{\partial\overline{m}}{\partial Z}\right)\widetilde{\Psi}\right]$$

where Ψ is the He mass mixing ratio. The vertical molecular diffusion coefficient is A, S is the production term, the loss term is R, the term E includes the effects of gravity, thermal diffusion

www.manaraa.com

and friction with the major species on the vertical profile of minor species. The first term on the right side of the equation is the vertical molecular diffusion term. The second and third terms are the production and the loss terms for He, which are negligible in the model because He is an inert gas; the fourth term is the horizontal and vertical nonlinear advection terms, which will be tested extensively in this study; and the last term on the right hand side is the vertical eddy diffusion term.

The simulations were conducted under low solar activity. The solar activity index $F_{10.7}$ is 70 sfu and K_p=2. The horizontal resolution of the TIEGCM model run is 5° latitudes by 5° longitudes and the vertical resolution is half a scale height. The time step is 120 seconds. The ionosphere convection is specified by the model of *Heelis et al.* [1982] and the migrating tides from the lower atmosphere are specified by the Global Scale Wave Model (GSWM) [*Hagan and Forbes*, 2002].

The altitude ranges of the TIEGCM in pressure levels are from -7 to 7 with increments of half a scale height. The initial state of the model run is zero He number density at all the altitudes from -7 to 7 pressure levels and constant mass mixing ratio, $0.209*10^{-5}$ at the -7.5 pressure level, which is half a pressure level below the bottom boundary. The purpose of setting the He number density to zero initially is to determine whether the TIEGCM model is capable of reproducing the formation of the winter helium bulge. We will carry out three TIEGCM simulations: the 1st simulation includes both the horizontal advection and the vertical wind effect in the minor species He module, the 2nd simulation turns off the horizontal advection, and the 3rd simulation

www.manaraa.com

turns off the vertical wind term. These three simulations are hereafter referred to as Run 1, Run 2 and Run 3.

The modeling was conducted under solstice conditions beginning from the 316th day of year. For all the following simulations of the TIEGCM and the NRL-MSISE00, the 316th day of year will be referred as day 1 and herein the 326th day of the year will be referred to as day 10.

5.4 Mechanism For Winter Helium Bulge

In order to verify the He output of the TIEGCM, the latitude profile of relative He number density from the model is compared with the output from the NRL-MSISE00 model. NRL-MSISE00 is empirical model based on in situ mass spectrometer measurement of He from several satellites in the 1970's [*Hendin,* 1983], such as OGO 6 [*Carignan and Pinkus*, 1968], AE satellites [*Spencer et al.,* 1973], ESRO [*Trinks and von Zahn,* 1975] etc. Figure 5.3 illustrates the relative He number density, which is the ratio of He number density to the mean over all latitudes, at 97, 150, 200, 300, 400 km in day 10. Figure 5.3a,b are the results of the TIEGCM run and Figure 5.3c are simulations from NRL-MSIS00 using the same solar condition input $F_{10.7}$=70, K_p=2 as TIEGCM. UT=4 and Lon=100°. The upper boundary condition of the simulation in Figure 5.3a is a global constant outward flux with a value of $2*10^8$ cm^{-2}s^{-1} [*Banks and Kockarts,* 1973] while a variable upper boundary flux, $\Phi_{He}(z) = -w(z) * n_{He}(z)$ [*Hays et al.,* 1973] is adopted in Figure 5.3b, where w is the vertical wind velocity and n_{He} is the He number density. Both TIEGCM simulations in Figure 5.3a and 5.3b are run with zero He number density at the initial state. Figure 5.3 illustrates that the winter helium bulge is reproduced in both the

www.manaraa.com

TIEGCM and the NRL-MSISE00 model with the relative He number density about 2.5 in the northern winter hemisphere and 0~0.5 in the southern summer hemisphere. The latitude patterns of the relative He number density from the TIEGCM are comparable with that from the MSIS simulation, which illustrates the capability of the TIEGCM He module to reproduce the winter helium bulge.

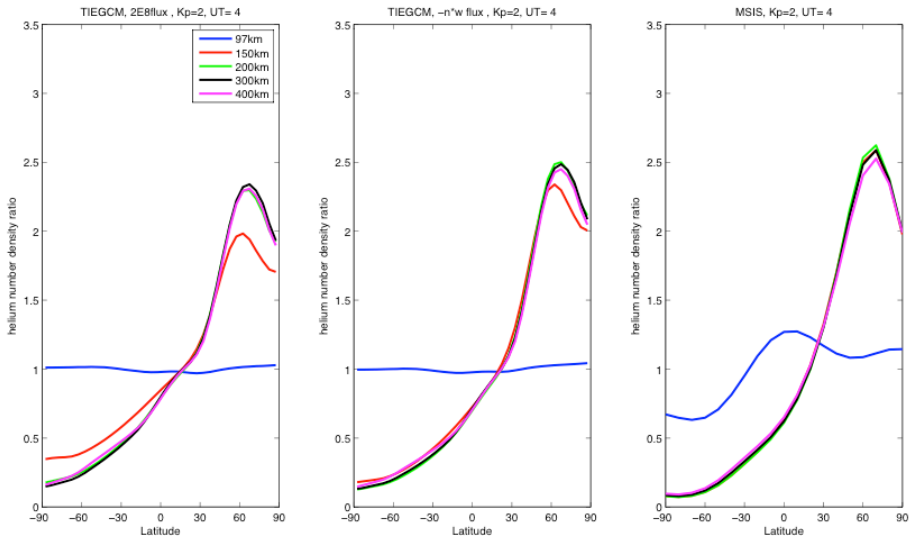

Figure 5.3. (a) Latitudinal variation of the relative helium number density to the latitudinal mean at 97 (blue), 150 (red), 200 (green), 300 (black) and 400 km (purple) by TIEGCM model in day 10. Fixed $F_{10.7}$=70 sfu, K_p=2, *UT*=4, *Lon*=100 degree. The upper boundary flux for the helium module is $2x10^8$ $cm^{-2}s^{-1}$. (b) Same as Figure 5.3a, but the upper boundary flux for the helium module is $-w(z)*n_{he}(z)$. where n_{he} is the helium number density and w is the vertical wind. (c) Same as Figure 5.3a, but from NRL-MSISE00 simulation with same solar condition.

The latitude variations of the relative He number density under constant and variable upper boundary fluxes in the TIEGCM, as shown in Figure 5.3a and 5.3b respectively, are consistent with each other but slightly different in magnitude, so the variable upper boundary flux $-w(z)*n_{He}(z)$ will be applied to the following TIEGCM model runs.

www.manaraa.com

One of the advantages of the TIEGCM model over the empirical NRL-MSIS00 model is that the TIEGCM can be used to explore the physical processes of the winter helium bulge formation. Figure 5.4 shows the latitude variations of the relative He number density from day 1 to day 10 of the TIEGCM model run with an initial state of zero He number density. Figure 5.4 illustrates

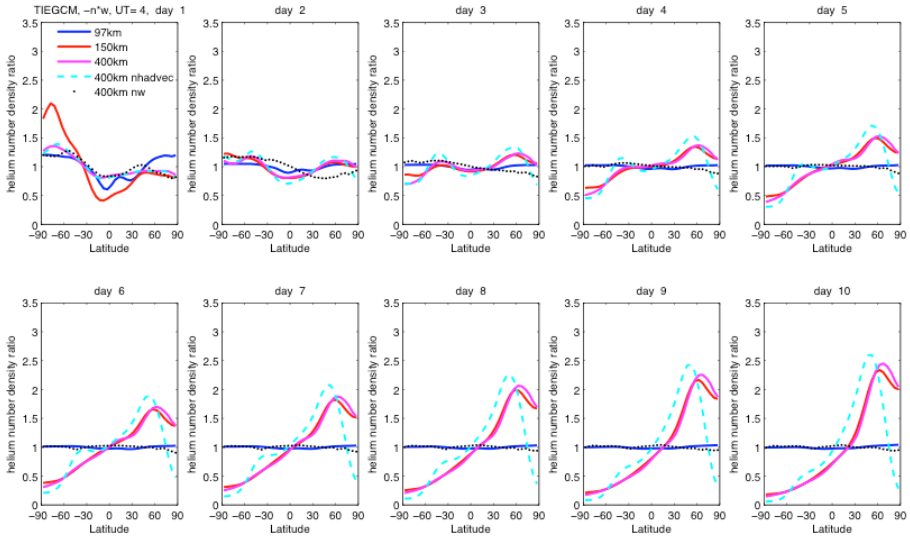

Figure 5.4. Latitudinal variation of relative helium number density to the latitudinal mean from day 1 to day 10 by TIEGCM, Fixed $F_{10.7}$=70 sfu, K_p=2, *UT*=4, *Lon*=100 degree. The upper boundary flux for the helium module is $-w(z)*n_{he}(z)$. The solid line represents the result of Run 1, the simulation includes both horizontal advection and vertical wind effects; the azure dash line shows the result of Run 2, the simulation with the horizontal advection off; the black dot line shows the result of Run 3, the simulation with the vertical wind effect off.

evolution of the winter helium bulge. The solid line represents Run 1, a simulation including both horizontal advection and vertical wind terms, at 97, 150 and 400 km. The azure dashed line represents the results from Run 2, a simulation without horizontal advection, at 400 km, and the dark dot line represents the results from Run 3, a simulation without the vertical wind term, at 400 km. Run 1 shows that the winter helium bulge is formed in day 3 and this bulge is growing with time towards day 10. Note that the winter helium bulge keeps increasing after day 10 until it

www.manaraa.com

reaches a steady state in day 20, however, only the results from day 1 to day 10 are displayed here because the purpose of these simulations is to address the basic mechanism for the formation of the winter helium bulge. Run 2, illustrated by the dashed line, shows that the winter helium bulge still occurs and the bulge keeps growing towards day 10 even though the horizontal transport of He from summer to winter is turned off. Run 2 suggests that the horizontal transport between hemispheres is not the mechanism for the winter helium bugle formation. Note that the horizontal advection changes the peak location of the helium bulge, pushing the peak location of the bulge toward the pole direction as compared to Run 1. Run 3, illustrated by dotted lines, shows the winter helium bulge can't be generated after the vertical wind in the He module is turned off, which implies that the vertical wind is the main source for the winter helium bulge formation instead of horizontal advection. However, the vertical wind (upward wind in summer and downward wind in winter) is associated with large-scale horizontal advection from summer to winter because the atmosphere must conserve mass continuity in the system.

As the vertical wind is critical to the formation of the winter helium bulge, Figure 5.5 illustrates the global distribution of the vertical wind, He number density from TIEGCM Run 1, and NRL-MSISE00 simulation in day 10 at two altitudes: 150 km on the left and 400 km on the right. The vertical wind plots in Figure 5.5a,d show an overall downward wind in the winter hemisphere and upward winds in the summer hemisphere at both 150 km and 400 km. The magnitude of the vertical wind velocity increases by about 100% from 150 km toward 400 km. Note that the results in Figure 5.5 are at a fixed UT = 4, so the longitudinal variation also represents the local time variation as: $L.S.T. = 4+Longitude/15$. The longitudinal (local time)

www.manaraa.com

variation of the vertical wind in Figure 5.5a shows a semi-diurnal tidal pattern at 150 km, and

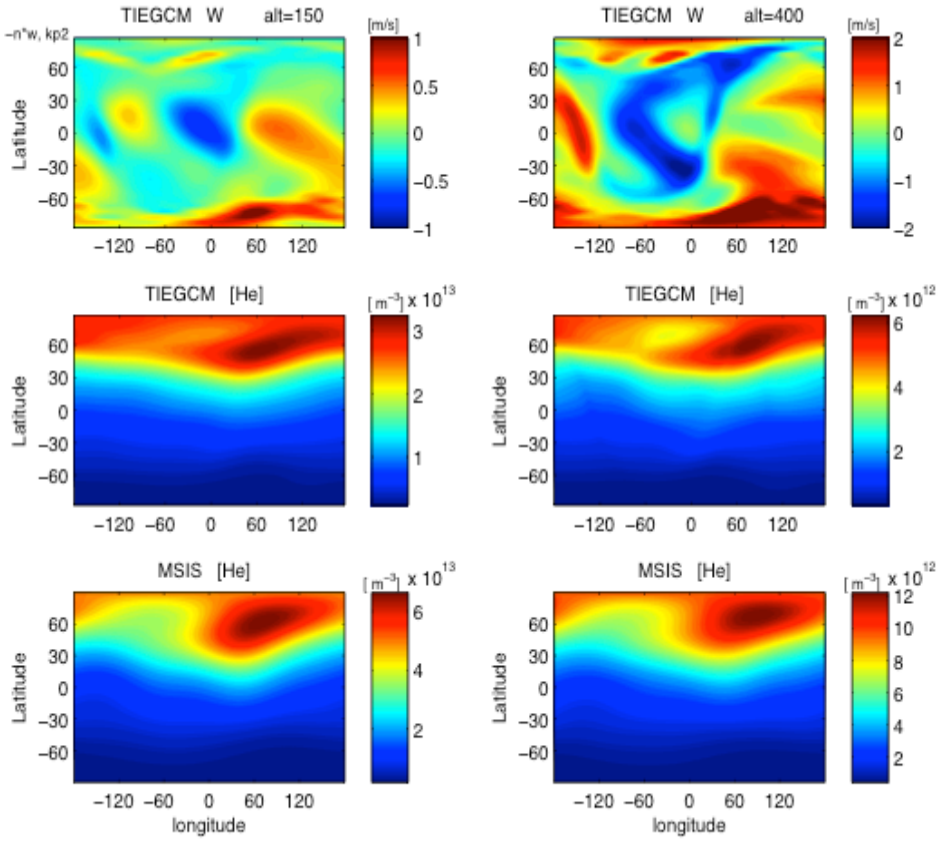

Figure 5.5. From top to bottom are the latitudinal and longitudinal variations of the vertical wind by TIEGCM, helium number density by TIEGCM and helium number density by NRL-MSISE00 in day 10. The left are the results at 150 km and the right are the results at 400 km. Fixed $F_{10.7}$=70 sfu, K_p=2, UT=4. The upper boundary flux for the helium module is $-w(z)*n_{he}(z)$.

a day-night variation at 400 km. The vertical wind is upward on the dayside and flows downward on the nightside at 400 km as shown in Figure 5.5d. The global pattern of the He number density from the TIEGCM is comparable with that from the NRL-MSISE00 at both 150 km (Figure 5.5b vs. 5.5c) and 400 km (Figure 5.5e vs. 5.5f), however, the absolute He number density of TIEGCM is of the same magnitude but smaller than the result of the NRL-MSISE00. This is

www.manaraa.com

probably due to the TIEGCM run beginning with a zero-He number density initial state. The longitudinal (local time) variation of the He number density shows the peaks are near 60°-75° in longitude, which is around 08:00 to 09:00 in local time as displayed in Figure 5.5b,e. This is consistent with *Cageao et al.* [1984], who suggested the largest He number density was found around 09:00 local time for a single orbital pass from the AE-E mass spectrometer measurement at 270 km in 1977.

5.5 Discussion and Conclusions

The horizontal transport between hemispheres is the most widely accepted mechanisms for the winter helium bulge formation in the 1970s, however, the simulations from the TIEGCM, using a minor gas He module that I implemented, illustrated in Figure 5.4 that although horizontal transport changes the latitude pattern of the helium bulge, it is not the mechanism for the winter helium bulge formation. Another possible mechanism for the winter helium bulge formation is the variation of the turbopause altitude, which has been discussed extensively by Reber and Nicolet [1965], Kockarts and Nicolet [1962] etc. However, Kockarts [1972] pointed out that a factor of 50 variation in the eddy diffusion coefficient is required to explain the He data from Ogo 6 satellite measurements. In this chapter the variation of the eddy diffusion coefficient is turned off in the TIEGCM modeling.

The zonal mean of the vertical wind as a function of altitude in Figure 5.6a illustrates an overall upward wind in the summer hemisphere and downward wind in the winter hemisphere. And the vertical wind velocity increases with altitude in both hemispheres. The solid lines

www.manaraa.com

(dashed lines) in Figure 5.6b shows the altitude distribution of He in summer and winter with (without) vertical winds.

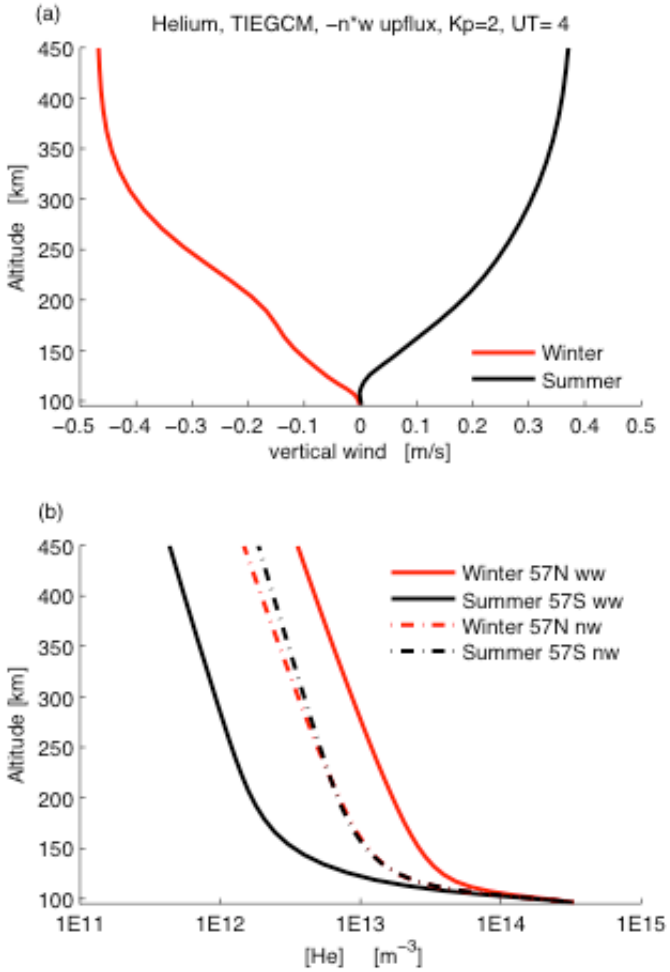

Figure 5.6. (a) The altitude profile of the zonal mean vertical wind at 57 degree N (winter hemisphere) and 57 degree S (summer hemisphere) in day 10; (b) The altitude profile of the zonal mean He number density from TIEGCM Run 1 in solid line and TIEGCM Run 3 in dash line at 57 degree N (winter hemisphere) and 57 degree S (summer hemisphere) in day 10. Fixed $F_{10.7}$=70 sfu, K_p=2, *UT*=4, *Lon*=100 degree. The upper boundary flux for the helium module is $-w(z)*n_{he}(z)$.

The He number density from Run 3 of the TIEGCM w/He as a minor species with the vertical wind effect turned off in the He module is given by the dashed lines. With no vertical winds, the

www.manaraa.com

He number density is slightly higher in the summer pole (57° S) than in the winter pole (57° N), and the altitude distributions of He are in diffusive equilibrium, which is also supported by the Equation 1.22 in Chapter 1. The solid lines show the results of Run 1 with the vertical wind effect included in the He module. The He number density decreases in the summer hemisphere due to the upward wind and increases in the winter hemisphere due to the downward wind, as compared to the result of no vertical winds in Run 3 given by the dashed lines. The altitude distribution of He number density (Run 1) is a departure from diffusive equilibrium (Run 3) due to vertical winds. *Kasprzak* [1969] summarized seven rocket flight measurements and illustrated that the vertical profiles of He densities consistently departed from diffusive equilibrium, and attributed the departure to an upward flux of He with a magnitude of 10^8 to 10^{10} $cm^{-2}s^{-1}$. The other major constituents, such as N_2 and Ar are in diffusive equilibrium with only some exceptions [*Hedin and Nier*, 1965; *Kasprzak et al.,* 1968; *Krankowsky et al.,* 1968]. According to Equation 1.23 in Chapter 1, the amount of departure from a diffusive equilibrium profile for the minor species due to the vertical motion is approximately related to the term $-\frac{U(z)n_i(z)m_i}{H_P}[1-\frac{m_i}{m}]$ in Equation 1.23 after combining the minor species momentum with the continuity equation. Here n_i is the number density of minor gas, $U_{(z)}$ is the vertical wind, H_P is the pressure scale height of the major gas, m_i is the molecular mass of the minor gas and m is the mean molecular mass of the major gas. Thus the upward wind in summer hemisphere causes a decrease in He, which is a lighter minor species, and the downward wind in winter hemisphere causes an increase in He concentration. Note that both the temperature difference and vertical

www.manaraa.com

wind difference can cause the He number density difference between the summer and winter hemispheres, however, the effect due to the temperature difference is quite small compared to the vertical wind effect as shown in Figure 5.6b.

According to the continuity equation shown in Equation 1.22 in Chapter 1, which is

$$\rho\frac{\partial}{\partial t}(\frac{\rho_i}{\rho}) = -\frac{\partial}{\partial z}\{-D(z)\rho_i(z)[\frac{1}{H_{\rho i}} - \frac{1}{H^*_{\rho i}} + \frac{m_i}{kT}\sum_{t\neq i}\upsilon_{it}C_t^z] - k(z)\rho_i(z)[\frac{1}{H_\rho} - \frac{1}{H^*_{\rho i}}]\} - U(z)\rho_i(z)[\frac{1}{H_\rho} - \frac{1}{H^*_{\rho i}}]$$

the molecular diffusion, eddy diffusion and the vertical wind effect are the three main processes that affect the change in concentration of species *i* if ignoring the production and loss processes of species *i*. In the Equation 1.22, $H^*_{\rho i}$ is the actual density scale height of species *i* calculated by the altitude distribution of the mass density of species *i*. $H^*_{\rho i} = -\frac{1}{\rho_i}\frac{\partial \rho_i}{\partial z}$, $H_{\rho i}$ is the density scale height of species *i* assuming species *i* is in diffusive equilibrium. $\frac{1}{H_{\rho i}} = \frac{1}{H_{mi}} + \frac{1}{H_T} + \frac{kT}{m_i g}$, and H_ρ is the total mass density height assuming total density is in diffusive equilibrium. $\frac{1}{H_\rho} = \frac{1}{H_m} + \frac{1}{H_T} + \frac{kT}{mg}$. Figure 5.7 displays the $H^*_{\rho i}$ in the black dotted line, $H_{\rho i}$ in the blue dotted line, and the H_ρ in the red dot line. The Figure 5.7a is for the species He, Figure 5.7b is for O and Figure 5.7c is for N_2. From Equation 1.22, molecular diffusion tends to force the density distribution of the species *i* with altitude to follow the density scale height of species *i*, while eddy diffusion and the vertical wind term try to drag the species *i* to follow the total mass density scale height. Note that the eddy diffusion is dominant at the lowest altitudes, molecular diffusion is dominant at the higher altitudes, and the vertical wind effect is competing with

www.manaraa.com

molecular diffusion for the altitudes in between. Thus, the actual mass density scale height of species *i*, $H_{\rho i}^{*}$, which determines the density profile of the species *i*, is close to the total mass density scale height H_{ρ} at lower altitudes, and transitions from the total mass density scale height H_{ρ} to its own density scale height $H_{\rho i}$ at the altitudes where vertical wind effect are comparable with the molecular diffusion effect. The altitude distribution of species *i* density follows its own mass density scale height at the altitude where the molecular diffusion effect is dominant compared to the vertical wind and the eddy diffusion terms. The result of the behavior of these three scale heights ($H_{\rho i}^{*}, H_{\rho i}, H_{\rho}$) for He, O and N_2 as shown in Figure 5.7a, b and 5.7c is consistent with the analysis above. The data used in Figure 5.7 are the same as the data of the summer (57° S) used in Figure 5.6. Figure 5.7d compared $H_{\rho i}^{*}$ for N_2 in green and O in purple and He in yellow. The density distribution of N_2, O and He with altitude follow the same scale height at the lower altitudes where the eddy diffusion is dominant. The scale heights of these three species show separations at the altitudes where vertical wind and molecular diffusion are both effective and the difference between the scale heights of these three species become larger at the altitudes where the molecular diffusion is dominant as compared to the lower altitudes.

Note that He was implemented into the TIEGCM model as a minor species in the prior analysis. To illustrate the development of the winter helium bulge in the He major species model, Figure 5.8b plots the latitudinal variation of the relative He number density to the latitude mean using the same initial state and same solar/geomagnetic condition as Figure 5.3 (repeated in

www.manaraa.com

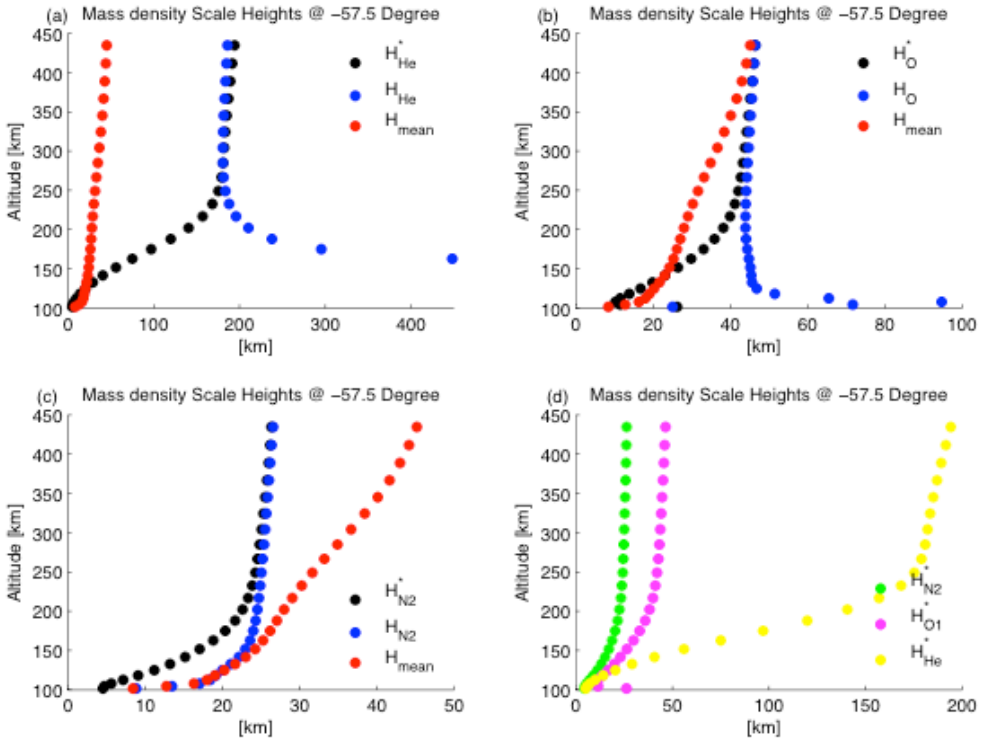

Figure 5.7. Altitude variation of the mass density scale heights: the black dotted line is the actual density scale height for species *i* ; the blue dotted line is the density scale height of species *i* assuming in diffusive equilibrium and the red dotted line is the total mass density height assuming in diffusive equilibrium. (a) is for He, (b) is for O and (c) is for N_2. (d) are the actual density scale heights for N_2 in green, O in purple and He in blue. The density is the zonal mean density from TIEGCM Run 1 at 57 degree S (summer hemisphere) in day 10. Fixed $F_{10.7}$=70 sfu, K_p=2, *UT*=4, *Lon*=100 degree. The upper boundary flux for the helium module is $-w(z)*n_{he}(z)$.

Figure 5.8a). The result in Figure 5.8b suggests that the latitude pattern of the relative He number density on day 10 of the model Run 1 from the He major species model is consistent with the result from the He minor species model shown in Figure 5.8a. There is only a slight difference in the absolute value of the relative He number density in these two models. Thus, the He minor species model can be used to study the short-term variations, such as the winter helium bulge

www.manaraa.com

mechanism and storm time perturbations. The He major species model can be used to study the long-term variation of He behavior, such as seasonal and solar cycle variations.

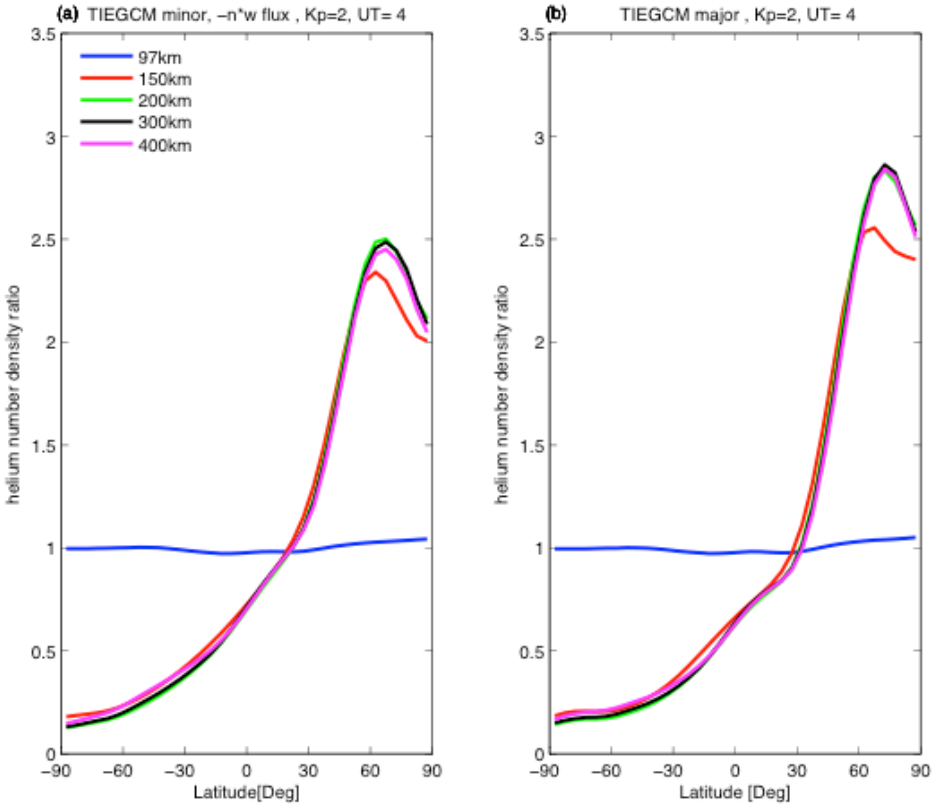

Figure 5. 8. (a) Exactly the same as Figure 5.3b; (b) Similar to (a), but from TIEGCM with helium as major species model with same solar condition.

In conclusion, we examined both the horizontal transport effect and the vertical wind effect in the formation of the winter helium bulge. After turning off the horizontal transport term, the winter bulge still appears with the peak location, but more equator-ward than in the run for which both effects are included, This implies the horizontal transport effect is not the mechanism for the winter helium bulge. The vertical wind forces the altitude distribution of the He number density to depart from diffusive equilibrium. The downward vertical wind increases the He

www.manaraa.com

number density in the winter hemisphere and the upward wind reduces the He concentration in the summer hemisphere at the altitude where the He is a lighter and minor species. Based on the boundary condition imposed, the local change due the molecular diffusion and vertical wind is the main mechanism for the winter helium bulge formation.

www.manaraa.com

Chapter 6 Conclusions and Outlooks

6.1 Conclusions

This dissertation has detailed how the thermosphere preconditioned composition state affect the thermosphere mass density perturbations using a combination of high-resolution observations and numerical models. Chapters 2 and 3 demonstrate the usage of mass density observations from the CHAMP and GRACE satellites to investigate the thermosphere mass density response with latitude and altitude to geomagnetic activity during their coplanar orbital periods in February 2007 and December 2008. The chief scientific finding in Chapters 2 and 3 are listed as follows:

- The preconditioned state of a cold and contracted thermosphere during this solar minimum resulted in a predominance of He in the winter hemisphere near GRACE altitudes. The thermosphere mass density response in the winter hemisphere was influenced by the relative amount of He and O present.
- In the February 2007 period, the C/G mass density ratio decreased with increasing geomagnetic activity in the winter hemisphere, in a manner similar to that in the summer hemisphere which predominantly is caused by temperature changes. However, the winter hemisphere C/G mass density response to geomagnetic activity is caused predominantly by changes in the vertical gradient of the logarithmic mean molecular weight.

www.manaraa.com

- The C/G mass density ratio in December 2008 depicted He-dominant effects in the winter hemisphere with the response increasing with geomagnetic activity and being anticorrelated with the summer hemisphere response
- The observed behavior is indicative of how the thermosphere composition preconditioned state influences the mass density response. The dynamic action of the O to He transition region in both latitude and altitude leads to complex behaviors in the mass density response at GRACE altitudes throughout the extended solar minimum from 2007 to 2010.
- The mass density response from quiet to active conditions is found to be less enhanced in the winter hemisphere at the higher GRACE altitudes (25%) than at CHAMP altitudes (60%) and is attributed to dynamic behavior in the He/O transition.
- The investigation revealed the maximum storm-time density perturbation to occur near the O/He transition region with a much weaker maximum near the O/N_2 transition region. The altitude of maximum density perturbation occurs where the perturbation of the density scale height is equal to zero.
- The altitude structure of density scale height perturbation is significantly influenced by the changes in the molecular weight scale height and can account for 50% of the change in mass density scale height in a region correspondingly close to the O/He transition during 2008 solar minimum period.

Helium is one of the key species in understanding the thermosphere composition preconditioned state during this recent extreme solar minimum. However, the behavior of He is

www.manaraa.com

far less understood than other species, such as O and N_2 , because the lack of both direct measurement and physical modeling. In this study, helium number densities near 500 km altitude were extracted from the CHAMP and GRACE measurements and clearly show the presence of a winter hemisphere helium bulge. This recent extreme solar minimum indicates winter-time He concentrations exceed NRL-MSISE00 estimates by 30%-70% during quiet geomagnetic activity after adjusting $F_{10.7}$ input into MSIS. During active geomagnetic conditions, helium concentrations at GRACE altitudes decrease while O concentrations increase in response to thermal expansion and vertical winds induced by a geomagnetic storm.

In addition to investigating the effects of pre-conditioning, this work has implemented a He module into the National Center for Atmospheric Research (NCAR) Thermosphere Ionosphere Electrodynamics General Circulation Model (TIEGCM).

Chapter 4 assessed the TIEGCM's output when implementing He as a major species. Comparisons between the modeling of TIEGCM without a He module and the modeling of TIEGCM with a He module illustrated the importance of including He as a major gas when modeling extreme solar minimum conditions. The altitude variation of mass density response in the TIEGCM is reproduced in the TIEGCM model with He included. The comparative results between TIEGCM with He vs. without, detailed in Chapter 4, are listed as following:

- The incorporation of He into the TIEGCM as a major species is a self-consistent process that shows consistency with observations.
- There are two possible mechanisms that change the thermosphere parameters after adding He: 1) an increase in mass density scale height after adding He; 2) increases in

www.manaraa.com

the specific heat, thermal conductivity and molecular viscosity, and consequent changes the thermodynamic properties. The first mechanism changes the mass density scale height and is responsible for most of the differences in thermosphere parameters

- The He concentrations are very minor at low altitudes and high pressure levels, hence the effect of adding He on the mass density are negligible. The density change are within ± 1%, primarily due to temperature changes.
- The He concentration increases significantly when going towards the higher altitudes and lower pressure levels, causing the changes in mean molecular weight and mass density to be significant, especially in the winter hemisphere where the winter helium bulge appear. The change in mass density could be up to 35% when including He.
- The altitude profile of the mass density change illustrates negative changes at low altitudes because the change is larger in temperature than in mean molecular weight. The mass density change is positive in high altitudes because the change is larger in mean molecular weight than in temperature due to a large amount of He existing at high altitudes.
- At a fixed pressure level, the mass density change is proportional to the change in mean molecular weight and inverse proportional to the change in temperature. At the pressure level 26 (~400 km), the latitude pattern of the mass density from TIEGCM w/o He suggests higher density in the summer than in the winter. This latitude structure reverses to higher density in the winter than in the summer after implementing He, which cause a significant change in the mass density of about 35% in winter hemisphere.

www.manaraa.com

Chapter 5 discussed implementation of a He module in the TIEGCM assuming He acts as a minor gas. This enabled the model to revisit the mechanism for the winter helium bulge formation. Both the effect of horizontal transport between hemispheres and the effect of the vertical wind in the formation of the helium bulge were examined in the model. The TIEGCM minor He modeling result suggested that:

- Vertical winds and molecular diffusion are the main source for the winter helium bulge formation.
- The altitude distribution of the He number density departs from the diffusive equilibrium due to the vertical winds.
- Downward winds in the winter hemisphere enhance the He concentration while upward winds in the summer hemisphere depresses the He concentration at an altitude where He is a minor species.
- The horizontal transport between hemispheres, pushes the peak location of the helium bulge poleward, however is a minor effect to the formation of the winter helium bulge.

6.2 Recommendation for Future Study

The impact of He on the latitude variation of mass density response at GRACE altitudes during solar minimum is illustrated in this study. The mass density response at CHAMP altitudes can be used as a comparison as it is dominated by O. This study was based on a case study of a geomagnetic storm during an extreme solar minimum. As the CHAMP and GRACE satellite data cover numerous geomagnetic storms in different seasons from 2007 to 2010, a more

www.manaraa.com

comprehensive and statistical study of the impact of a He-dominant preconditioned state on the mass density response at GRACE altitude is recommended for future study.

Helium is photochemically inert and low in mass, which makes it an excellent tracer for thermospheric dynamics [*Reber,* 1976]. Given the limited attention paid to thermosphere He behavior since 1980's, and the results in this dissertation, further investigation of the He morphology is still needed to advance the study of thermosphere gasses. The He module in the NCAR-TIEGCM model can be used to study the solar cycle, latitude-seasonal, diurnal variation of He. In addition, the He impact on the ionosphere is also worth investigating in the future. The output of He in the TIEGCM model can be used as the input for plasmasphere models and the influence of He on the plasmasphere can be also studied. Furthermore, a comparison of He and H morphology will extend our understandings in thermosphere dynamics.

www.manaraa.com

References

Allen, J., and H. Kroehl (1975), Spatial and temporal distributions of magnetic effects of auroral electrojets as derived from AE indices, Journal of Geophysical Research, 80(25), 3667-3677.

Baker, D. N., T. I. Pulkkinen, X. Li, S. G. Kanekal, J. B. Blake, R. S. Selesnick, M. G. Henderson, G. D. Reeves, H. E. Spence, and G. Rostoker (1998), Coronal mass ejections, magnetic clouds, and relativistic magnetospheric electron events: ISTP, Journal of Geophysical Research: Space Physics, 103(A8), 17279-17291.

Banks, P. M., and G. Kockarts (1973), Aeronomy, part B, Academic, San Diego, Calif, 259.

Bates, H. F. (1974), Atmospheric expansion from Joule heating, Planetary and Space Science, 22(6), 925-937.

Bates, H. F. (1974), Thermospheric changes shortly after the onset of daytime Joule heating, Planetary and Space Science, 22(12), 1625-1636.

Bruinsma, S. L., and J. M. Forbes (2010), Anomalous behavior of the thermosphere during solar minimum observed by CHAMP and GRACE, Journal of Geophysical Research: Space Physics (1978-2012), 115(A11).

Burns, A., W. Wang, T. Killeen, S. Solomon, and M. Wiltberger (2006), Vertical variations in the N2 mass mixing ratio during a thermospheric storm that have been simulated using a coupled magnetosphere-ionosphere-thermosphere model, Journal of Geophysical Research: Space Physics (1978-2012), 111(A11).

Burns, A. G., T. Killeen, G. Carignan, and R. Roble (1995), Large enhancements in the O/N2 ratio in the evening sector of the winter hemisphere during geomagnetic storms, Journal of Geophysical Research: Space Physics (1978-2012), 100(A8), 14661-14671.

Cageao, R., and R. Kerr (1984), Global distribution of helium in the upper atmosphere during solar minimum, Planetary and Space Science, 32(12), 1523-1529.

Carignan, G., and W. Pinkus (1968), Ogo-F04 experiment description TechRep., Note 08041-3-T, Univ. of Mich., Ann Arbor.

Carignan, G. R., B. P. Block, J. C. Maurer, A. E. Hedin, C. A. Reber, and N. W. Spencer (1981), The neutral mass spectrometer on Dynamics Explorer B, Space Science Instrumentation, 5, 429-441.

www.manaraa.com

Chapman, S. (1937), The heating of the ionosphere by the electric currents associated with geomagnetic variations, Terrestrial Magnetism and Atmospheric Electricity, 42(4), 355-358.

Chen, Y., L. Liu, and W. Wan (2011), Does the F10. 7 index correctly describe solar EUV flux during the deep solar minimum of 2007-2009, Journal of Geophysical Research: Space Physics (1978-2012), 116(A4).

Crowley, G., A. Reynolds, J. Thayer, J. Lei, L. Paxton, A. Christensen, Y. Zhang, R. Meier, and D. Strickland (2008), Periodic modulations in thermospheric composition by solar wind high speed streams, Geophysical Research Letters, 35(21), L21106.

DeVries, L. L. D., E.W. Friday, L.C. Jones (1967), Analysis of density data deduced from low-altitude, high resolution satellite tracking data, Space Res., 7, 1173-1182.

Dickinson, R. E., E. C. Ridley, and R. G. Roble (1984), Thermospheric general circulation with coupled dynamics and composition, Journal of the Atmospheric Sciences, 41(2), 205-219.

Duncan, R. (1969), F-region seasonal and magnetic-storm behaviour, Journal of Atmospheric and Terrestrial Physics, 31(1), 59-70.

Emmert, J., J. Lean, and J. Picone (2010), Record-low thermospheric density during the 2008 solar minimum, Geophysical Research Letters, 37(12).

Emmert, J. T., R. R. Meier, J. M. Picone, J. L. Lean, and A. B. Christensen (2006), Thermospheric density 2002–2004: TIMED/GUVI dayside limb observations and satellite drag, Journal of Geophysical Research: Space Physics, 111(A10), A10S16.

Fuller-Rowell, T., D. Rees, B. Tinsley, H. Rishbeth, A. Rodger, and S. Quegan (1990), Modelling the response of the thermosphere and ionosphere to geomagnetic storms: Effects of a mid-latitude heat source, Advances in Space Research, 10(6), 215-223.

Haaser, R., G. Earle, R. Heelis, W. Coley, and J. Klenzing (2010), Low-latitude measurements of neutral thermospheric helium dominance near 400 km during extreme solar minimum, Journal of Geophysical Research: Space Physics (1978-2012), 115(A11).

Hagan, M., and J. M. Forbes (2002), Migrating and nonmigrating diurnal tides in the middle and upper atmosphere excited by tropospheric latent heat release, Journal of Geophysical Research, 107(D24), 4754.

www.manaraa.com

Hartmann, G., K. Mauersberger, and D. Müller (1968), Evaluation of the turbopause level from measurements of the helium and argon content of the lower thermosphere above Fort Churchill, Space Res, 8, 940.

Hays, P., R. Jones, and M. Rees (1973), Auroral heating and the composition of the neutral atmosphere, Planetary and Space Science, 21(4), 559-573.

Hedin, A. (1983), A Revised thermospheric model based on mass spectrometer and incoherent scatter data: MSIS-83, Journal of Geophysical Research: Space Physics (1978-2012), 88(A12), 10170-10188.

Hedin, A., and G. Carignan (1985), Morphology of thermospheric composition variations in the quiet polar thermosphere from Dynamics Explorer measurements, Journal of Geophysical Research, 90(A6), 5269-5277.

Hedin, A., and A. O. Nier (1965), Diffusive separation in the upper atmosphere, Journal of Geophysical Research, 70(5), 1273-1274.

Hedin, A., C. Reber, N. Spencer, H. Brinton, and D. Kayser (1979), Global model of longitude/UT variations in thermospheric composition and temperature based on mass spectrometer data, Journal of Geophysical Research: Space Physics (1978-2012), 84(A1), 1-9.

Heelis, R., J. K. Lowell, and R. W. Spiro (1982), A model of the high-latitude ionospheric convection pattern, Journal of Geophysical Research: Space Physics (1978-2012), 87(A8), 6339-6345.

Hodges Jr, R., and F. Johnson (1968), Lateral transport in planetary exospheres, Journal of Geophysical Research, 73(23), 7307-7317.

Hodges, R. R. (1973), Differential equation of exospheric lateral transport and its application to terrestrial hydrogen, Journal of Geophysical Research, 78(31), 7340-7346.

Jacchia, L. G., and J. W. Slowey (1968), Diurnal and seasonal latitudinal variations in the upper atmosphere, Planetary and Space Science, 16(4), 509-524.

Jacobs, R. L. (1967), Atmospheric density derived from the drag of eleven low-altitude satellites, Journal of Geophysical Research, 72(5), 1571-1581.

www.manaraa.com

Johnson, E., and R. Heelis (2005), Characteristics of ion velocity structure at high latitudes during steady southward interplanetary magnetic field conditions, Journal of Geophysical Research: Space Physics (1978-2012), 110(A12).

Johnson, F. (1964), Composition changes in the upper atmosphere.

Johnson, F. (1964), Composition Changes in the Upper Atmosphere, Electron Density Distribution in Ionosphere and Exosphere, E. Thrane, North Holland, Amsterdam.

Johnson, F., and B. Gottlieb (1969), Composition changes in the lower thermosphere, Space Res, 9, 442.

Johnson, F. S., and B. Gottlieb (1970), Eddy mixing and circulation at ionospheric levels, Planetary and Space Science, 18(12), 1707-1718.

Kahler, S. W. (1992), Solar flares and coronal mass ejections, Annual Review of Astronomy and Astrophysics, 30, 113-141.

Kasprzak, W. (1969), Evidence for a helium flux in the lower thermosphere, Journal of Geophysical Research, 74(3), 894-896.

Kasprzak, W., D. Krankowsky, and A. O. Nier (1968), A study of day-night variations in the neutral composition of the lower thermosphere, Journal of Geophysical Research, 73(21), 6765-6782.

Keating, G., and E. Prior (1968), The winter helium bulge, Space Res., 8(982).

Kim, J. S., J. V. Urbina, T. J. Kane, and D. B. Spencer (2012), Improvement of TIE-GCM thermospheric density predictions via incorporation of helium data from NRLMSISE-00, Journal of Atmospheric and Solar-Terrestrial Physics, 77, 19-25.

Kockarts, G. (1972), Distribution of hydrogen and helium in the upper atmosphere, Journal of Atmospheric and Terrestrial Physics, 34(10), 1729-1743.

Kockarts, G., and M. Nicolet (1962), Aeronomical problem of neutral helium and hydrogen, Ann. Geophys, 18(3), 269-290.

Krankowsky, D., W. Kasprzak, and A. O. Nier (1968), Mass spectrometric studies of the composition of the lower thermosphere during summer 1967, Journal of Geophysical Research, 73(23), 7291-7306.

www.manaraa.com

Lei, J., J. P. Thayer, A. G. Burns, G. Lu, and Y. Deng (2010), Wind and temperature effects on thermosphere mass density response to the November 2004 geomagnetic storm, Journal of Geophysical Research, 115(A5), A05303.

Lei, J., J. P. Thayer, J. M. Forbes, E. K. Sutton, and R. S. Nerem (2008), Rotating solar coronal holes and periodic modulation of the upper atmosphere, Geophysical Research Letters, 35(10), L10109.

Lei, J., J. P. Thayer, W. Wang, and R. L. McPherron (2011), Impact of CIR storms on thermosphere density variability during the solar minimum of 2008, Sol Phys, 274(1-2), 427-437.

Lühr, H., M. Rother, W. Köhler, P. Ritter, and L. Grunwaldt (2004), Thermospheric up-welling in the cusp region: Evidence from CHAMP observations, Geophysical Research Letters, 31(6).

Marcos, F. A., S. T. Lai, C. Y. Huang, C. S. Lin, J. M. Retterer, S. H. Delay, and E. K. Sutton (2010), Towards next level satellite drag modeling, AIAA 2010-7840, paper presented at the AIAA Atmospheric and Space Environments Conference, Toronto, Ontario, Canada, 2–5 August.

Matsuo, T., and J. M. Forbes (2010), Principal modes of thermospheric density variability: Empirical orthogonal function analysis of CHAMP 2001-2008 data, Journal of Geophysical Research, 115(A7), A07309.

Mauersberger, K., D. Kayser, W. Potter, and A. Nier (1976), Seasonal variation of neutral thermospheric constituents in the northern hemisphere, Journal of Geophysical Research, 81(1), 7-11.

Mauersberger, K., W. Potter, and D. Kayser (1976), A direct measurement of the winter helium bulge, Geophysical Research Letters, 3(5), 269-271.

Mayr, H., I. Harris, and N. Spencer (1978), Some properties of upper atmosphere dynamics, Reviews of Geophysics, 16(4), 539-565.

McAfee, J. (1967), Lateral flow in the exosphere, Planetary and Space Science, 15(4), 599-609.

Müller, S., H. Lühr, and S. Rentz (2009), Solar and magnetospheric forcing of the low latitude thermospheric mass density as observed by CHAMP, Annales Geophysicae, 27, 2087-2099.

www.manaraa.com

Mursula, K., and B. Zieger (1996), The 13.5-day periodicity in the Sun, solar wind, and geomagnetic activity: The last three solar cycles, Journal of Geophysical Research: Space Physics, 101(A12), 27077-27090.

Offermann, D. (1974), Composition variations in the lower thermosphere, Journal of Geophysical Research, 79(28), 4281-4293.

Picone, J., A. Hedin, D. P. Drob, and A. Aikin (2002), NRLMSISE-00 empirical model of the atmosphere: Statistical comparisons and scientific issues, Journal of Geophysical Research, 107(A12), 1468.

Pilinski, M. D., B. M. Argrow, and S. E. Palo (2010), Semiempirical Model for Satellite Energy-Accommodation Coefficients, Journal of Spacecraft and Rockets, 47(6), 951-956.

Pilinski, M. D., B. M. Argrow, and S. E. Palo (2011), Drag coefficients of satellites with concave geometries: Comparing models and observations, Journal of Spacecraft and Rockets, 48(2), 312-325.

Prölss, G. (1976), On explaining the negative phase of ionospheric storms, Planetary and Space Science, 24(6), 607-609.

Prölss, G. (1980), Magnetic storm associated perturbations of the upper atmosphere: Recent results obtained by satellite-borne gas analyzers, Reviews of Geophysics, 18(1), 183-202.

Prölss, G. (1981), Latitudinal structure and extension of the polar atmospheric disturbance, Journal of Geophysical Research: Space Physics (1978-2012), 86(A4), 2385-2396.

Prölss, G. W. (1992), Satellite mass spectrometer measurements of composition changes, Advances in Space Research, 12(10), 241-251.

Prölss, G. W. (2011), Density perturbations in the upper atmosphere caused by the dissipation of solar wind energy, Surveys in Geophysics, 32(2), 101-195.

Prölss, G., and M. Roemer (1985), Some properties of the polar energy source and of the associated atmospheric perturbations, Advances in Space Research, 5(7), 193-202.

Prölss, G., and U. Von Zahn (1977), Seasonal variations in the latitudinal structure of atmospheric disturbances, Journal of Geophysical Research, 82(35), 5629-5632.

www.manaraa.com

Qian, L., S. C. Solomon, and M. G. Mlynczak (2010), Model simulation of thermospheric response to recurrent geomagnetic forcing, Journal of Geophysical Research: Space Physics (1978-2012), 115(A10).

Reber, C., J. Cooley, and D. Harpold (1968), Upper atmosphere hydrogen and helium measurements from the Explorer 32 satellite, Space Res, 8, 993.

Reber, C., D. Harpold, R. Horowitz, and A. Hedin (1971), Horizontal distribution of helium in the earth's upper atmosphere, Journal of Geophysical Research, 76(7), 1845-1848.

Reber, C. A. (1976), Dynamical effects in the distribution of helium in the thermosphere, Journal of Atmospheric and Terrestrial Physics, 38(8), 829-840.

Reber, C. A., and P. B. Hays (1973), Thermospheric wind effects on the distribution of helium and argon in the Earth's upper atmosphere, Journal of Geophysical Research, 78(16), 2977-2991.

Reber, C. A., and M. Nicolet (1965), Investigation of the major constituents of the April-May 1963 heterosphere by the Explorer XVII satellite, Planetary and Space Science, 13(7), 617-646.

Reigber, C., H. Lühr, and P. Schwintzer (2000), CHAMP mission status and perspectives, Eos Trans. AGU, 81(48), F307.

Rentz, S., and H. Lühr (2008), Climatology of the cusp-related thermospheric mass density anomaly, as derived from CHAMP observations, Annales Geophys, 26, 2807-2823.

Richardson, I. G., E. W. Cliver, and H. V. Cane (2001), Sources of geomagnetic storms for solar minimum and maximum conditions during 1972–2000, Geophysical Research Letters, 28(13), 2569-2572.

Richmond, A., E. Ridley, and R. Roble (1992), A thermosphere/ionosphere general circulation model with coupled electrodynamics, Geophysical Research Letters, 19(6), 601-604.

Rishbeth, H., T. Fuller-Rowell, and D. Rees (1987), Diffusive equilibrium and vertical motion in the thermosphere during a severe magnetic storm: a computational study, Planetary and Space Science, 35(9), 1157-1165.

Rishbeth, H., R. Gordon, D. Rees, and T. Fuller-Rowell (1985), Modelling of thermospheric composition changes caused by a severe magnetic storm, Planetary and Space Science, 33(11), 1283-1301.

www.manaraa.com

Rishbeth, H., and I. Müller-Wodarg (1999), Vertical circulation and thermospheric composition: a modelling study, paper presented at Annales Geophysicae, Springer.

Roble, R., E. C. Ridley, A. Richmond, and R. Dickinson (1988), A coupled thermosphere/ionosphere general circulation model, Geophysical Research Letters, 15(12), 1325-1328.

Rothwell, P., and C. E. McIlwain (1960), Magnetic storms and the Van Allen radiation belts—Observations from satellite 1958ε(Explorer IV), Journal of Geophysical Research, 65(3), 799-806.

Sentman, L. H. (1961), Free molecule flow theory and its application to the determination of aerodynamic forcesRep, DTIC Document.

Shimazaki, T., Effects of vertical mass motions on the composition structure in the thermosphere, Space Res., 12, 1039–1045, 1972.

Showstack, R. (2002), GRACE Mission Promises improved maps of Earth gravity, Eos, Transactions American Geophysical Union, 83(14), 158-158.

Solomon, S. C., L. Qian, L. V. Didkovsky, R. A. Viereck, and T. N. Woods (2011), Causes of low thermospheric density during the 2007- 2009 solar minimum, Journal of Geophysical Research: Space Physics (1978-2012), 116(A2).

Spencer, N., H. Niemann, and G. Carignan (1973), The neutral-atmosphere temperature instrument, Radio Science, 8(4), 287-296.

Spencer, N. W., and G. R. Carignan (1988), In situ measurements of thermospheric composition, temperature and winds by mass spectrometry, Advances in Space Research, 8(5-6), 107-117.

Strickland, D. J., R. R. Meier, R. L. Walterscheid, J. D. Craven, A. B. Christensen, L. J. Paxton, D. Morrison, and G. Crowley (2004), Quiet-time seasonal behavior of the thermosphere seen in the far ultraviolet dayglow, Journal of Geophysical Research: Space Physics, 109(A1), A01302.

Stubbe, P. (1972), Vertical neutral gas motions and deviations from the barometric law in the lower thermosphere, Planetary and Space Science, 20(2), 209-215.

Sutton, E. K. (2009), Normalized force coefficients for satellites with elongated shapes, Journal of Spacecraft and Rockets, 46(1), 112-116.

www.manaraa.com

Sutton, E. K., J. M. Forbes, and R. S. Nerem (2005), Global thermospheric neutral density and wind response to the severe 2003 geomagnetic storms from CHAMP accelerometer data, Journal of Geophysical Research: Space Physics (1978-2012), 110(A9).

Sutton, E. K., R. S. Nerem, and J. M. Forbes (2007), Density and winds in the thermosphere deduced from accelerometer data, Journal of Spacecraft and Rockets, 44(6), 1210-1219.

Tapley, B. D., S. Bettadpur, M. Watkins, and C. Reigber (2004), The gravity recovery and climate experiment: Mission overview and early results, Geophysical Research Letters, 31(9).

Thayer, J., X. Liu, J. Lei, M. Pilinski, and A. Burns (2012), The impact of helium on thermosphere mass density response to geomagnetic activity during the recent solar minimum, Journal of Geophysical Research, 117(A7), A07315.

Thayer, J. P., J. Lei, J. M. Forbes, E. K. Sutton, and R. S. Nerem (2008), Thermospheric density oscillations due to periodic solar wind high-speed streams, Journal of Geophysical Research, 113(A6), A06307.

Trinks, H., and U. Von Zahn (1975), The ESRO 4 gas analyzer, Review of Scientific Instruments, 46(2), 213-217.

Tsurutani, B. T., E. Echer, and W. D. Gonzalez (2011), The solar and interplanetary causes of the recent minimum in geomagnetic activity (MGA23): a combination of midlatitude small coronal holes, low IMF B Z variances, low solar wind speeds and low solar magnetic fields, Ann. Geophys, 29, 839-849.

Turner, N. E., E. J. Mitchell, D. J. Knipp, and B. A. Emery (2006), Energetics of magnetic storms driven by corotating interaction regions: A study of geoeffectiveness, Recurrent magnetic storms: corotating solar wind streams, 113-124.

Von Zahn, U. (1975), Early aeronomy results from the satellite Esro 4, in Atmospheres of Earth and the Planets, edited, pp. 133-157, Springer.

Webb, D. F. (1991), The solar cycle variation of the rates of CMEs and related activity, Advances in Space Research, 11(1), 37-40.

Weimer, D. R. (1996), A flexible, IMF dependent model of high-latitude electric potentials having "space weather" applications, Geophysical Research Letters, 23(18), 2549-2552.

www.manaraa.com

Xu, J., W. Wang, and H. Gao (2013), The longitudinal variation of the daily mean thermospheric mass density, Journal of Geophysical Research: Space Physics, 118(1), 515-523.

Yashiro, S., N. Gopalswamy, G. Michalek, O. C. St. Cyr, S. P. Plunkett, N. B. Rich, and R. A. Howard (2004), A catalog of white light coronal mass ejections observed by the SOHO spacecraft, Journal of Geophysical Research: Space Physics, 109(A7), A07105.

Zhang, Y., and L. J. Paxton (2011), Long-term variation in the thermosphere: TIMED/GUVI observations, Journal of Geophysical Research, 116(null), A00H02.

www.manaraa.com

Appendix A Drag Coefficient Calculations

The GRACE densities are re-computed according to the method presented by *Sutton* [2009], but with an adjusted MSIS atmosphere based on a reduction in $F_{10.7}$ from 67 to 53 sfu. A six-panel model for the GRACE satellite is first defined and includes information on panel area and orientation. Next, the drag coefficient in each panel is computed according to Sentman's equations [*Sentman*, 1961] and the results are combined to form the drag coefficient of the entire object. The following equations govern free-molecular flow force coefficients on a flat plate with one side exposed to the flow under the assumption of diffuse reflection (Sentman's model)

$$C_{D,\text{plate}} = \frac{2}{s\sqrt{\pi}}\exp\left(-s^2\sin\theta_{\text{in}}\right) + \frac{\sin\theta_{\text{in}}}{s^2}\left(1+2s^2\right)\text{erf}\left(s\sin\theta_{\text{in}}\right) + \frac{\sqrt{\pi}}{s}\sin^2\theta_{\text{in}}\sqrt{\frac{T_{k,\text{out}}}{T_a}} \quad \text{(A1)}$$

where θ_{in} is the angle between the surface-normal and incident velocity vector, T_a is the temperature of the atmosphere, $T_{k,out}$ is the kinetic temperature of the outgoing molecules, while the speed ratio s is defined as

$$s = \left|\left|\vec{V}_r\right|\right|\beta \quad \text{(A2)}$$

and can be thought of as the ratio of bulk speed to the most probable thermal speed. The analytic solutions are carried out for N_s species considered in the computation and combined as a weighted mean. Equation A3 demonstrates this concept for the k^{th} panel in the geometry.

$$C_{D,k} = \frac{\sum_{j=1}^{N_s} C_{D,j} n_i m_i}{\sum_{j=1}^{N_s} n_i m_i} \quad \text{(A3)}$$

www.manaraa.com

The results from each of the N_p panels can then be combined to compute a force coefficient for the entire shape. First the total cross sectional area is computed for the panel model.

$$A_{\text{ref}} = \sum_{k=1}^{N_p} A_{\text{proj},k} \tag{A4}$$

In equation A4, A_{ref} is the cross sectional area projected in the direction of the free-stream velocity

$$A_{proj,k} = \begin{cases} A_{\text{plan},k}\left|\hat{n}_k \cdot \hat{V}_i\right| & \text{if} \quad \hat{n}_k \cdot \hat{V} < 0 \quad \text{panel facing incoming flow} \\ 0 & \text{if} \quad \hat{n}_k \cdot \hat{V} \geq 0 \quad \text{panel facing away from flow} \end{cases}$$

where $A_{plan,k}$ is the geometric area (planform area) of the k^{th} panel. Next, the panel results are weighted by panel area to produce the total force coefficient as shown in equation A5.

$$C_D = \frac{\sum_{k=1}^{N_p} C_{D,k} A_{\text{plan},k}}{A_{\text{ref}}} \tag{A5}$$

The drag coefficient and cross sectional areas obtained this way are shown in Figure A.1 as a function of He/O ratio for two values of atmospheric temperature (T_a) and angle of attack (β). An increase in the amount of He relative to O increases the drag coefficient. This is because, at any given temperature, the bulk velocity for a lighter molecule remains the same while the most probable thermal speed increases as the inverse square-root of mass, lowering the speed ratio more in the presence of the lighter species and increasing most of the terms in equation A1.

This is particularly true for long panels aligned with the bulk velocity ($\theta_{in} \approx 90^\circ$ in equation A1) which is often the case for the GRACE satellites. Similarly, an increase in temperature also decreases the speed ratio, causing an increased C_D. Physically, a lower speed ratio associated with increased thermal speeds (higher temperatures or lower molecular masses) causes more

www.manaraa.com

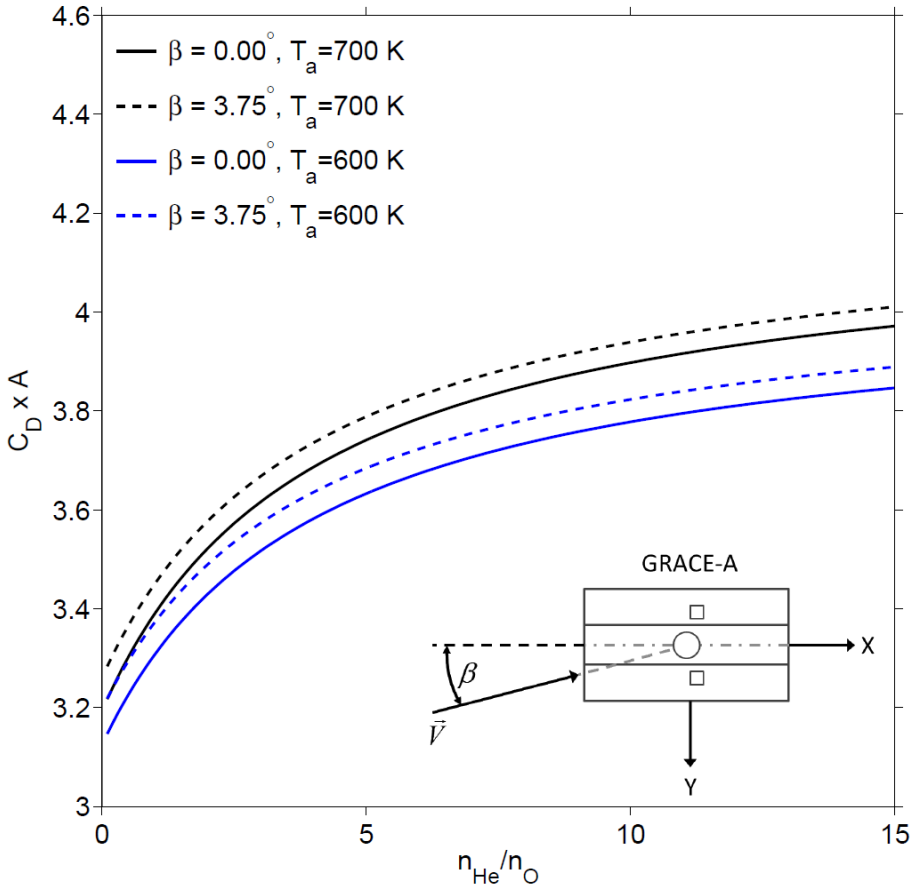

Figure A.1. GRACE panel model C_DxA as a function of He/O ratio at two values of atmospheric temperature and angle of attack.

molecules to reach the long sides of the satellite, increasing the momentum exchange between the spacecraft and the atmosphere. For example, a doubling of the He/O ratio from 5 to 10 increases C_DxA from 3.74 to 3.90 when the atmospheric temperature is fixed at 700 K. The same increase in He/O at a T_a of 600 K increases the drag from 3.63 to 3.78. Note that such an increase in He/O accompanied by a drop in temperature of 100 K results in almost no change in C_DxA. This is approximately indicative of the conditions experienced in the December 2008 period presented in this paper when using the orginal and adjusted $F_{10.7}$ values as input to the MSIS

www.manaraa.com

model. The lowering of the $F_{10.7}$ index in MSIS results in a decrease in the exospheric temperature while increasing the He-to-O ratio at GRACE altitudes. The two effects on the C_D offset each other. Figure A.2 shows the MSIS ouputs for the abovementioned $F_{10.7}$ and A_p inputs indicating that the He/O ratio changes from 3 to 5.7 in the winter hemisphere while the temperature drops by 50K. Thus, little error in C_D is expected due to changes in the ballistic coefficient. However, if the atmosphere were to increase He/O without an accompanying decrease in temperature, i.e. departures in diffusive equilibrium due to transport, then the drag coefficient would increase and become more of a factor in determining the mass density from accelerometer data.

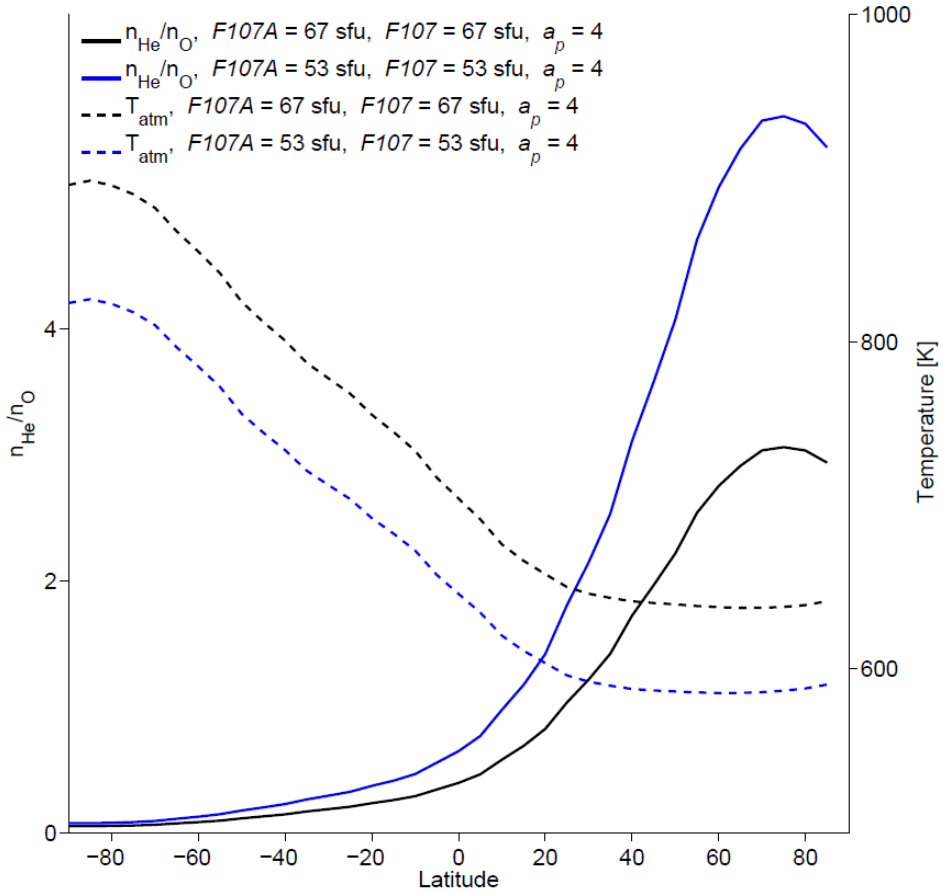

Figure A.2. MSIS outputs for December 9th 2008, sampled along the GRACE orbit.

www.manaraa.com

Appendix B Helium concentration estimation at the GRACE altitude

The He concentration can be estimated using the mass density measurements from CHAMP and GRACE satellites and temperature output from NRL-MSISE00 model. The CHAMP mass density at 350 km consists primarily of atomic O. The O scale height between the CHAMP and GRACE satellites can be calculated using the exospheric temperature estimated by NRL-MSISE00. The O density at the altitude of GRACE is derivable assuming atomic O is in diffusive equilibrium between CHAMP and GRACE satellites. This same method is applied to the other species such as N_2, O_2 and H. Note that O and He constitute up to 98% of the total mass density in this altitude range. The He concentration can be estimated by subtracting the O mass density, and species mass densities other than He, from total mass density measurements at GRACE altitude. The following steps outline the detail of this method and the error estimation.

The first step is to estimate the exospheric temperature from the NRL-MSISE00 model. To do so, the mass density from the mid and low latitude regions (60° S to 40° N) estimated by the CHAMP satellite are compared with estimates from MSIS for a range of input values of the $F_{10.7}$ index. Figure B.1a is an example of adjusting the MSIS model density output to provide a close fit to the CHAMP satellite density measurement on 09 December 2008. The red line in Figure B.1a represents the daily mean of the mass density from CHAMP measurements as a function of latitude. The black lines are the adjusted MSIS density at the same altitude as CHAMP with the adjustments of $F_{10.7}$ from -15 on the left to -9 on the right. The criterion for best fit is the smallest variance between the density of CHAMP and the adjusted MSIS density. The best adjustment of

www.manaraa.com

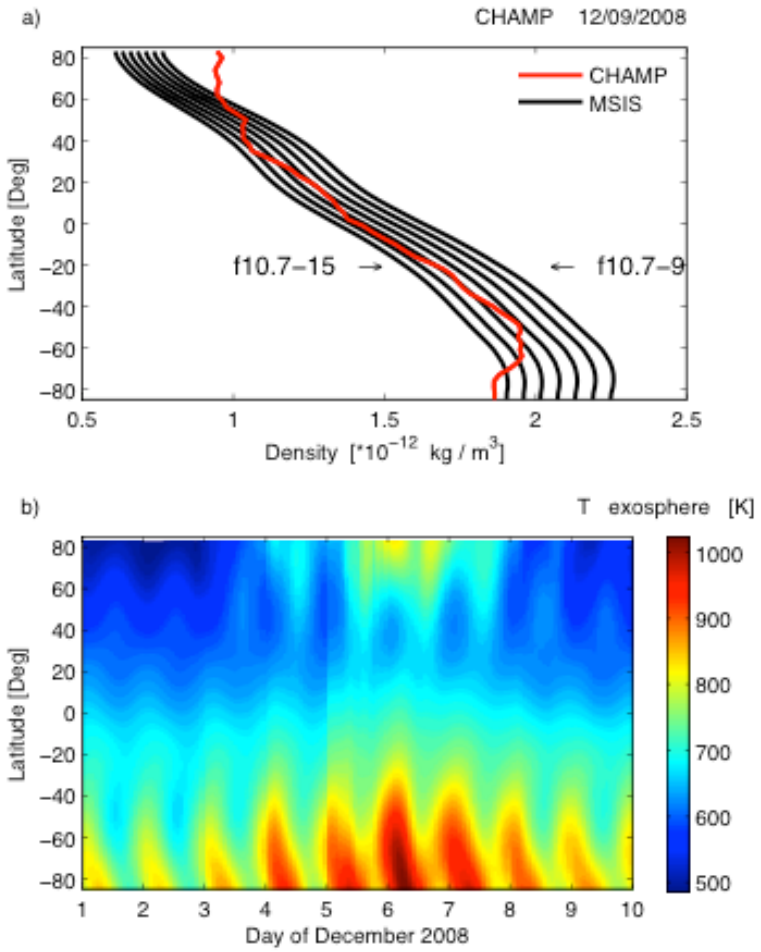

Figure B.1. An example of the $F_{10.7}$ adjustment to best fit the NRL-MSISE00 total mass density output (black) with the total mass density by CHAMP measurement (red) in 09 December 2008; The adjustments of $F_{10.7}$ were from -15 to -9 with a step of 1, (b) Latitudinal variation of the MSIS adjusted exosphere temperature for 01-09 December 2008.

$F_{10.7}$ for 09 December 2008 period is -14 as shown in Figure B.1a. Based on other observations during this extreme solar minimum [e.g., *Solomon et al.,* 2011], $F_{10.7}$ seems to overestimate the EUV flux and a downward adjustment of the proxy is required. Similar adjustments are applied to the period 01-10 December 2008. Figure B.1b shows latitudinal and UT variation of the

www.manaraa.com

adjusted MSIS exosphere temperature during 01-10 December 2008. The summer-winter variation, storm time variation and diurnal variation of the exosphere temperature are clearly illustrated in the Figure B.1b.

The next step is to determine the O mass density at CHAMP altitude from the total mass density measurement by CHAMP. The approach is to use the adjusted MSIS exosphere temperature T_{exo}, oxygen density O_{CH}^{MSIS}, and total mass density ρ_{CH}^{MSIS} in this step. Then the ratio of O_{CH}^{MSIS} to ρ_{CH}^{MSIS} is used to scale the CHAMP mass density estimate and extract the O density,

$$O_{CH} = \rho_{CH}^{Sat} \frac{O_{CH}^{MSIS}}{\rho_{CH}^{MSIS}} \tag{B1}$$

where O_{CH} is the estimated O density at CHAMP altitude and ρ_{CH}^{Sat} is the total mass density from CHAMP measurement. It is assumed that the O mass mixing ratio $O_{CH}^{MSIS} / \rho_{CH}^{MSIS}$ is properly represented by the MSIS model after the adjustment. This is a reasonable assumption as atomic O is expected to be the major species at this altitude.

The next step is to calculate the atomic O mass density at the altitude of GRACE by assuming diffusive equilibrium,

$$O_{GR} = O_{CH} \exp(-\frac{h_{GR} - h_{CH}}{H_O}) \qquad H_O = \frac{KT_{exo}}{m_O g} \tag{B2}$$

where O_{GR} is the calculated atomic O density at the altitude of GRACE, h_{GR} and h_{CH} are the altitudes for the CHAMP and GRACE satellites, respectively, H_O is the atomic O scale height and m_O is the mean molecular mass of atomic O. Although the primary constituent of the total

www.manaraa.com

mass density at CHAMP altitudes is O, N_2 and other more minor species also increase during the storm period, particularly in the summer polar region. To account for this contribution, the same method as above is applied to those species as well. The result of this process is an estimate of N_2, O_2 and H mass density at the altitude of the GRACE satellite. The amount of the adjusted MSIS number densities of N_2, O_2 and H sum up to less than 0.8% of the total number density in the winter hemisphere and less than 2% of the total number density in summer hemisphere in this study.

The final step is to calculate the He mass density by subtracting the O, N_2, O_2 and H density from the total mass density of the GRACE measurement.

$$He_{GR} = \rho_{GR}^{sat} - O_{GR} - N2_{GR} - O2_{GR} - H_{GR} \tag{B3}$$

The uncertainty in the estimate of He density at GRACE altitudes is primarily determined by how well atomic O at GRACE altitudes is determined. In turn, the atomic O concentration is sensitive to the calculated O density at CHAMP altitudes and the estimated exospheric temperature.

$$\frac{\sigma_{O_{GR}}^2}{O_{GR}^2} = \frac{\sigma_{O_{CH}}^2}{O_{CH}^2} + \frac{\sigma_{T_{exo}}^2}{T_{exo}^2}\left(\frac{h_{GR} - h_{CH}}{H_O}\right)^2 \tag{B4}$$

Considering the primary composition of the thermosphere at CHAMP altitudes is atomic O and the O mixing ratio $O_{CH}^{MSIS} / \rho_{CH}^{MSIS}$ is about 98%, so that most of the uncertainty in O_{CH} is close to the uncertainty in the total mass density estimate from the CHAMP measurement. This statistical error is about 10% according to estimates by *Sutton et al.* [2007]. From the relation between the $F_{10.7}$ adjustment and the corresponding MSIS exospheric temperature change shown

www.manaraa.com

in Figure B2a, the exospheric temperature increase (decrease) depends on latitude with about 4 K change in the winter hemisphere and 5 K change in the summer hemisphere for each increasing (decreasing) increment in the $F_{10.7}$ index. Assuming a 10% uncertainty in the density estimate, the error in exospheric temperature is on the order of $\sigma_{T_{exo}} = 12\text{K}$ in the winter hemisphere and 17K in the summer hemisphere.

According to equation (B4) and above assumptions, the latitudinal variation of the uncertainty in calculated O density at GRACE altitude is illustrated in Figure B.2b. The uncertainty of calculated O density is larger in the winter hemisphere than that in the summer, and larger in quiet times than storm times, because the uncertainty is inversely proportional to T_{exo}^2. It is about 15% in the winter polar region compared to 12% in the summer region for 01-10 December 2008.

There could also be a bias in the mass density measurements between the GRACE and CHAMP estimates that would affect the He density retrieval, however this bias is expected to be small. The annual mean bias for CHAMP and GRACE in 2008 is about 1.03 (Eric Sutton, private communication), which means $\frac{\rho_{CH}}{\rho_{CH}^{MSIS}} = 1.03\frac{\rho_{GR}}{\rho_{GR}^{MSIS}}$. If this bias is included in estimating the uncertainty of the calculated He at GRACE altitude, the Equation (B4) could be written as

$$\frac{\sigma_{O_{GR}}^2}{O_{GR}^2} = (\frac{1}{bias_{index}})^2(\frac{\sigma_{O_{GR}}^2}{O_{GR}^2} + \frac{\sigma_{T_{exo}}^2}{T_{exo}^2}(\frac{h_{GR} - h_{CH}}{H_O})^2) \qquad \text{(B5)}$$

where $bias_{index} = 1.03$. If the effect of the bias between CHAMP and GRACE measurements is included, the estimated He density would decrease by 3%.

www.manaraa.com

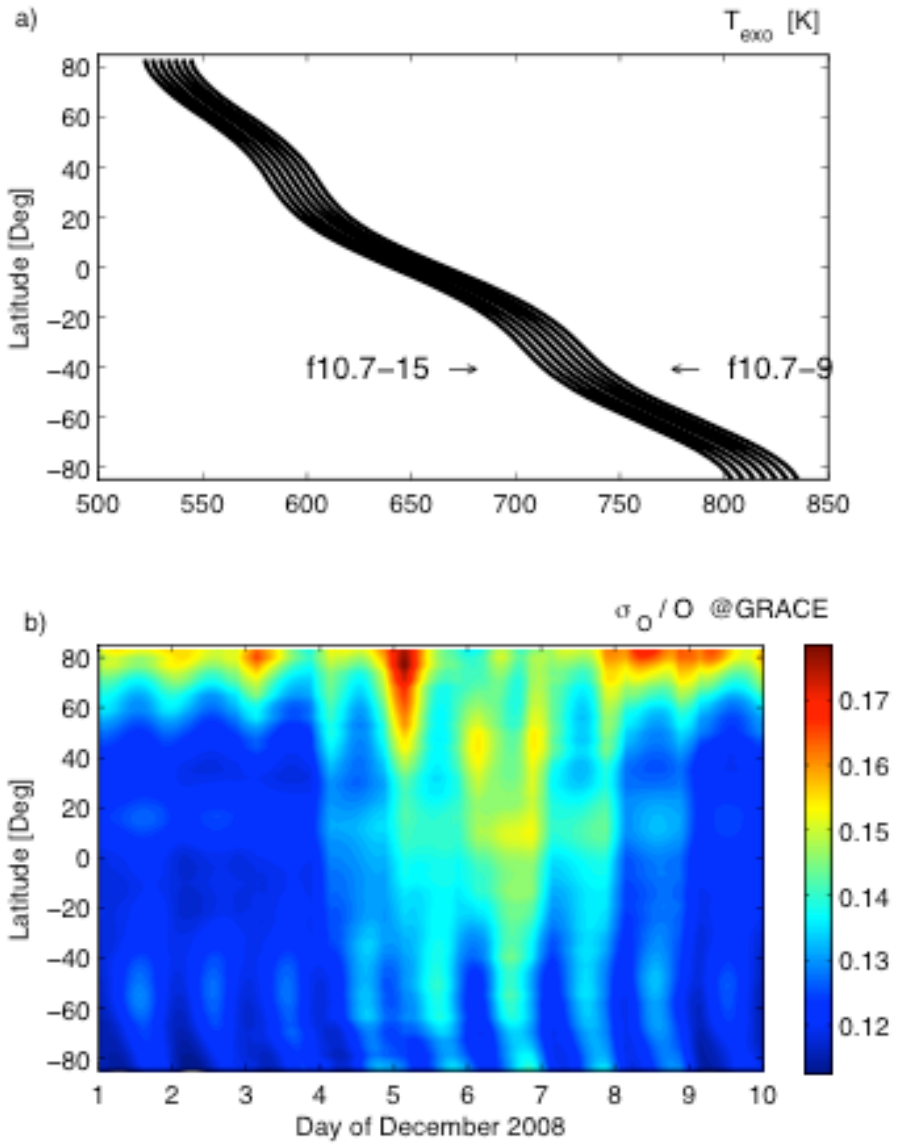

Figure B.2. (a) Latitudinal variation of the NRL-MSISE00 estimated exosphere temperature in 09 December, 2008 with the $F_{10.7}$ adjustments from -15 to -9; the step of the $F_{10.7}$ adjustment is 1, (b) Latitudinal variation of the relative uncertainty in calculated oxygen density at GRACE altitude from 01-09 December 2008. The result includes the error propagation of the uncertainty of oxygen density at CHAMP altitude and the uncertainty of the MSIS adjusted exosphere temperature at fixed 09 SLT.

www.manaraa.com